METAL MOLD FABRICATION BY PROTON BEAM WRITING AND ITS APPLICATIONS

WANG YINGHUI

(*B.Sc, ShanDong University*)

A THESIS SUBMITTED

FOR THE DEGREE OF DOCTOR OF PHILOSOPHY

DEPARTMENT OF PHYSICS

NATIONAL UNIVERSITY OF SINGAPORE

2013

DECLARATION

I hereby declare that the thesis is my original work and it has been written by me in its entirety. I have duly acknowledged all the sources of information which have been used in the thesis.

This thesis has not been submitted for any degree in any university previously.

Signature:

WANG Yinghui

01/08/2013

Research Supervisor: ----------

A/Prof. van Kan, Jeroen Anton

Internal Examiner: ----------

A/Prof.

Internal Examiner: ----------

A/Prof.

External Examiner: ----------

Dr.

NATIONAL UNIVERSITY OF SINGAPORE

To my dearest parents

Acknowledgements

The last four years are a fantastic journey in my life. I never thought I could meet so many wonderful people who care me and help me during this journey.

Firstly, I would like to give my sincere thanks to my supervisor Associate Prof Jeroen van Kan. His enthusiasm and circumspection on science have impressed me and give me great passion on the research topic. His suggestions and encouragement helped me solve every difficulty in the work. From him I also learned to believe in and be confident in what I do.

Secondly, I want to thank Dr. Shao Peige who brought me to this lab. Dr. Shao is a very nice person. I still remember the first time he talked to me and the first time he taught me to do experiment. Now he has passed away because of cancer. Wish he is happy in heaven.

I also would like to thank Dr P. Malar, Dr P.S. Raman, Nan Nan, Liu Fan, Yao Yong for their help and valuable discussions.

I am also grateful to Prof Frank Watt, Associate Prof Thomas Osipowicz, Prof Mark Breese and Asst Prof Andrew Bettiol for their discussions and suggestions.

I also want to thank Mr Armin Baysic De Vera, who helped me a lot in hardware problems. I also want to thank Mr Choo for teaching me a lot on CIBA accelerator and helping me optimize the system. Thanks to Dr Ow Yueh Sheng Isaac and Dr Chen Xiao for assisting me a lot in my beginning of PhD study and helping me to enter into the spirit of CIBA.

Thanks to all other people in CIBA, Dr Ren Minqin, Dr Chammika Udalagama, Dr Chan Taw Kuei, Dr Yan Yuanjun, Dr Vanga Sudheer Kumar,

Dr Mallikarjuna Rao Motapothula and Dr Sara Azimi. I am also grateful to the students in CIBA, Zhiya, Haidong, Jianfeng, Chengyuan, Zhaohong and Prashant. CIBA is a family and I am proud to be part of it.

I also would like to thank the students from Shandong University who help me a lot in my PhD, Xinjun, Fusheng, Lanfei, Yuzhan, Yingying, Guanggeng, Wang Qian, Wang Xiao, Yanan, Huihui, Wentao, Junpeng and Hongwei.

I would like to thank Song Jiao, my beloved girl that I met during my PhD. She is the one who makes me happy everyday; she is the one who encourages me when I am depressed; she is the one who gives me strength to overcome difficulties; she is also the one I love , protect, and take care of with all my heart.

Lastly, I would like to give my sincere thanks to my parents who have been always supporting me to their best. They are my first teacher. They have taught me so much since my childhood------ be frank and honest with people, be persistent and practical with work. Without them, I would never be where I am.

Table of contents

Acknowledgements……i

Abstract……..vii

List of Publications……ix

List of Abbreviations……....x

List of tables……...…xii

List of Figures……...xiii

1 Micro-nanofabrication technologies 1

1.1 Photoresist 1

1.2 Optical Lithography 5

1.3 Electron Beam Lithography (EBL)..... 10

1.4 Ion Beam Technologies 13

1.4.1 Focused ion beam (FIB) 13

1.4.2 Proton beam writing (PBW) 14

1.4.3 Ion projection lithography (IPL)..... 15

1.5 X-ray Lithography 16
1.6 Summary 18
References 21
2 Proton beam writing 29
2.1 Proton beam writing set up 29
2.2 Proton beam writing of Micro-nanostructures 36
2.3 Resist materials for PBW 40
2.3.1 ma-N series 41
2.3.2 PMMA series 49
2.3.3 AR-P series 52
2.4 Summary 67
References 68
3 Fabrication of Nickel mold for nanoimprinting and injection molding 72
3.1 Ni electroplating 72
3.2 Ni electroplating system: Technotrans AG, RD. 50 plating system 75
3.3 Ni electroplating of protonn beam fabrication resist structures 78
3.3.1 Ni molds fabricated with ma-N series resist 82
3.3.2 Ni pillars and molds fabricated with 950k PMMA 86
3.3.3 Ni molds fabricated with AR-P 3250 93
3.3.4 Ni molds fabricated with mixture resist (AR-P 3250: AR 300-12=1: 3) 94
3.4 Summary 95
References 97
4 Introduction to Nanoimprint Lithography and Applications of Ni molds 99
4.1 Introduction to Nanoimprint Lithography (NIL) 99

4.1.1 Thermoplastic nanoimprint lithography 101
4.1.2 UV-cured nanoimprint 106
4.2 Applications of Ni molds fabricated by PBW and electroplating 107
4.2.1 Imprinting results of Ni mold fabricated by AR-P 3250 108
4.2.2 Imprinting results of Ni mold fabricated by mixture resist (AR-P 3250: AR 300-12=1: 3) 113
4.3 Microfluidic particle separartion device fabrication and test 113
4.3.1 Particle separation design 113
4.3.2 Ni mold fabrication for particle separation device ... 114
4.3.3 NIL of microfluidic device 117
4.3.4 Thermal bonding of the microfluidic device 117
4.4 Summary 119
References 120
5 Application of proton beam fabricated Ni molds in Injection Molding 125
5.1 Introduction to Injection Molding 125
5.2 Ni molds application in Injection Molding 129
5.2.1 Battenfeld Microsystem 50 130
5.2.2 Application of Ni mold fabricated with AR-P 3250 in Injection Molding 134
5.2.3 Application of Ni mold fabricated with ma-N 2410 in Injection Molding 135
5.2.4 Application of Ni mold fabricated with PMMA 950 A11 in Injection Molding 137
5.3 Summary 139
References 140

6 Conclusion..... 144

Appendix……..147

A

B

Abstract

Proton Beam Writing (PBW) is a mask-less, 3D fabrication lithographic technique developed at the Center for Ion Beam Applications (CIBA), Department of Physics, National University of Singapore. It uses a fine focused beam of high energy e.g. MeV protons or H_2^+ to pattern resist and silicon materials with nanometer scale details. Because of the inherent properties of protons, this technique has many advantages over conventional optical lithography and various next generation lithography techniques. The applications of the technique can be applied in optics, micro- and nano-fluidic devices and biochips fabrication.

The aim of my research is to combine PBW with other techniques like electroplating, nanoimprinting and injection molding to realize mass production of plastic products with micro and nanostructures. In order to fabricate the plastic products, the metal mold which can be used in nanoimprinting and injection molding should first be fabricated through electroplating. Prior to fabricate the metal mold with micro and nanostructures, the structures should be achieved in resists. PBW is applied to different kinds of resists to achieve nano structures. One critical aspect for the production of high quality Ni molds is the fact that a resist can be removed after Ni electroplating; this aspect guided the choice of resist in this work.

Chapter 1 introduces what photoresist is and several micro- and nano-fabrication technologies based on lithography technique. The principle, applications and prospective development to the respective approaches are given. Different lithography techniques are compared.

Chapter 2 presents the details of PBW setup in CIBA, national University of Singapore. A list of photoresists that can be used in PBW was given. In addition, several new photoresists were introduced and the results based on the photoresists are discussed. PBW is capable of fabricating 60 nm wide lines in ma-N 2401. Structures with aspect ratio up to 11, with vertical and smooth sidewalls are also achieved using PBW. ARP series resist is a positive resist under UV exposure but behaves as a negative resist when exposed to protons. An explanation for this negative resist behavior of ARP under proton exposure is given.

Chapter 3 gives an introduction of electroplating technique. In this section, the resist structures mentioned in chapter 2 are transferred to metal through Ni electroplating. Structures down to 120 nm are well transferred. In addition, the high aspect ratio (more than 10) structures at a width of 330 nm are transferred in metal.

Chapter 4 is devoted to nanoimprinting lithography (NIL) technology. NIL is introduced with its application and recent development. In our research, 500 nm wide, 4 μm high structures are achieved using nanoimprinting. In this section, a prototype microfluidic cell sorting device is fabricated. Initial tests with the device show that PBW and Ni electroplating can be used in combination with nanoimprinting to produce microfluidic lab on chip devices.

Chapter 5 introduces injection molding technology. A basic knowledge of injection is first given in this chapter. Moreover, Ni molds fabricated by PBW and the new photoresists are also applied in injection molding. Structures down to 300 nm are transferred from mold to plastic. 500 nm wide ridges with aspect ratio of 2 are also well replicated.

Chapter 6 gives an overall conclusion of the research projects.

List of Publications

1. J. A. van Kan, P. G. Shao, Y. H. Wang and P. Malar, *Proton beam writing a platform technology for high quality three dimensional metal mold fabrication for nanofluidic applications*, Microsystem Technologies (2011) 17:1519-1527
2. Y. H. Wang, P. Malar, J. Zhao and J. A. van Kan, *Resist evaluation for Ni mold fabrication and proton beam writing*, Microelectronic Engineering, 102 (2013) 40-43
3. Lu Junpeng, Sun Cheng, Zheng Minrui, Wang Yinghui, Nripan Mathews, Van Kan Jeroen A., Mhaisalkar Subodh G., Sow Chorng Haur, *Ultrasensitive phototransistor based on K-enriched MoO3 single nanowires*, Journal of Physical Chemistry C, p 22015-22020, October 18, 2012
4. Zhibin Hu, Chenggang Zhou, Rajiv Ramanujam Prabhakar, Sharon Xiaodai Lim, Yinghui Wang, Jeroen A. van Kan, Hansong Cheng, Subodh G. Mhaisalkar, and Chorng-Haur Sow, *Rapid reversible electromigration of intercalated K ions within individual MoO_3 nanobundle*, Journal of Applied Physics, 113, 024311 (2013)
5. Y.H. WANG, P. Malar, J. A. van Kan, *Resist evaluation for proton beam writing, Ni mold fabrication and nanoimprinting*, Submitted to microsystem technologies
6. Y.H. WANG, P. Malar, J. A. van Kan, A review of different photoresists applied in proton beam writing, in preparation.

List of Abbreviations

IC	Integrated Circuit
PAC	Photoactive Compound
NA	Numerical Aperture
DOF	Depth of Focus
EBL	Electron Beam Lithography
FIB	Focused Ion Beam
TEM	Transmission Electron Microscopy
PBW	Proton Beam Writing
IPL	Ion Projection Lithography
HVEE	High Voltage Engineering Europa
RBS	Rutherford Back Scattering
RF	Radio Frequency
CCD	Charged-coupled Device
CEM	Channeltron Electron Multiplayer

FWHM	Full width at half maximum
PMMA	Polymethyl Methacrylate
MW	Molecular Weight
MMA	Methylmethacrylate
SEM	Scanning Electron Microscopy
ITRS	International Technology Roadmap for Semiconductor
NIL	Nanoimprint Lithography
CE	Current Efficiency
NEMS	Nanoelectromechanical Systems
RIE	Reactive ion etching
HSQ	Hydrogen Silsesquioxane
PP	Polypropylene
HIPS	High Impact Polystyrene
PC	Polycarbonate
DI	De-ionized
IPA	Isopropanol

List of Tables

Table 1.1 *A very simple comparison of optical lithography, EBL, PBW, FIB, and X-ray lithography in PMMA* 18
Table 2.1 *Current status and dose requirements in PBW* 41
Table 2.2 *Parameters of thinner AR 300-12 [40]* 66
Table 2.3 *Results for new resists in PBW presented in this thesis* 67
Table 3.1 *Compositions for Ni electroplating solution* 77
Table 3.2 *Results achieved in Ni mold fabricated by different resists* 95
Table 6.1 *Results on resist and Ni structures* 144

List of figures

Fig. 1. 1 *Resist exposure and chemical development of positive and negative resist* 2
Fig. 1. 2 *Definition of sensitivity and contrast for positive and negative photoresists [1]* 3
Fig. 1. 3 *(a) Contact printing (b) proximity printing* 6
Fig. 1. 4 *Basic layout of a projection printing system* 7
Fig. 1. 5 *Spectrum of a 100-watt high-pressure mercury plasma arc-discharge lamp* 9
Fig. 1. 6 *Schematic of electron optical system in an e-beam lithography column* 11
Fig. 1. 7 *Schematic of X-ray lithography* 17
Fig. 1. 8 *Comparison between PBW, FIB, EBL and X-ray lithography. The p-beam and e-beam images were simulated using SRIM and CASINO software packages, respectively* 19

Fig. 2. 1 *CIBA Singletron accelerator and beam line applications: (a) X_1, X_2, Y_1, Y_2 Steerers (b) 90° analyzing magnet (c) Objective slits (d) Blanking system (e) switcher magnet; (1) the high resolution RBS facility; (2) the nuclear microscope; (3) the cell and tissue imaging beam line; (4) the next generation proton beam writing facility; (5) the proton beam writer prototype [4]* 30
Fig. 2. 2 *The main facilities of the proton beam writer prototype* 31
Fig. 2. 3 *Schematic diagram of the scanning and control hardware setup at the Centre for Ion Beam Applications, National University of Singapore proton beam writer* 33
Fig. 2. 4 *Example emc source file* 35
Fig. 2. 5 *scan figure produced from example code* 35
Fig. 2. 6 *The point scan order for (a) a raster rectangle, (b) a raster rectangle with a silhouette, (c) a spiral circle and (d) a spiral square is shown for the four emc file entities supported by the current version of the Ionutils software [9]* 36

Fig. 2. 7 *(a)2 MeV Proton-induced secondary electron image from a free-standing Ni grid, (b) beam size measurement spectrum (Assume beam size is FWHM)* 38
Fig. 2. 8 *(a) mounted Si wafer in sample holder. (b) An optical image of the Ni grid (the central part was fabricated by PBW, while the other parts were fabricated by UV lithography).* 38
Fig. 2. 9 *Experimental procedure of PBW for micro- and nanostructures in ma-N (a) Cr and Au sputtering, (b) spin coat resist, (c) PBW, (d) development* 43
Fig. 2. 10 *Dose calibration using 1 MeV proton beam (a---f) the dose of proton is 40 nC/mm^2, 60nC/mm^2, 100nC/mm^2, 120nC/mm^2, 150nC/mm^2, 200nC/mm^2.*.....44
Fig. 2. 11 *(a)250 nm wide lines, (b) 330 nm diameter pillar in a 600 nm thick ma-N 2410 resist layer written with 1 MeV proton beam*.....46
Fig. 2. 12 *Dose calibration using 1 MeV proton beam, the dose of proton is (a,d) 40nC/mm^2 (b,e) 60nC/mm^2 (c,f) 100nC/mm^2* 47
Fig. 2. 13 *(a) 60 nm line in 100 nm thick ma-N 2401 (b) side wall of 100 nm wide line in 100 nm thick ma-N 2401* 48
Fig. 2. 14 *PMMA structural construction*.....49
Fig. 2. 15 *Mechanism of radiation-induced chain scission in PMMA*.....50
Fig. 2. 16 *Experimental procedure of PBW for micro- and nanostructures in PMMA (a) Cr and Au sputtering, (b) spin coat resist, (c) PBW, (d) development* 51
Fig. 2. 17 *SEM image of proton beam written PMMA with a dose of 150 nC/mm^2*.....52
Fig. 2. 18 *Experimental procedures for micro- and nanostructures using PBW and UV exposure (a) Cr and Au sputtering, (b) spincoat resist, (c) PBW, (c) UV exposure, (e)development*.....53
Fig. 2. 19 *optical image of ARP-3250 grids (three samples)*.....55
Fig. 2. 20 *Sample 1 proton dose 50 nC/mm^2 exposed with UV (365 nm using a 100W lamp) for 5 min and developed for 80 s.*.....56
Fig. 2. 21 *Sample 2 proton dose 50 nC/mm^2 exposed with UV (365 nm using a 100W lamp) for 7 min* 57
Fig. 2. 22 *Sample 3 proton dose 50 nC/mm^2 exposed with UV (365 nm using a 100W lamp) for 10 min* 58
Fig. 2. 23 *Contrast curve of AR-P 3250, obtained for 500 nm wide structures in a 4 μm coated resist layer using 1 MeV protons, 7 min UV and 60 s development*……..*59*
Fig. 2. 24 *(a) electron microscope image of AR-P 3250 grids in 4 μm thick layer featuring 500 nm wide lines (b) a high magnification SEM image of the 500 nm wide line in 4 μm thick AR-P 3250* 60

Fig. 2. 25 *AR-P 3250 200 nm wide lines collapse* 61
Fig. 2. 26 *330 nm wide line in 3.5 μm thick AR-P 3250* 62
Fig. 2. 27 *Schematic of measurement method* 63
Fig. 2. 28 *Absorption spectrum of AR-P 3250* 64
Fig. 2. 29 *Absorption spectrum of resist* 64
Fig. 2. 30 *Height of proton beam exposed structure after development* 65
Fig. 2. 31 *(a) electron microscope image of grids in 280 nm thick layer featuring 120 nm wide lines (b) a high magnification SEM image of the 120 nm wide line in 280 nm thick AR-P 3250：AR300-12= 1: 3* 66

Fig. 3. 1 *Electroplating a metal (Me) with Ni in a Ni electrolyte bath* 73
Fig. 3. 2 *System schematic for electroplating cell* 76
Fig. 3. 3 *Schematic of the RD.50 Electroplating Cell.1) Anode Basket 2) Electrolyte 3) Spindle Drive 4) Cathode plus Sample Holder 5) Tunnel Battle 6) Anode Material* 77
Fig. 3. 4 *Ni electroplating (a) resist structures, (b) Ni electroplating (Ni is lower than resist), (c) resist removal* 79
Fig. 3.5 *Ni mold fabrication (a) resist structures, (b) Ti sputtering, (c) Ni electroplating to the top layer of resist, (d) over Ni electroplating, (e) resist removal* 81
Fig. 3. 6 *Schematic sectional back cutting of the sample after plating* 82
Fig. 3. 7 *Sample after Ni electroplating (a) Back side after cutting, the central part is very flat, (b) Front face of Ni, the central part is Si wafer, the other part is copper tape* 83
Fig. 3. 8 *Procedures from coating protection layer to side cutting (a) coating of AR-P protection layer, (b) UV exposure, (c) development, (d) wire spark erosion cutting to obtain the desired size, (e) mold cleaning with acetone* 84
Fig. 3. 9 *(a)Electron microscope image of ma-N 2410 structures written with a 1 MeV proton beam in a 1 μm thick resist layer (b) SEM image of the micro-channels in Ni mold* 85
Fig. 3. 10 *Ni pillars with a diameter of 500 nm at the top* 88
Fig. 3. 11 *The distribution of 1, 2 and 3 meV protons into 9 μm thick PMMA, the crossing point between the curve and arrows means 90% of protons land within this distance [14]* 88
Fig. 3. 12 *Ni electroplated mold featuring 300 x 500 nm^2 wide and 1 μm high pillars plated in a 1 μm thick PMMA resist layer written with a 1 MeV proton beam* 90
Fig. 3. 13 *Optical image of channels fabricated using a 2 MeV proton beam in a 1 μm thick PMMA layer* 91

Fig. 3. 14 *(a) Top view of ridges in the Ni mold (b) tilted view of ridges (15^otilt)* 92
Fig. 3. 15 *Grooves with a depth of 4 µm in the Ni mold obtained via electroplating on AR-P3250 resist, featuring groove width of (a) 1.8 µm, (b) 1.4 µm and (c) 500 nm* 93
Fig. 3. 16 *SEM images of 330 nm wide and 3.5 µm deep grooves in Ni mold* 94
Fig. 3. 17 *(a) 150 nm and (b) 120 nm wide with 280 nm height grooves in Ni mold*..... 95

Fig. 4. 1 *Schematic of nanoimprinting process*..... 102
Fig. 4. 2 *Temperature and pressure evolution during thermal press nanoimprinting*..... 103
Fig. 4. 3 *Schematic of UV-cured Nanoimprint: (a) transparent mold, polymer and substrate, (b) UV exposure to cure the polymer, (c) demolding*..... 107
Fig. 4. 4 *Grooves in Ni mold (a) 5 µm wide (b) 2.5 µm wide. The height of the structure is 4 µm* 108
Fig. 4. 5 *SEM image of the nanoimprinted PMMA structures with width of 5 µm and 2.5 µm: samples (a)-(d)* 110
Fig. 4. 6 *(a) Ni mold with 500 nm wide and 4 µm deep groove, (b) PMMA ridge imprinted at 130 ℃ and 30 bar for 30 s, (c) PMMA ridge imprinted at 120 ℃ and 30 bar for 30 s* 112
Fig. 4. 7 *SEM image of 120 nm wide and 280 nm high line imprinted on spincoated PMMA*..... 113
Fig. 4. 8 *Design showing the dimensions of the microfluidic device*..... 114
Fig. 4. 9 *Schematic procedures of microfluidic device fabrication* 115
Fig. 4. 10 *AR-P 3250 resist structures (a) The whole structure in Si wafer as exposed via UV and PBW (b)Pillars in the large channel fabricated by PBW (c) The collection channels fabricated by UV lithography*..... 116
Fig. 4. 11 *(a) sidewall of 10 µm AR-P resist structure (b) sidewall of 10 µm hole in Ni mold (Height: 10 µm) (c)three holes in a large channel(depth: 11 µm; this mold was used in nanoimprinter)* 116
Fig. 4. 12 *(a) three pillars in a large channel imprinted in PMMA sheet, (b) sidewall of the 11 µm high pillar* 117
Fig. 4. 13 *The configuration of PMMA bonding at 110 ℃ and 1.2 bar for 2 hours* 118
Fig. 4. 14 *Liquid flows in the channel passing through the pillars while filling the chip*..... 118

Fig. 5. 1 *Sketch of injection molding machine* 125
Fig. 5. 2 *The process of injection molding*..... 126

Fig. 5. 3 *50 kN micro injection molding machine from Battenfeld*.....130
Fig. 5. 4 *Schematic drawing of the injection molding machine*.....131
Fig. 5. 5 *Mold set up* 132
Fig. 5. 6 *Ni insert retainer showing the clamping mechanism and the different parts* 133
Fig. 5. 7 *Measured result of injection molded pillars based on profilometer*134
Fig. 5. 8 *Injection molded structures with PC (a) injection speed: 600 mm/s, mold temp.: 80 ℃; (b) injection speed: 600 mm/s, mold temp.: 100 ℃ (inserted figure is Ni mold).* 135
Fig. 5. 9 *Injection molded structures with PMMA (a) injection speed: 700 mm/s, mold temp.: 90 ℃; (b) injection speed: 700 mm/s, mold temp.: 100 ℃. (tilted by 30^{o})*.....136
Fig. 5. 10 *(a) Ni molds fabricated with ridges of 300 nm and 1.5 μm wide, (b) a high magnification of the structures in the central part* 137
Fig. 5. 11 *Injection molded PMMA (b) (c) (d) are high magnification figures labeled in fig. (a)*.....138

Chapter 1 Miro-nanofabrication technologies

Micro-nanofabrication is the fabrication of structures and parts to the dimension of micrometer or nanometer size. In the past 60 years, the development of micro-nanofabrication technologies has greatly pushed forward the development of IC (integrated circuit) technology and bioscience applications. Today, the demand for high resolution structures is still increasing.

In this chapter, I will first give a brief introduction of photoresist which is used in the lithography technologies. Then I will give an overview of the currently used micro-nanofabrication technologies including massive parallel optical lithography, electron beam lithography, ion beam technologies, X-ray lithography.

1.1 Photoresist

Photoresist is a kind of chemical compound which is sensitive to light. There has been a very long history of resist. In 1826, Joseph Nicephore Niepce, in Chalon, France, took the first photograph using bitumen of Judea on a pewter plate, developed using oil of lavender and mineral spirits. In 1935 Louis Minsk of Eastman Kodak developed the first negative photoresist, in 1940 Otto Suess developed the first positive resist. In 1950s, photoresist became popular in the semiconductor industry. Now it is widely used in fabrication of printed circuit boards, sand carving, microelectronics and patterning and etching of substrates.

Photoresists can be divided into positive resists and negative resists according to the reaction to light. For positive resist, the long chain molecules will undergo chain scission under light exposure. After development, the exposed area is removed. In the case of negative resist, the exposed area undergoes cross linking and becomes much more difficult to be dissolved in the developer. Fig. 1.1 shows the difference between positive resist and negative resist.

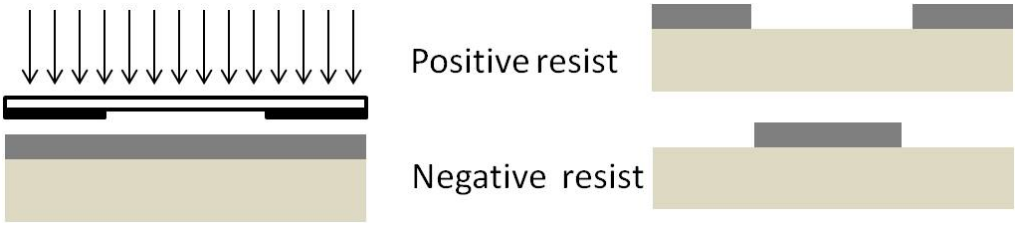

(a) Resist exposure (b) Resist after development

Fig. 1.1 Resist exposure and chemical development of positive and negative resist

Every photoresist has to be synthesized individually to satisfy its special application. Generally, all the conventional photoresists contain 4 elementary components: resin, solvent, photoactive compound (PAC), and additives. Resin is the main part of resist which makes the resist etch resistant. Solvent is used to dissolve resin to liquid, so the resist can be coated on substrate using spin coating. PAC controls the photosensitivity of a resin to a certain wavelength of light. Additives control light absorption and solubility of a photoresist.

In fact, photoresists can also be classified as conventional and chemically amplified resists. The resists mentioned above belong to conventional photoresist. Chemically amplified resists are added into an essential constituent called "Photo Acid Generator" (PAG). PAG can release acid molecules when exposed by UV light. The acid molecules can induce more acid molecules during a key process, the Post Exposure Bake (PEB), causing molecular chain reaction in the resist resulting in change of resist solubility to developers. This wide range of response requires different processing techniques.

Below are several parameters to compare the performance of a photoresist:

1. Sensitivity

   Sensitivity is a measure standard of the exposure speed. It is measured in units of mJ/cm^2 for optical lithography and $\mu C/cm^2$ for electron beam lithography and other kinds of ion beam lithography. The

sensitivity of a resist is describing which radiation dose is needed to cause sufficient chemical change. The higher the sensitivity of a photoresist, the lower the exposure dose required for sufficient exposure, hence the faster the exposure. There is little difference in the definition of sensitivity for positive and negative resists. As shown in Fig. 1.2a, the sensitivity of positive resist is the exposure dose (D_{p}) needed to completely remove the resist after development. While for negative resist, the sensitivity is the exposure dose needed to keep more than 50% of the original thickness of the resist after development [1]. $D_{\mathrm{n}}^{\mathrm{i}}$ is the initial dose that begins to change the property of negative resist and D_n^0 is the dose to completely cross link the resist after development.

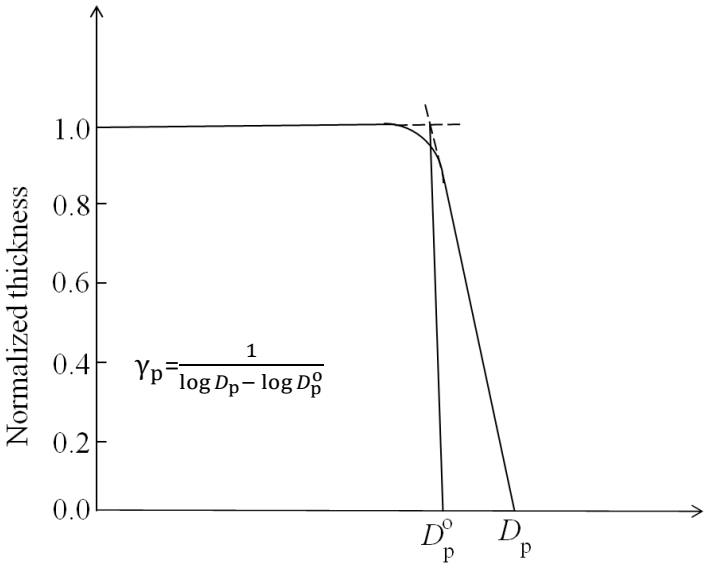

$D_{\mathrm{p}}^{\mathrm{o}}$ threshold dose D_{p} sensitivity γ_{p} contrast

(a) Sensitivity and contrast for positive resist

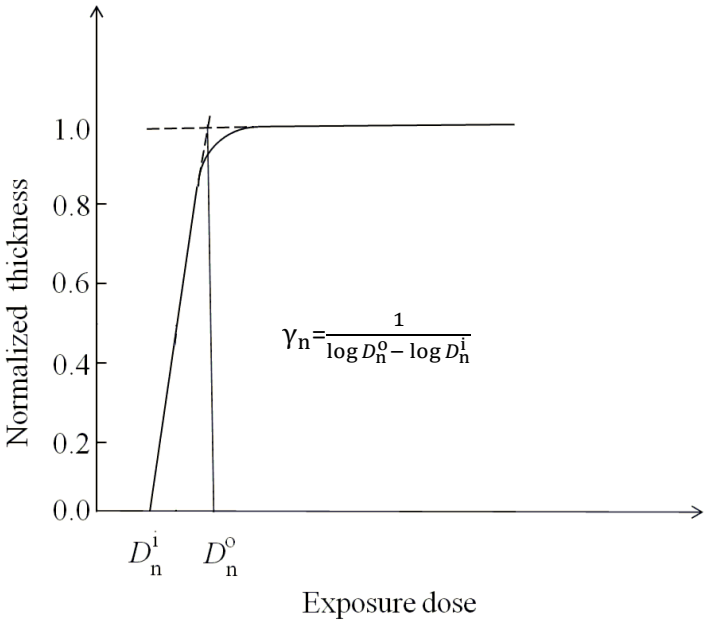

D_n^o threshold dose γ_n contrast

(b) Sensitivity and contrast for negative photoresists

Fig. 1.2 Definition of sensitivity and contrast for positive and negative photoresists [1]

2. Contrast

Contrast is also a very important characteristic of a photoresist. The definition of contrast is also shown in Fig. 1.2. A photoresist with high contrast can be used to fabricate structures with vertical sidewalls and high aspect ratio (ratio between the height and width of a structure). Contrast value of more than 10 was achieved in PMMA with optimization of different developers [2]. When standard development procedures are used, the typical contrast of PMMA with EBL is around 3, similar to proton beam writing [3]. The contrast of HSQ can also be as high as 10 after optimization of developers [4]. However, the typical contrast value is about 3 in EBL and PBW when standard development procedures are employed [5].

3. Resolution

The resolution of a photoresist depends on several factors: (1) the resolution of the exposure system, (2) the molecule weight, molecule

weight distribution, contrast and resist thickness, (3) development condition, pre and post bake temperature, etc.

4. Process latitude

   Variations of processing steps: pre, post baking temperature, development time, concentration of developer and temperature all influence the quality of final resist patterns. Every step has its optimal condition achieving high quality resist patterns. When conditions deviate from their optimized values, the structure size will be affected. Large process latitude results in a small change in final structure size whereas small process latitude will result in larger change of structure size.

5. Shelf life

   Every photoresist has its own shelf life. The photoactive compounds may lose its photoactivity over time.

In the next several sections, several micro-nanofabrication lithography technologies are introduced.

1.2 Optical Lithography

Optical lithography, also called photolithography or UV lithography, is a process used in micro- and nanofabrication to pattern parts in a thin film substrate. It utilizes a flux of photons passing through a patterned mask to transfer the structures on the mask to the thin film substrate. The opaque part on the mask protects the resist from irradiation, the exposed wafer is chemically developed leaving the desired structure in the resist. In general, there are 2 types of optical lithography: shadow printing (mask aligning) and projection printing [6, 7]. Shadow printing has two modes: contact printing and proximity printing. Fig. 1.3a shows a contact printing system. A layer of photoresist is spin coated onto the substrate, then the photoresist is exposed utilizing nearly parallel light passing through the mask. Because of the direct

contact between the mask and the photoresist, the patterns in the photoresist have the same resolution as in the mask. The direct contact, and possible dust particles on the substrate, will damage the mask and thus reduce the lifetime of the mask.

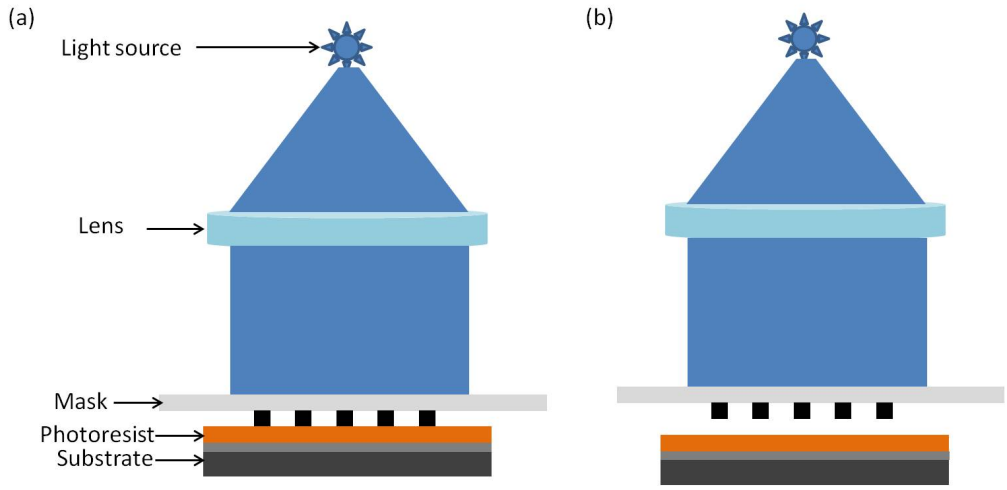

Fig. 1.3 (a) Contact printing *(b) proximity printing*

In order to reduce the damage to the mask, proximity printing was introduced as shown in Fig. 1.3b. The only difference is that during exposure, there is a space between mask and substrate of about 10 μm to 50 μm. The small space causes diffraction near the edges of the structures in the mask. In other words, when light passes through the edge of the parts which are opaque, part of light goes to the place which should be dark. As a result, the resolution is not good compared to contact printing.

In proximity printing, the critical dimension l can be expressed as

$$l \approx \sqrt{\lambda g} \tag{1.1}$$

where λ is the wavelength of the light and g is the distance between mask and substrate. If λ or g *is* reduced, l becomes smaller. This can help to improve the resolution. However, for a fixed g, any dust particle which is larger than g will damage the mask.

In order to address the damage of the mask in shadow printing, projection printing which can avoid mask damage entirely is developed (shown in Fig.

1.4a). The image of the structures on the mask is projected onto the substrate. The distance between the mask and substrate can be centimeters. By moving the substrate, the whole substrate can be exposed. Usually there is size reduction built in the projection system which is called step-and-repeat projection system. However, 1:1 projection printing was not a long term solution for future generations of integrated circuit, since it became very difficult to make 1:1 masks with continuous reduction of minimum circuit feature size. Therefore, a reduction projection printing system was introduced. With a reduction projection (5:1) or (10:1) [8], features on a mask can be 5 or 10 times bigger than the projected images, which greatly eased mask fabrication. Since the projected patterns are 5 or 10 times smaller on the substrate, the same pattern can be repeated many times on the same substrate.

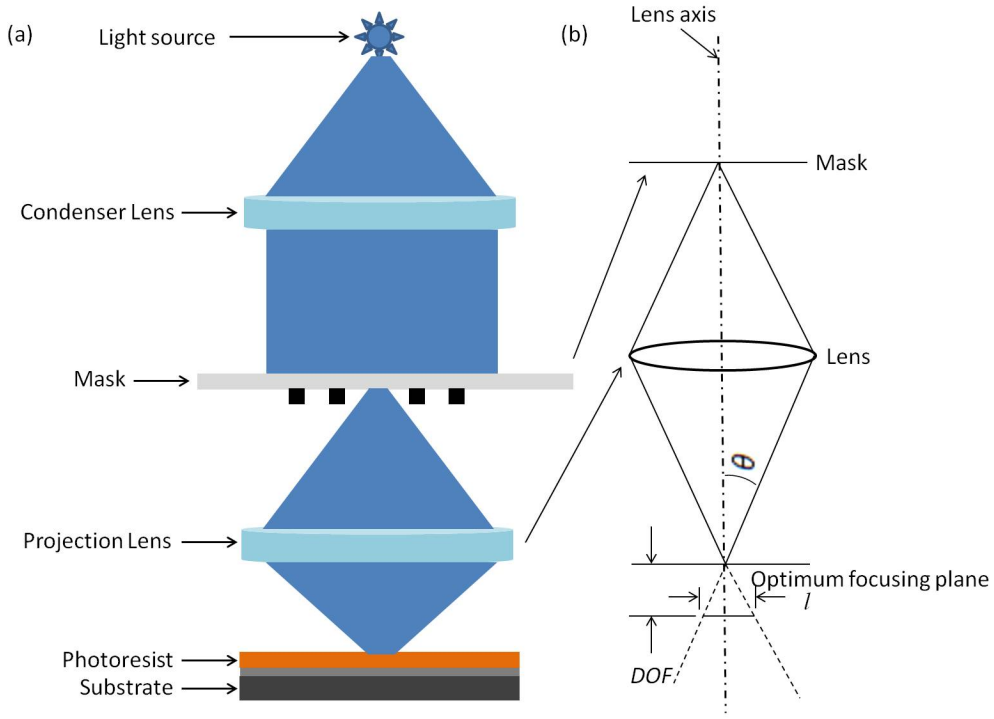

Fig. 1.4 Basic layout of a projection printing system

The resolution expressed in minimum feature size l of a projection printing system is

$$l = k_1 \frac{\lambda}{NA} \tag{1.2}$$

Where is the wavelength of the light, k_1 is a dimensionless factor determined by the exposure system and the photoresist which is typically 0.4 for production , *NA* is the numerical aperture. *NA* is

$$NA = n \sin\theta \tag{1.3}$$

Where n is refractive index of medium (n=1 for air), θ is convergence angle of the lens, as shown in Fig. 1.4b [6]. Fig. 1.4 also gives the depth of focus *DOF*,

$$DOF = \frac{\pm l/2}{\tan\theta} \approx \frac{\pm l/2}{\sin\theta} = k_2 \frac{\lambda}{NA^2} \tag{1.4}$$

Where k_2 is another dimensionless factor determined by the exposure system and the photoresist.

Equation (1.2) shows that reducing wavelength of light or increasing *NA* results in higher resolution (smaller *l*). However the *DOF* decreases as *NA* increases, and increasing *NA* has a larger effect on *DOF* than reducing wavelength of light as shown in Equation (1.4). As a result, reducing the wavelength of light becomes the inevitable trend of optical lithography.

Because of the high light intensity and degree of stability, mercury-arc lamp is widely used as the light source. There are several peaks in mercury-arc lamp, which are called G-line, H-line and I-line with the wavelength 436 nm, 405 nm and 365 nm respectively. Fig. 1.5 shows the spectrum of mercury-arc lamp [9].

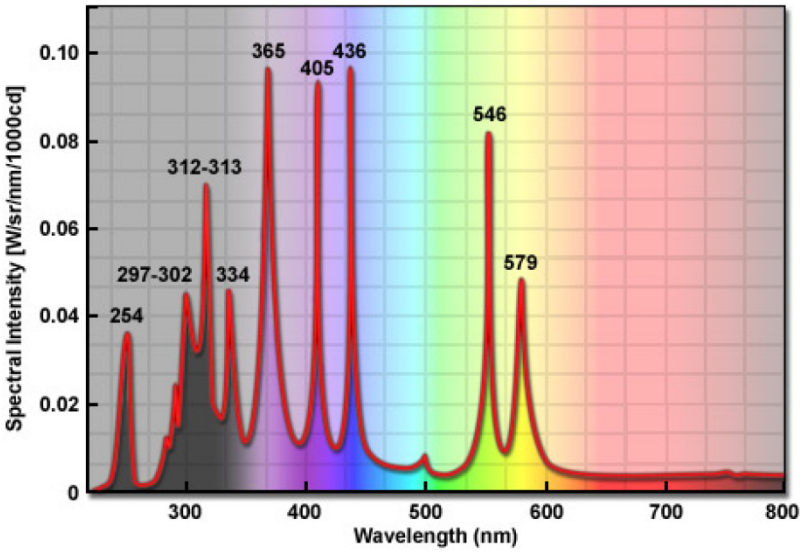

Fig. 1.5 Spectrum of a 100-watt high-pressure mercury plasma arc-discharge lamp

As can be seen from Fig. 1.5, for shorter wavelength, there is not enough intensity. Therefore more advanced photo exposure machine uses KrF excimer laser (248 nm), ArF excimer laser (193 nm) and F_2 excimer laser (157 nm) were developed. Excimer laser lithography has played a critical role in the continued advance of the so-called Moore's Law for the last 20 years [10]. The dominant lithography technology today is excimer laser lithography. The first wave of excimer lithographic systems operated with KrF lasers at 248 nm. These systems have been employed in patterning down to 130 nm lines and spaces. However, excimer lasers encompass a whole class of discharge gases and corresponding emission wavelengths [11]. Therefore, it is natural to explore the feasibility of ArF excimer laser lithography. Large efforts have been applied to the development of new photoresist platforms at 193 nm [12]. ArF excimer laser 193 nm systems were used in patterning 90 nm lines and spaces, and are expected to provide the platform for 65 nm and 45 nm lithography [13, 14]. Optical lithography has been extended to feature sizes below 50 nm using the 193 nm ArF excimer laser and liquid immersion techniques by increasing n (eq. 1.2 & 1.3). High-index lithography is the newest extension of 193 nm lithography to be considered. Using this technique, IBM has demonstrated features less than 30 nm [15]. For 157 nm

lithography, experimental tools were built, however due to the slow process because of the availability and cost of lens material [16,17], lack of organic pellicles [18], and slow progress in photoresist development [19, 20, 21, 22, 23], it has been abandoned.

1.3 Electron Beam Lithography (EBL)

Electron beam lithography (EBL) has been a preferred choice for many years to get resolution below 100 nm [24, 25]. Electron itself is a charged particle. We can get the wavelength of an electron according to wave-particle duality. Equation 1.5 [26] gives the wavelength of electron

$$\lambda_e = \frac{1.226}{\sqrt{V}} \text{ (nm)} \qquad (1.5)$$

where V is the energy of the electron in electron volt unit. From this equation, the wavelength of a 100 eV electron is only 0.12 nm. In addition, the higher the energy of the electron, the shorter of the wavelength. It is much smaller than the wavelength of light. Consequently, a focused electron beam is not limited by its wavelength and has potentially much better resolution compared to optical lithography. EBL has a history over 50 years. In 1958, researchers in MIT used a high energy electron beam to induce carbon pollution to get high resolution 2 dimensional structures [27, 28]. An electron beam in e-beam lithography system is normally acceletated to a kinetic energy between 10 keV to 100 keV. In 1965, 100 nm structures were fabricated by EBL [29]. In 1970, surface acoustic wave devices with 150 nm structures have been fabricated by EBL in polymethyl methacrylate (PMMA) resist [30]. The first commercial EBL machine was fabricated in 1977 [28]. In the current nanotechnology boom, EBL is an indispensable fabrication tool. A typical low electron energy beam is between 2 and 20 keV, 12 nm lines of 50 nm period grating with 50 nm thickness of HSQ was achieved using 10 keV electron beam [31]. A typical high electron beam energy is about 30, 50 and 100 keV. Less than 10 nm structures can be fabricated using 100 keV EBL combined with special

resist process technology [32]. The ultra high resolution capability and the direct write flexibility has made the EBL an important technology in research and development of micro and nanoscience.

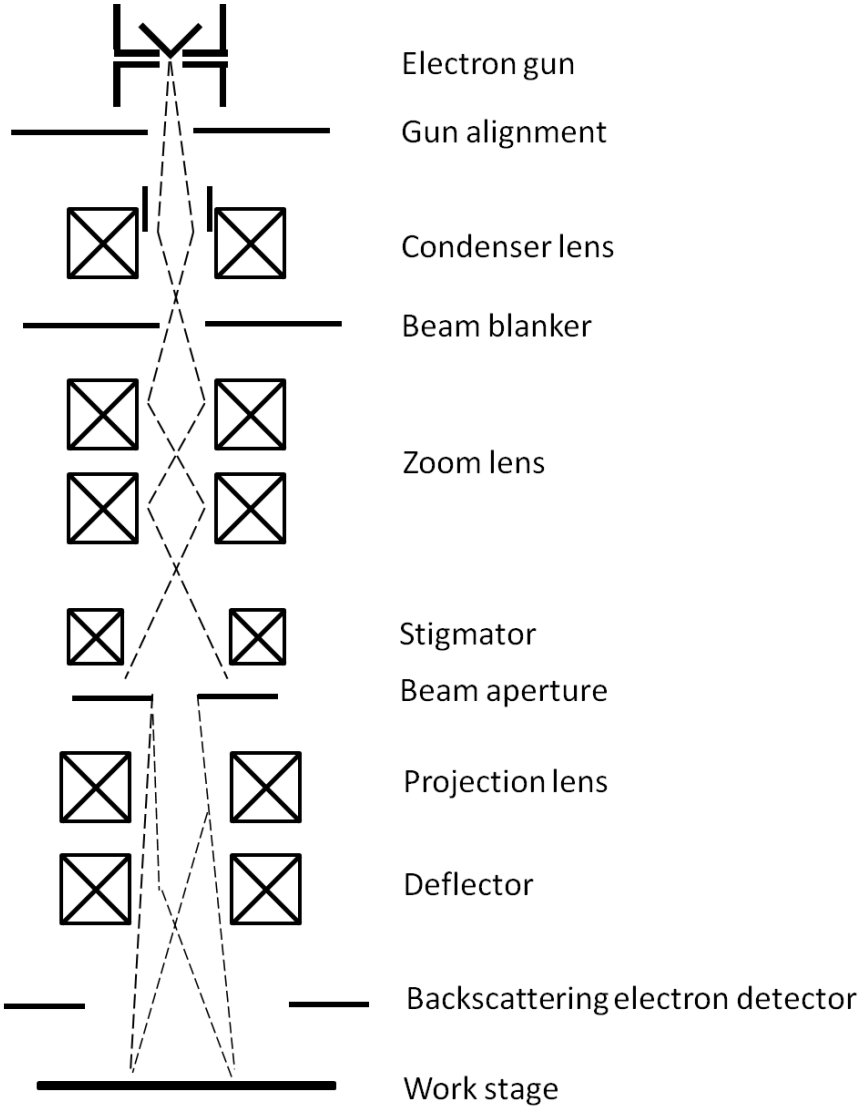

Fig. 1.6 Schematic of electron optical system in an e-beam lithography column

Fig. 1.6 shows a schematic drawing of an electron optical system in an e-beam lithography configuration. The electron column consists of the following sub-systems:

(1) Electron gun--- a component to generate electron beam with appropriate current density [33], usually uses tungsten, LaB_6 or field emission cathode as electron gun. The brightness of tungsten and LaB_6

electron guns is about $10^5 \sim 10^6/(A \cdot cm^{-2} \cdot sr^{-1})$. The field emission cathode guns can give a brightness of $10^8 \sim 10^9/(A \cdot cm^{-2} \cdot sr^{-1})$.

(2) Gun alignment---a deflection system to align the electron beam if an alignment is required. Spherical aberrations are high in electron columns, so only small openings can be used.

(3) Condenser lens---A combination of two separate lenses. Its function is (1) the primary de-magnifier for electron gun's crossover, and (2) converge the emitted electrons to make them arrive at the exposure surface in maximum numbers.

(4) Beam blanking---an electrostatic deflector which diverts the electron beam away from the optical axis allowing fast beam blanking

(5) Zoom lens---adjusts the focal plane, including dynamic focusing of electron beam.

(6) Stigmator---Astigmatism occurs when focusing of a beam is different in X and Y directions, resulting in an elliptical shape of beam instead of a circular beam. Stigmator consists of multipole lenses, it can focus beam laterally from different directions.

(7) Apertures---the size of aperture can be adjusted, a smaller aperture for high resolution and a larger aperture for high beam current at low resolution.

(8) Projection lens---the final lens of electron column, which focuses the electron beam to form the final beam spot at the exposure surface.

(9) Deflectors---realize electron beam scanning. It can be electrostatic or magnetic. A magnetic deflector has less aberration and distortion but slow deflection, whereas electrostatic deflection is of high speed but has large aberration.

(10) Backscattering electron detector--- inspect the exposure surface, find the alignment marks on the surface.

(11) Work stage---hold and move the substrate.

Until now EBL has not entered into the mass production arena, primarily because of its low throughput compared with optical lithography. However, EBL has a firm position in the technology chain of mask production of UV

and X-ray masks and high resolution patterning of specific devices. Efforts towards high throughput EBL systems are strong in USA and Europe pursuing high throughput electron beam systems either at low or middle range energies. High throughput EBL is considered as an alternative to the mass production of high resolution structures due to the high cost of high resolution patterning systems in 193 nm immersion lithography, and extreme ultraviolet lithography system.

1.4 Ion Beam Technologies

1.4.1 Focused ion beam (FIB)

Focused ion beams are all charged ions focused by electromagnetic field into a fine small beam. The main difference to EBL is their mass. The lightest ion (proton) is 1,840 times heavier than an electron. FIB usually uses very heavy ions (e.g. Ga^+) with energy of 20 ~ 50 keV.

Ion beam lithography can machine any material, this is a very important property [34]. FIB has very high sensitivity because the energy transfer between ions and atoms is much more efficient than between electrons and atoms. Commonly used electron beam resists are 100 times more sensitive to an ion beam than to electron beam. For example, PMMA only needs 0.1 $\mu C/cm^2$ exposure dose by gallium ion beam exposure at 100 keV, however, for EBL, it needs 20 $\mu C/cm^2$ exposure dose by 20 keV electron beam [35]. In this way, the exposure time becomes much less for the same beam brightness. However, if the resist is too sensitive, it can result in statistic noise. As the ion scattering is random, some ions cause fluctuation of statistic distribution of exposure dose, which results in edge roughness of exposed patterns. Another advantage of FIB is that it has no proximity effect. Because ions are much heavier than electrons, the scattering range of the secondary electron is much less than that of electrons. Experiments have shown that for dense lines exposure or exposure on substrate of high atomic number material, feature

dimensions achieved by ion beam lithography are the same as with light substrate material and for sparse lines [35].

As early as in 1989, sub-20 nm lines were achieved in PMMA using a Ga^+ beam [36]. In 1991, sub-10 nm wide lines were realized in PMMA using Ga^+ beam by the same group [37]. 6-nm diameter dots were fabricated on 5 nm thick HSQ using 20 keV helium ion beam [38].

The main drawback of ion beam lithography is its small penetration depth in resist. Monte Carlo analysis shows that a gallium ion beam at 250 keV energy can only expose PMMA to 0.25 μm depth. In this way, FIB lithography is only useful for patterning surface structures, other techniques should be combined for deep structures. For example, FIB lithography can pattern the top thin layer resist in a bilayer resist stack. A reactive ion etching process is followed to transfer top layer resist pattern to the under laying Si.

There are also some other applications of FIB. One application is to inspect and edit integrated circuits (IC). Using sputtering and deposition of FIB, it can connect or disconnect some parts of circuits on IC chips to correct errors in these chips. Another application is to repair defects of optical masks by ion sputtering. Also, FIB is nowadays used routinely to prepare transmission electron microscopy (TEM) samples for failure analysis [39, 40, 41, 42].

1.4.2 Proton Beam Writing (PBW)

Proton beams have been used in (contact) masked lithography since 1979 [43, 44], in early experiments Adesida [45] and Brenner et al [46] used low (200 keV) and high (8 MeV) energetic proton beams respectively for masked irradiation of PMMA resist materials. In this early work Adesida produced rather rough sub-100 nm features, whereas Brenner et al produced very high aspect ratio structures featuring lateral dimensions of tens of microns.

More recently proton beam writing (PBW) was introduced as a direct-write lithography process developed by Frank Watt and his colleagues at the Centre

for Ion Beam Applications (CIBA), Department of Physics, National University of Singapore.

PBW uses a focused beam of high energy protons to pattern resist material at nano-dimensions. The process, although similar in many ways to direct writing using electrons, nevertheless offers some interesting and unique advantages.

The main advantage of PBW is that protons have a straight deep well-defined path and range in resist [47]. Calculations have also indicated that PBW exhibits minimal proximity effects (unwanted exposure due to secondary electrons) [48], since the secondary electrons induced in proton/electron collisions have low energies [48, 49, 50, 51]. These features enable PBW with great capability to fabricate high aspect ratio micro- and nanostructures with vertical and smooth sidewalls [52]. PBW can also be applied to produce pillars, trenches and arbitrary structures in both polymer and Si substrates for applications in optics (e.g. waveguides, laser arrays and gratings) [53, 54] and fluidics (micro-fluidic devices, biostructures and biochips) [55, 56, 57]. Protons with different energy can stop at different depth of resist. Therefore, applying different energies, PBW can perform machining in multilayers to form stacked structures in resist, and Si modifications including Si fabrication and porous Si patterning [58, 59, 60, 61, 62].
Since its establishment at the end of the last century, PBW has undergone many technical improvements, and great efforts have been made to expand its practical applications. Now high aspect ratio structures down to 22 nm have been fabricated with PBW in resist HSQ [63]. PBW technique will be discussed in greater detail in the next chapter.

1.4.3 Ion projection lithography (IPL)

Ion projection lithography (IPL) was developed at the Institute of Microfabrication Systems (IMS) in Austria in 1985 [64]. The difference between FIB and IPL, is that IPL is a masked process like optical projection

lithography [65]. In the IPL system, a stencil mask is irradiated with a uniform light beam of ions, H^+, H_2^+, or He^+, and the transmitted pattern is de-magnified by 3 or 10 times and focused on a resist covered wafer at energies in the 70 to 150 keV range [66]. Commonly used stencil masks consist of a thin Si membrane with patterned openings. In order to avoid forbidden geometrics and stress relief distortion of the stencil mask, thin, continuous-membrane, single crystal, channeling masks have been used [67, 68, 69]. With recent developments in the mask fabrication process, electrostatic lenses, and resist materials, IPL has demonstrated resolution of 50 nm in 2002 [70, 71, 72]. In 2009, 12.5 nm dots and lines were fabricated in 20 nm thick HSQ with 10 keV H_3^+ [73].

1.5 X-ray lithography

X-ray is electromagnetic radiation with wavelengths from 0.01~10 nm. It was first discovered by Wilhelm Röntgen in 1895. In the past 100 years, X-ray has become one of the most powerful tools in scientific research. The most famous discovery with the aid of X-ray is the DNA double helix structure [74]. In this section, I will introduce X-ray lithography.

The X-ray lithography technique was first developed by Henry Smith of MIT in the early 1970s [75]. X-rays can penetrate most of the materials, only some materials with high atomic number can absorb X-rays (all matter absorb X-rays but low atomic number absorbs less). X-ray cannot be focused like light, because the index of refraction of X-ray in all the materials is nearly 1. As a result, X-ray lithography is only 1:1 lithography. Fig. 1.7 shows the schematic of X-ray lithography.

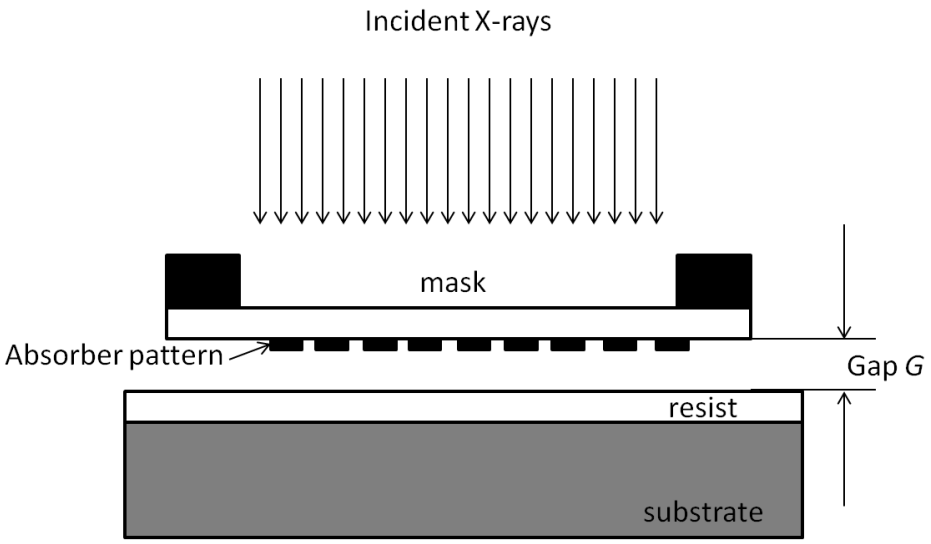

Fig. 1.7 Schematic of X-ray lithography

When X-rays pass through the mask, low atomic number materials are transparent to X-rays, while high atomic number materials, such as Au, W, Ta, absorb and block the X-rays. For X-rays whose wavelength is 1 nm, the thickness of Si membrane is about 1~2 μm and the thickness of the heavy metals is about 300~500 nm. The exposure depth in resist is 1 μm and the proximity gap between X-ray mask and substrate is 5~50 μm [76]. Because X-ray lithography is direct projection (1:1), the structures in the mask must be the same size as the image structures. For sub-100 nm lithography, the metal absorber structures should be smaller than 100 nm. In addition, the thickness of the mask is only several μm, therefore any residual stress can cause distortion in the mask patterns. Another difficulty for X-ray is the gap between mask and substrate. To get high resolution structures with X-rays, the gap should be less than 10 μm. In order to better control the gap, the flatness of the Si wafer has to be within ±0.25 μm and the flatness of the mask within ±0.5 μm [77]. The requirement for the flatness is very difficult to be realized for both Si wafer and mask. Besides, the cost for X-ray lithography is too high. High brightness X-ray can only be obtained from a synchrotron. Construction of a large scale synchrotron radiation facility costs over $100 million. From a low cost and high throughput point of view, X-rays are not a candidate as next

generation lithography tools. However, it may play a role in small-scale production, particular for special semiconductor devices such as GaAs integrated circuits. Researchers have fabricated surface acoustic wave devices [78], bipolar transistors and MOS transistors [79, 80] using X-ray lithography. In 1994, X-ray lithography was already capable of fabricating 85 nm MOSFET devices in a laboratory environment [81]. By 1995 IBM was able to produce very large scale integration (VLSI) chips with size down to 0.25 μm using X-ray lithography [82]. In 2011, a sub-μm photon sieve was fabricated using E-beam lithography and X-ray lithography, which provided a direction of nanoscale optical element fabrication with higher resolution and lower cost [83].

1.6 Summary

Table 1.1 shows a very simple comparison of optical lithography, EBL, PBW, FIB, and X-ray lithography in PMMA.

	Optical lithography	X-ray lithography	EBL	PBW	FIB
Source property	248 nm [84]	8.3 Å [84]	20 keV-50 keV [84]	2 MeV Proton [58]	100 keV Ga^+ [35]
Sensitivity	500 mJ/cm^2	1-2 J/cm^2	50-500 $\mu C/cm^2$	10 $\mu C/cm^2$	0.1 $\mu C/cm^2$

As can be seen from this table, optical lithography is more effective than X-ray lithography. For EBL, PBW and FIB, the best sensitivity is achieved in FIB at the expense of nuclear damage, the lowest sensitivity is achieved in EBL.

Fig. 1.8 shows a comparison of these different kinds of lithographic techniques.

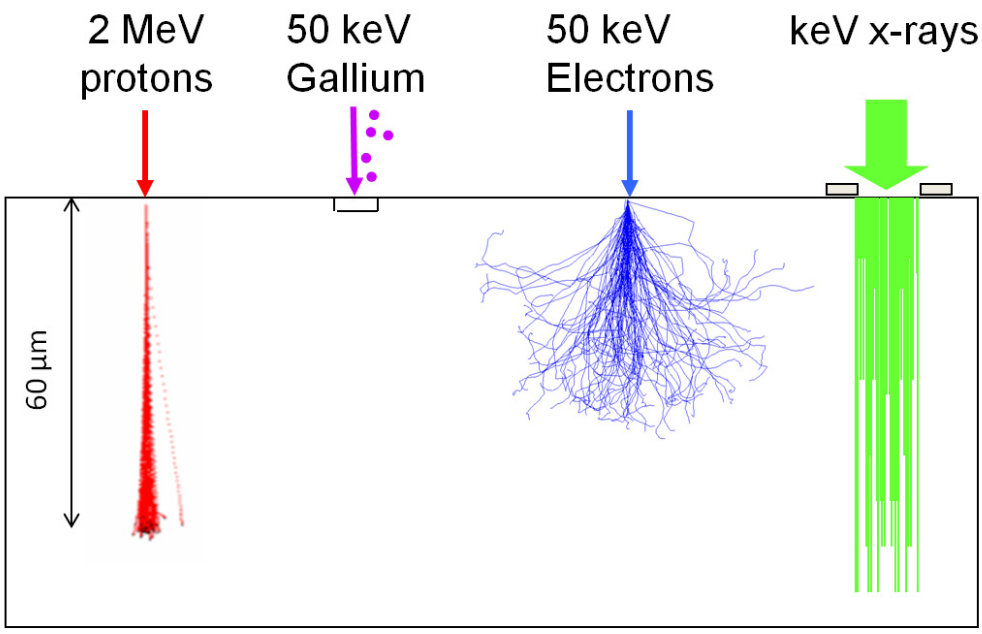

Fig. 1.8 Comparison among PBW, FIB, EBL and X-ray lithography. The p-beam and e-beam images were simulated using SRIM and CASINO software packages, respectively.

As can be seen from Fig. 1.8, PBW is capable of high aspect ratio structure fabrication with small features (down to 19 nm [85]) and vertical and smooth sidewall. Calculations by Udalagama et al [48] show that secondary electrons induced in PBW only travel several nano meters. FIB has ability to fabricate structures down to 6 nm in a 5 nm thick HSQ at the expense of nuclear damage [38]. The penetration depth is very small limiting layer thick ness typically less than 10 nm, with significant nuclear damage to the substrate. EBL also has high resolution (less than 10 nm in HSQ [32]), but the penetration depth of electron is also very small and proximity effects complicate large area nano structure fabrication; as a result FIB and EBL are suitable for 2D nano fabrication. X-ray lithography is capable of fabricating either high aspect ratio microstructures or high resolution (30 nm) structures with low aspect ratio, however the mask for X-ray lithography is very expensive.

In this project “metal mold fabrication and its applications for mass production of micro and nano components”, since structures with high resolution, high

aspect ratio, vertical and smooth sidewall are needed. In addition, protons are very efficient in exposing resist. As a result, PBW is the appropriate technique for this project.

References

[1] Zheng Cui, *Micro-Nanofabrication Technologies and Applications*, p 28, 2005

[2] G.H. Bernstein, D.A. Hill, On the attainment of optimum developer parameters for PMMA resist, Superlattices and Microstructures, V11, 1992, 237-248

[3] S. Bolhuis, J.A. van Kan, F. Watt, Enhancement of proton beam writing in PMMA through optimization of the development procedure, NIMB 267 (2009) 2302-2305

[4] W. Henschel, Y.M. Georgiev, H. Kurz, Study of a high contrast process for hydrogen silsesquioxane as a negative tone electron beam resist, J. Vac. Sci. Technol. B 21, 2018, 2003

[5] J.A. van Kan, A.A. Bettiol, F. Watt, Hydrogen silsesquioxane a next generation resist for proton beam writing at the 20 nm level, NIMB 260 (2007) 396-399

[6] M. C. King, *Principles of Optical Lithography*, in N. G. Einspruch, Ed., VLSI Electronics, v 1, Academic, New York, 1981

[7] J. H. Bruning, *A Tutorial on Optical Lithography*, in D. A. Doane, D. B. Fraser, and D.W. Hess, Eds. Semiconductor Technology, Electrochemical Soc., Penningston, 1982

[8] Simon Sze, *Semiconductor devices: Physics and Technology*, p 396, 2008

[9] http://zeisscampus.magnet.fsu.edu/articles/lightsources/mercuryarc.html

[10] La Fontaine, B., *Lasers and Moore's Law*, SPIE Professional, p. 20, 2010

[11] M. Rothschild, *projection optical lithography*, materials today, v 8, n 2, p 18-24, 2005

[12] Allen R. D., Wallraff G. M., Hofer D. C., Kunz R. R., *Photoresists for 193-nm lithography* IBM J. Res. Dev v41, p 95-104, 1997

[13] Matsuyama, T. Ishiyama, T., Ohmura, Y., *Nikon projection lens update*, Proc. SPIE, v5377, n 1, p 730-41, 2004

[14] Fuard, D., Schiavone, P., *Comparison of various lithography strategies for the 65- and 45-nm half pitch using simulation*, Proc. SPIE, v5377, n 1, p 1360-74, 2004

[15] Hand, Aaron., *High-Index Lenses Push Immersion Beyond 32 nm*, 2006

[16] Bloomstein, T. M., Rothschild, M., Kunz, R. R., Hardy, D. E., Goodman, R. B., Palmacci, S. T., *Critical issues in 157 nm lithography*, J. Vac. Sci. Technol. B, v16, n 6, p 3154-7, 1998

[17] Burnett, J. H., Levine, Z. H., *Intrinsic birefringence in calcium fluoride and barium fluoride*, Phys. Rev. B, v64, 2001

[18] Grenville, A., Liberman, V., Rothschild, M., Sedlacek, J.H.C., French, R.H., Wheland, R.C., Zhang, X., Gordan, J., Proc. SPIE, v4691, p 1644-53, 2002

[19] Bloomstein, T.M., et al., *Critical issues in 157 nm lithography*, J. Vac. Sci. Technol. B 16 (6), 3154-3157, 1998

[20] Crawford, M.K., Farnham, W.B., Feiring, A.E., Feldman, J., French, R.H., Leffew, K.W., Petrov, V.A., Qiu, W, Schadt, F.L., Tran, H.V., Wheland, R.C., Zumsteg, F.C., *Single layer fluoropolymer resists for 157 nm lithography*, Proc. SPIE, v5039, p 80-92, 2003

[21] Houlihan, F.M., Sakamuri, R., Romano, A., Rentikiewicz, D., Dammel, R.R., Conley, W.E., Miller, D.A., Sebald, M., Stepanenko, N., Markert, M., Mierau, U., Vermeir, I., Hohle, C., Itani, T., Shigematsu, M., Kawaguchi, E., *Recent advantages in fluorinated resists for application at 157 nm*, Proc. SPIE, v5376, n 1, p 134-50, 2004

[22] Yamazaki, T., Furukawa, T., Itani, T., Ishikawa, T., Koh, M., Araki, T., Toriumi, M., Kodani, T., Aoyama, H., Yamashita, T., *Development*

and characterization of new 157-nm photoresists based on advanced fluorinated polymers, Proc. SPIE, v5039, p 103-12, 2003

[23] Otoguro, A. Irie, S., Ishimaru, T., Suganage, T., Itani, T., Fujii, K., *157-nm resist assessment by a full-field scanner*, Proc. SPIE, v5376, n 1, p 245-53, 2004

[24] Henini. M, *EBL opening up the nano-world*, III-Vs Review, v 12, n 6, p 18, 1999

[25] Mauer, J.L., Pfeiffer H.C., Stickel W., *Electron-optics of an electron-beam lithographic system*. IBM J. Res. Dev., v26, p 568, 1977

[26] Grivet P. Electron Optics. Pergamon Press, 1965

[27] Buck, D.A., Shoulders, K.R., Proc. Eastern Joint Computer Conf., p. 55–59, 1959

[28] Hahmann P. Fortagne O. *50 years of electron beam lithography: contribution from Jena (Germany)*, in 34th International Conference on Micro & Nano Engineering,2009

[29] Broers A N, *Combined electron and ion beam processes for microelectronics. Microelectronics and Reliability*, 4: 103-104, 1965

[30] Lean, E.G., Broers, A.N., *Microwave surface acoustic delay lines*. Microwave J., v13, n 3, p 97-101, 1970

[31] Haifang Yang, Aizi Jin, Qiang Luo, Changzhi Gu, Zheng Cui, Yifang Chen, Low-energy electron beam lithography of hydrogen silsesquioxane, Microelectronics Engineer 83 (2006) 788-791

[32] Muhammad M. Mirza, Haiping Zhou, Philippe Velha, Xu Li, Kevin E. Docherty, Antonio Samarelli. Gary Ternent, Douglas J. Paul, *Nanofabrication of high aspect ratio (~ 50:1) sub-10 nm silicon nanowires using inductively coupled plasma etching*, J. Vac. Sci. Technol. B 30, 06FF02 (2012)

[33] D.P. Kern, P. J. Coane, P. J. Houzego, and T. H. P. Chang, *Practical Aspects of Microfabrication in 100 nm Region*, Solid State Technol., v27, n 2, p 127(1984)

[34] F. Watt, A. A. Bettiol, J. A. Van Kan, E. J. Teo, and M. B. H. Breese. *Ion beam lithography and nanofabrication: a review*. International Journal of Nanoscience, v 4, n 3, p 269–286, 2005.

[35] Matsui S, et al, *Lithography approach for 100nm fabrication by focused ion beam*, J.Vac.Sci.Technol., B4, p.845, 1986

[36] R. L. Kubena, F. P. Stratton, J. W. Ward, G. M. Atkinson, and R. J. Joyce, *Sub-20-nm-wide line fabrication in poly(methylmethacrylate using a Ga^+ microprobe,* J. Vac. Sci. Technol. B **7**, 1989

[37] R. L. Kubena, J. W. Ward, F. P. Stratton, R. J. Joyce, and G. M. Atkinson, *A low magnification focused ion beam system with 8 nm spot size*, J. Vac. Sci. Technol. B 9, 3079, 1991

[38] V. Sidorkin, E. van Veldhoven, E. van der Drift, P. Alkemade, H. Salemink, D. Mass, *sub-10-nm nanolithography with a scanning helium beam*, J. Vac. Sci. Technol. v 27, n4,18-20, 2009

[39] J. Mayer, L. A. Giannuzzi, T. Kamino, and J. Michael, *TEM sample preparation and FIB-induced damage*, MRS Bulletin, vol 32, pp. 400-407, 2007.

[40] R. Langford, *Preparation for physic-chemical analysis, in Focused Ion Beam Systems: Basics and Applications*, chapter 8, N. Yao, Eds. Cambridge University Press, pp. 215-249, 2007

[41] C. A. Volkert and A. A. Minor, *Focused ion beam microscopy and micromachining*, MRS Bulletin, v 32, pp.389-395, 2007

[42] J. Zhu, Q.X. Wang, C.Q. Chen, S.P. Neo, A.Y. Du, Y.N. Hua, *FIB sample preparation for TEM failure analysis of advanced devices*, 17th IEEE International Symposium on the Physical and Failure Analysis of Integrated Circuits, p 5, 2010

[43] R.L. Seliger, R.L. Kubena, R.D. Olney, J.W. Ward,V. Wang, *High resolution ion-beam processes for microstructure fabrication*, J. Vac. Sci. Technol. 16 1610, 1979

[44] M.B.H. Breese, G.W. Grime, F. Watt, *MeV ion beam lithography of PMMA*, Nucl. Instr. and Meth. B 77 169-174, 1993

[45] Ilesanmi. Adesida, Fine line lithography using ion beams, Nucl. Instr. Meth. B7/8 (1985) 923-928

[46] K.H. Brenner, M. Frank, M. Kufner, S. Kufner, H^+ lithography for 3-D integration of optical circuits, Applied optics V29, NO. 26, 1990

[47] J. A. van Kan, T. C. Sum, T. Osipowicz, and F. Watt. *Sub 100 nm proton beam micromachining: theoretical calculations on resolution limits*, Nucl. Instr. and Meth. B, 161:366–370, 2000

[48] C. Udalagama, A. A. Bettiol and F. Watt, *Stocastic spatial energy deposition profiles for MeV protons and keV electrons*, Physical Review B 80 224107, 2009

[49] Zhang Chunxiang, D.E. Dunn, R. Katz, *Radial distribution of dose and cross-sections for the intactivation of dry enzymes and viruses*, Radiat. Protect. Dos. 13, 215, 1985

[50] M.P.R. Waligorski, R.N. Hamm, R. Katz, *The radial distribution of dose around the path of a heavy ion in liquid water*, Nucl. Tracks Radiat Meas 11 309, 1986

[51] W.H. Barakas, Nuclear Research Emulsions, Academic Press, New York, v1, p. 371, 1963

[52] J.A. Van Kan, A.A. Bettiol, K. Ansari, E.J. Teo, T.C. Sum, and F. Watt, *Proton beam writing: a progress review*, International Journal of Nanotechnology, 4:464–479, 2004

[53] A. A. Bettiol, S. Venugopal Rao, E.J. Teo, J. A. van Kan, and Frank Watt, *Fabrication of buried channel waveguides in photosensitive glass using proton beam writing*, Applied Physics Letters, 88:171106, 2006

[54] A.A. Bettiol, T.C. Sum, F.C. Cheong, C.H. Sow, S. Venugopal Rao, J.A. van Kan, E.J. Teo, K. Ansari, and F. Watt, *A progress review of proton beam writing applications in microphotonics*, Nuclear Instruments and Methods in Physics Research B, 231:364–371, 2005

[55] J.L. Sanchez, G. Guy, J.A. van Kan, T. Osipowicz, and F. Watt, *Proton micromachining of substrate scaffolds for celluar and tissue*

engineering, Nuclear Instruments and Methods B, v 158, p 185-189, 1999

[56] K. A. Mahabadi, I. Rodriguez, S. C. Haur, J. A. van Kan, A. A. Bettiol, and W. Frank, *Fabrication of PMMA micro- and nanofluidic channels by proton beam writing: electrokinetic and morphological characterization*, J. Micromech. Microeng., 16:1170–1180, 2006

[57] J. A. van Kan, C. Zhang, P. Malar and J. R. C.van der Maarel, *High throughput fabrication of disposable nanofluidic lab-on-chip devices for single molecule studies*, Biomicrofluidics, 6, 036502, 2012

[58] J.A. van Kan, J.L. Sanchez, B. Xu, T. Osipowicz, F. Watt, *Resist materials for proton micromachining*, Nuclear Instruments and Methods in Physics Research B 158 p179-184, 1999

[59] J.A. van Kan, J.L. Sanchez, T. Osipowicz, F. Watt, *Proton micromachining: a new technique for the production of three-dimensional microstructures*, Microsystem Technologies 6 82-85, 2000

[60] E. J. Teo, M. B. H Breese, E. P. Tavernier, A. A. Bettiol, F. Watt, M. H. Liu, and D.J. Blackwood, *Three-dimensional microfabrication in bulk silicon using high-energy protons*, Applied Physics Letters, 84:3202–3204, 2004

[61] M.B.H. Breese, E.J. Teo, D. Mangaiyarkarasi, F. Champeaux, A.A. Bettiol, and D. Blackwood, *Proton beam writing of microstructures in silicon*, Nuclear Instruments and Methods in Physics Research B, 231:357–363, 2005.

[62] E.J. Teo, M.B.H. Breese, A.A. Bettiol, D. Mangaiyarkarasi, F. Champeauz, F. Watt, and D. Blackwood, *Multicolour photoluminescence from porous silicon using focused high-energy helium ions advanced materials*, Journal of Laboratory and Clinical Medicine, 18:51–55, 2006

[63] J. A. van Kan, A. A. Bettiol, and F. Watt, *Proton beam writing of 3D nanostructures in hydrogen silsesquioxane*, Nano Letters, 6:579–582, 2006

[64] G. Stengel, H. Loschner, W. Maurer, and P. Wolf, *Current status of ion projection lithography,* Proc. SPIE **537**, pp. 138–145, 1985

[65] F. Watt, A. A. Bettiol, J. A. van Kan, E. J. Teo, and M. B. H. Breese. *Ion beam lithography and nanofabrication: a review*, International Journal of Nanoscience, 4(3):269–286, 2005

[66] J. Melngailis, A.A. Mondelli, I.L. Berry, and R. Mohondro, *A review of ion projection lithography*, J. Vac. Sci. Technol. B, 163:927–957, 1998

[67] J. L. Bartlett, Solid State Technol. 29, 215, 1996

[68] L. Cspergi, F. Iberl, and P. Eichinger, *Ion-beam shadow printing through thin silicon foils using channeling*, Appl. Phys. Lett. v 37,p 630, 1980

[69] G. M. Atlinson, J. L. Bartlet, A. R. Neureuther, and N. W. Cheung, *The characterization and optimization of masked ion beam lithography with <100> silicon channeling masks*, J. Vac. Sci. Technol. B 5, 232, 1987

[70] R Kaesmaier, A. Ehrmann, and H. Loschner, *Ion projection lithography: Status of tool and mask developments*, Microelectronic Engineering, 57-58:145-153, 2001

[71] G. Stengl, H. Loeschner., *Large field particle beam optics for projection and proximity printing and for maskless lithography*, SPIE Journal of Microlithography, Microfabrication and Microsystems, 2:34-48, 2003.

[72] S. Hirscher, M. Kummel, O. Kirch, W.-D. Domke, A. Wolter, R. Kasmaier, H. Buschbeck, E. Cekan, A. Chalupk, A. Chylik, S. Eder, C. Horner, H. Loschner, R. Nowak, G. Stengl, T. Windischbauer, and M. Zeininger, *Ion projection lithography below 70 nm: tool performance and resist process*, Microelectronic Engineering, 61–62:301–307, 2002

[73] Platzgummer. E, *Maskless Lithography and Nanopatterning with Electron and Ion Multi-Beam Projection*, The International Society for Optical Engineering, v 7637, p 763703, 2010

[74] Smith H I., *100 years of X-rays: Impact on micro and nanofabrication*, J.Vac.Sci. Technol., B13(6), p.2323, 1995

[75] Spears, D.L., Smith, H.I., *X-ray lithography-a new high resolution replication process*, Solid State Technology, v 15, n 7, p 21-6, July 1972

[76] Smith, H.I., Cerrina, F., *X-ray lithography for ULSI manufacturing*, Microlithography world, V.6(1), p 10, 1997

[77] Krasnoperva, A. A., et al., *Imaging capability of proximity X-ray lithography at 70 nm ground rule*, SPIE, V.3676, p.24, 1999

[78] Smith, H.I., Spears, D.L., Bernacki, S.E., *X-ray Lithography: A complementary technique to electron beam lithography*, J. Vac. Sci. Technol., v 10,p 913, 1974

[79] Bernacki, S.E., Smith, H.I., Proceedings 6th International Conf. Electron and Ion beam Science and Technology, 1974

[80] Bernacki S.E., Smith, H.I., *Fabrication of Silicon MOS Devices using X-ray Lithography*, IEEE Trans. Electron Devices, ED-22, p.421, 1975

[81] Yang, I.Y., *High performance self-aligned sub-100nm MOSFET using X-ray lithography*, J. Vac. Sci. Technol.,B12,p 4051, 1994

[82] Dellaguardia, R., *Fabrication of a 64Mbit DRAM using X-ray lithography*, SPIE, V.2144, p.112, 1995

[83] Wenbo Jiang, Song Hu, Changqing Xie, Xiaoli Zhu, Weicheng Xie, Jun Wang, Xiucheng Dong, *Fabrication of submicron photon sieve using E-beam lithography and X-ray lithography*, Microelectronic Engineering, v88, n 10, p 3178-81, 2011

[84] http://depts.washington.edu/ntuf/facility/docs/PMMA_Data_Sheet.pdf

[85] Y. Yao, P.S. Raman, J.A. van Kan, *Orthogonal and fine lithographic structures attained from the next generation proton beam writing facility*, 2013, Submitted to microsystem technologies

Chapter 2 Proton beam writing

In this chapter, I will give more details on proton beam writing (PBW), including the PBW facility and the procedures of PBW. In addition, several new resists that can be used in PBW and are potentially compatible with Ni plating will be introduced.

2.1 Proton beam writing set up

PBW is introduced in the Center for Ion Beam Applications (CIBA) in the physics department of the National University of Singapore (NUS), by Professor Frank Watt and his colleagues. CIBA is a state-of-the-art research centre utilizing advanced high energy (MeV) ion beam techniques covering a wide range of disciplines, including biophysics, lab-on-a-chip technology, nuclear microscopy of degenerative diseases, micro-photonics, advanced materials characterization and semiconductor micromachining.

In CIBA, there is a 3.5 MV high voltage single-ended accelerator made by High Voltage Engineering Europa (HVEE Singletron) [1]. A high energy section with a steerer table, a 90° analyzer magnet, a high energy switching magnet and 5 advanced beam lines are directly connected to the accelerator. The 5 advanced beam lines are: the high resolution RBS facility (1), the nuclear microscope cell and tissue imaging beam line (2), the nano-imaging beam line (3), the second generation proton beam writing facility (4) and the 1st generation proton beam writing beam line (5) as shown in Fig. 2.1. Now the proton beam writer prototype is widely used by our colleagues for PBW. The 2nd generation proton beam writing facility is still under development and is currently tested for its lithographic performance. In this section I will mainly cover the 1st generation proton beam writer and high voltage accelerator.

The HVEE Singletron accelerator can generate energetic proton beams up to 3.5 MeV with much higher energy stability than the more common belt-driven Van de Graaff accelerators [1, 2]. Protons are generated from a RF (Radio Frequency) source with high brightness and stability. The RF ion source is a long life (3000 h) ion source containing a gas which is excited by an RF oscillator. After the protons and H_2^+ are extracted into the beam pipe, they pass through a 90° magnet and the desired mass and energy are selected. Then the protons pass through a 1 mm round aperture, directly followed by rectangular object slit apertures which are positioned one meter in front of the switcher magnet. The object slits aperture is defined by 4 tungsten carbide cylinders. Typical object sizes range from 1-1000 μm and are adjusted manually. The switching magnet can be adjusted to guide the beam into any of the 5 beam lines. For PBW, protons will be guided into the proton beam writer prototype.

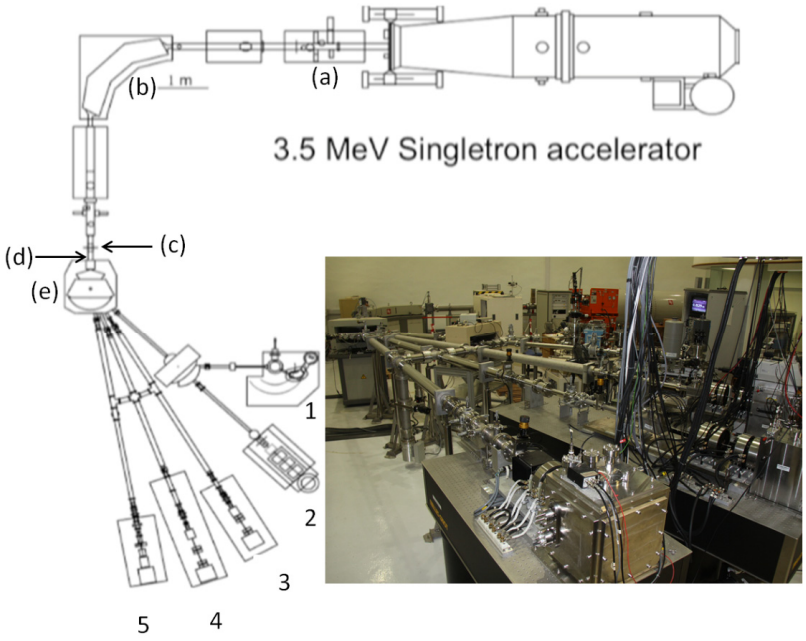

Fig. 2.1 CIBA Singletron accelerator and beam line applications: (a) X_1, X_2, Y_1, Y_2 Steerers (b) 90° analyzing magnet (c) Objective slits (d) Blanking system (e) switcher magnet; (1) the high resolution RBS facility; (2) the nuclear microscope; (3) the cell and tissue imaging beam line; (4) the next generation proton beam writing facility; (5) the proton beam writer prototype [3]

Proton beam focusing system

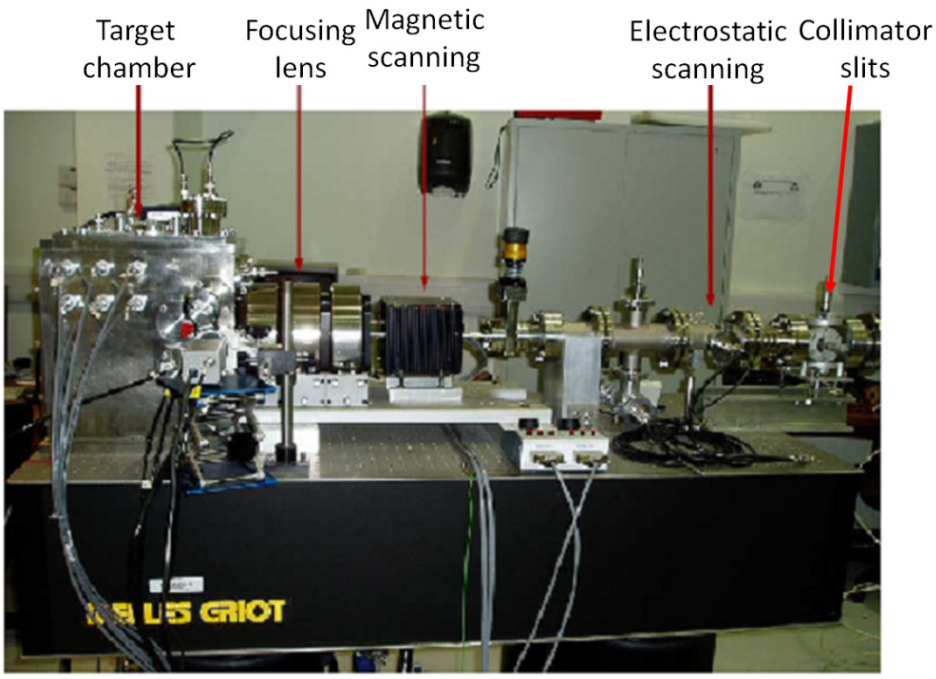

Fig 2.2 The main facilities of the proton beam writer prototype

Fig. 2.2 shows the end-station of the CIBA proton beam writer. As can be seen from this figure, three OM52 magnetic quadrupole lenses from Oxford Microbeams [4] are installed in an Oxford triplet configuration [5] in front of the target chamber. The distance from the object to the lenses and the distance from the lenses to the image plane is 7 m and 70 mm respectively. The demagnification of this focusing system is 228 × 60 in lateral and vertical direction [6]. MeV proton beam can be easily focused down to sub-100 nm with this 1st generation PBW configuration [7].

Scanning and blanking system

As shown in Fig. 2.2, there is a set of magnetic scan coils in front of the lenses. The magnetic scan system can scan the beam across an area up to 0.5 × 0.5 mm^2 in a single scan field.

The blanking system uses a 5 V logic control to power a +/-180 V HV amplifier with a slew rate of 1000 V/μs. This HV amplifier supplies an electrostatic potential between a set of parallel copper plates. It is placed just before the switching magnet. The blanking system is to prevent unwanted exposure by applying a voltage to deflect the proton beam from its original path. A fast deflection time (<1 μs) is applied.

Fig 2.3 shows a schematic diagram of the scanning and control hardware setup at CIBA [8]. The scanning and blanking systems are driven by computer data acquisition (DAQ) cards from National Instruments ^{TM}. The cards are chosen to perform the functions of (1) beam manipulation through the driving of scan amplifier with a minimum update time of 1.0 μs; (2) beam blanking by a 16 bit supplying the blanking amplifier 5 V which is amplified to ±100 V on the blanking plates; (3) beam normalization by means of a 20 MHz counter-timer to collect signal from either RBS or electron detection.

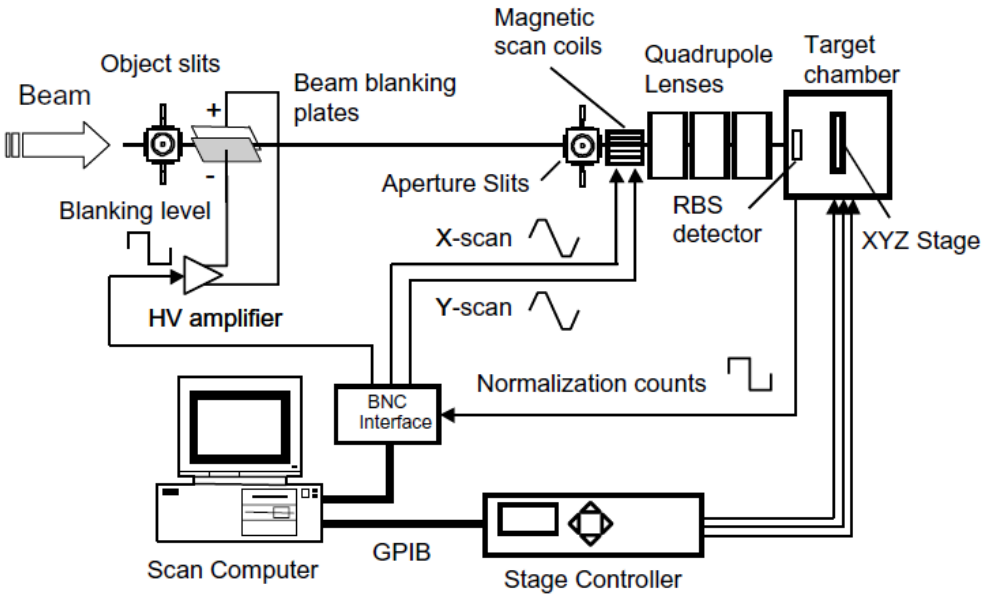

Fig. 2.3 Schematic diagram of the scanning and control hardware setup at the Centre for Ion Beam Applications, National University of Singapore proton beam writer

Target chamber

At the end station of the proton beam writer prototype, there is a stainless steel target chamber that can be operated in 10^{-6} mbar range. Inside the chamber, there is an EXFO Burleigh Inchworm® TSE-820-V XYZ stage controlled by a National Instruments GPIB card. The Inchworm® stage can provide a total movement of 2.5 cm in X, Y and Z directions. The minimum step size (Encoder resolution) is 20 nm, and the maximum stage speed is 1.5 mm/s. In addition, there is an optical microscope connected with a CCD camera to monitor the position of the sample; an annular Rutherford Backscattering (RBS) detector for exposure dose normalization; a channeltron detector for beam focusing and imaging through the detection of proton induced secondary electrons.

Software

At the Center for Ion Beam Applications, National University of Singapore, A.A. Bettiol *et al* have developed a suite of programs known as *Ionscan* which is written with the *Microsoft Visual C++*. The first version was developed using *LabVIEW* [9], now many new features have been added into the software, e.g. the ability to perform combined stage and magnetic scanning. The software encompasses scan file conversion, resist calibration, dose calculation, scan parameters settings and automated serial writing. The software is compatible with many file types: BMP (Monochrome Bitmap in 2^n resolution typically 1024^2 to 4096^2), TXT (ASCII format. List of X and Y co-ordinates in native resolution), EMC (the *emc* file is an ASCII file with an *.emc* extension---Ionscan *emc* file version 1) and EPL (Ionscan *epl* version format). This last file format allows the user to define several basic shapes that can be easily converted to the *.epl* format for PBW. The *emc* shapes, called entities, contain information on their design (e.g. the radius and centre co-ordinates) and more importantly the order in which the points within the shape are scanned. An example of the *emc* file format is shown in Fig. 2.4, and the corresponding figure generated by this file is shown in Fig.2.5. Fig. 2.6 shows the order in which points are scanned for the four basic shapes that are currently supported by the *emc* file format. Rectangles can be raster scanned with a silhouette which helps to smooth out edge distortions that can occur due to magnetic hysteresis in the scanning system. The silhouette is written by scanning the beam along the edge of a shape. Spiral scanning can also improve the edge roughness for circles and squares. In the spiral square case, the beam scanning always begins and ends in the center of the shape. This scan method was found to improve the edge smoothness of squares through avoiding any unwanted resist exposure due to magnetic hysteresis especially when the beam is moved fast from shape to shape.

```
!EMC1          .........     Header for emc version 1.0
!RES           .........     Resolution keyword
1024           .........     Resolution value (128,256,512,1024....65536)
!SSQU          .........     Spiral square keyword
340            .........     centre x-coord
340            .........     centre y-coord
101            .........     Side width
!SCIR          .........     Spiral circle keyword
680            .........     centre x-coord
340            .........     centre y-coord
50             .........     Inner radius
120            .........     Outer radius
!RREC          .........     Raster rectangle keyword
0              .........     Scan direction
620            .........     First x-coord
620            .........     First y-coord
740            .........     Last x-coord
840            .........     Last y-coord
!SREC          .........     Raster rectangle keyword
1              .........     Scan direction
220            .........     First x-coord
740            .........     First y-coord
400            .........     Last x-coord
800            .........     Last y-coord
```

Fig 2.4 Example emc source file

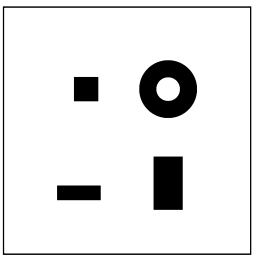

Fig 2.5 scan figure produced from example code

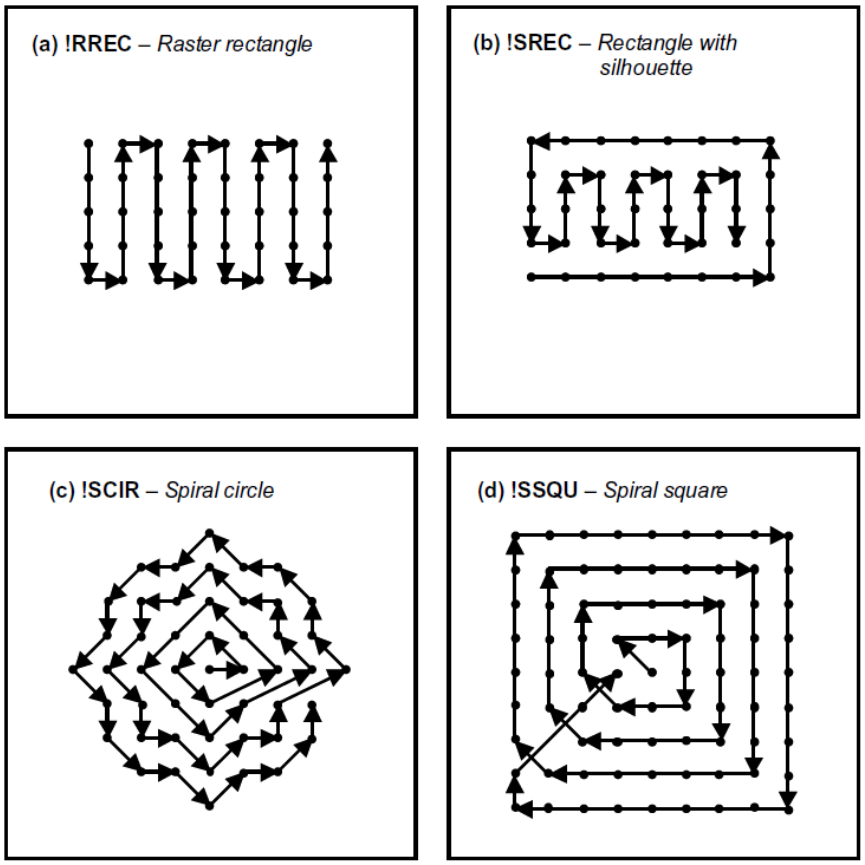

Fig 2.6 The point scan order for (a) a raster rectangle, (b) a raster rectangle with a silhouette, (c) a spiral circle and (d) a spiral square is shown for the four emc file entities supported by the current version of the Ionutils software [9]

2.2 PBW of micro-nanostructures

In this section, I will give the details of every step in fabricating the structures with PBW.

2.2.1 Sample preparation

All the work has been done in a class 1000 cleanroom.

I. Pre-treatment of silicon wafers

A silicon wafer has to be completely dry and clean so that photoresist can adhere well to the surface. In our experiment, the silicon wafers will be used in an electroplating machine, so a layer of Cr and Au is first coated onto the silicon wafer as seed layer for electroplating. Then, the wafer is baked at 200 ℃ for 30 min on a hot plate to dry completely.

II. Coating photoresist

Photoresist is coated onto the silicon wafer by spin coating process. In a spin coater, photoresist drops are dispensed in the center of the wafer and spread over the whole surface. The thickness is controlled by different spin speed, viscosity of the solvent and the molecular weight of the resist.

III. Pre-exposure bake

After coating photoresist, the wafer is baked to drive out all the solvent to become completely dry and solid. Different photoresists need different bake temperature and time, typically depending on the glass transition temperature and solid content of the resist respectively.

2.2.2 PBW

I. Proton beam focusing

The fabrication of nano-sized structures relies on focusing the proton beam to a sub-100 nm spot size. A free standing Ni resolution standard (Ni grid) and a channeltron electron multiplayer (CEM) are used to focus the proton beam. The Ni grid is the product of combined fabrication procedures employing; PBW, Deep UV lithography, Ni electroplating and metal etching [10, 11]. This enables us to get a 2 μm thick Ni fine gird on a coarser supporting grid. The fine grid has a side-wall vertically of 89.6 ◦ and an average side wall projection to the beam around 20 nm on either side. When protons hit the Ni

grid, secondary electrons will be induced. The CEM will detect secondary electrons when the proton beam is scanned across the Ni grid， typical images as shown in Fig. 2.7 are generated.

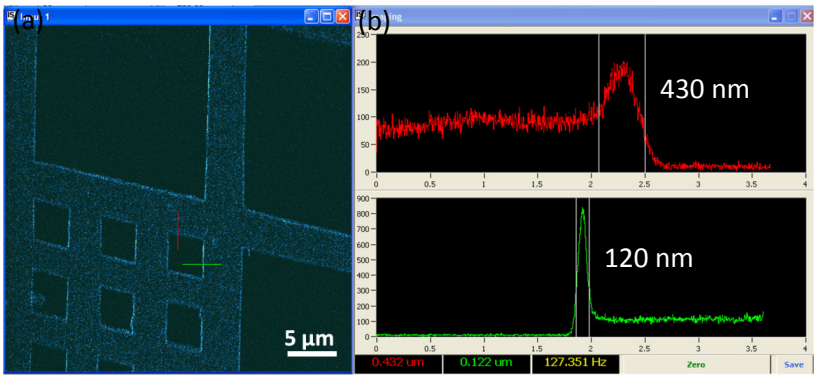

Fig. 2.7 (a)2 MeV Proton-induced secondary electron image from a free-standing Ni grid, (b) beam size measurement spectrum (Assume beam size is FWHM)

II. Focal plane adjustment

Fig. 2.8 shows a typical configuration of the Ni grid and sample in the sample holder.

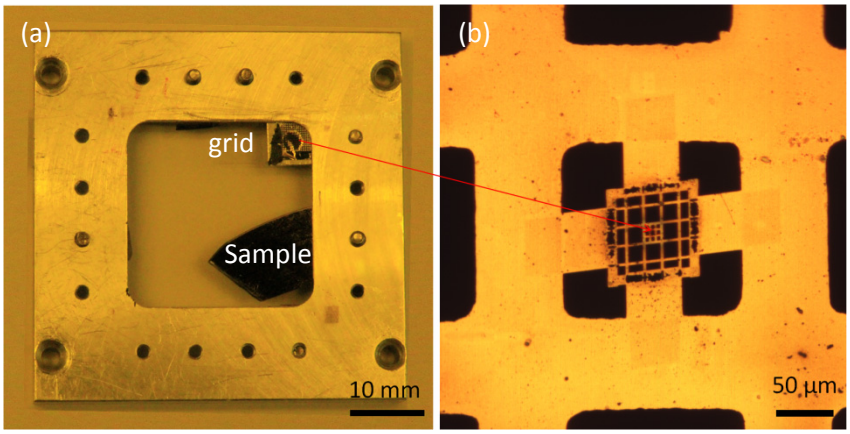

Fig. 2.8 (a) mounted Si wafer in sample holder. (b) An optical image of the Ni grid (the central part was fabricated by PBW, while the other parts were fabricated by UV lithography).

In the PBW focusing system, because of the short distance between the lenses and beam focus point, there is a relatively steep focusing angle, which can be controlled with the collimator slits just in front of the scanning system. The proton

beam is focused on the Ni grid. Since there is always a height difference between the Ni grid and the resist sample surface, this will result in increased beam spot size on the resist surface and therefore larger feature sizes.

In order to reduce this issue we measure the height difference between the Ni grid and the resist surface before we put the sample into the target chamber, using a high resolution optical microscope. In this way, we can determine the height difference with several micron precision. After focusing the proton beam on the Ni grid, the stage moves the resist surface into the focal plane of the proton beam. The accuracy of placing the sample in the focal plane is 10 μm. If the object slits' opening is 6 μm × 8 μm, and collimator slits' opening is 120 μm × 120 μm, the focused beam will increase by 21 nm × 7 nm.

III. Dose calculation

One important factor of fabricating micro- and nanostructures in photoresist is that an exact amount of energy needs to be deposited in the photoresist. Usually there are two ways to normalize the fluence. One way is to use Rutherford Backscattering (RBS). In this process, the beam dwells on a certain place for a while, until a certain number of backscattered particles are collected. However, this method is only suitable if large structures are to be written using a large beam current (several pA). When the proton beam is focused to sub-100 nm dimensions the beam current is typically very low. Usually the beam current to write nanostructures is less than 0.1 pA. To detect these small beam currents a silicon PIN photodiode can be used to directly count individual protons [12, 13]. A Hamamastu Si PIN photodiode (model S1223-01) is used to calibrate the beam current. The pin-diode consists of an

intrinsic Si layer contained between highly doped P and N type materials, it has high sensitivity, high reliability and high-speed response (fc= 20 MHz operated at a reverse bias of 20 V) [14]. However, the the pin-diode count rate should be kept low, due to data acquisition dead time issues.

IV. Beam scanning

Usually in PBW, there are two exposure strategies, one is magnetic or electrostatic beam scanning and the other is stage scanning. In the magnetic scanning system, the maximum area that can be exposed is 500 × 500 μm^2; if a structure is much larger, a combination of stage and beam scanning has to be used. Using this approach the system is capable of scanning over the sample surface with an area of 25 × 25 mm^2.

2.2.3 Development

After exposure, the sample is immersed in a container filled with developer, and then the residual developer is rinsed off using de-ionized water (DI). Next the resist structures obtained can be observed via optical or electron microscopy.

2.3 Resist material for PBW

Resist is a common name for all photo sensitive macromolecule polymers. It is usually a polymer consisting of a long molecular chain. There are many kinds of photoresists which have been tested with PBW [15]. Table 2.1 shows the current resists that can be patterned by PBW.

Table 2.1 current status and dose requirements in PBW

Resist	Type	Dose needed (nC/mm^2)	Energy of proton (MeV)	Smallest feature written	Aspect ratio
PMMA [15]	Positive	80-150	2	20-30 nm	100
SU-8 [16]	Negative	30	1	60 nm	166
HSQ [17]	Negative	30	2	19 nm	5.3
PMGI [15]	Positive	150	2	1.5 μm	8-9
WL-7154 [18]	Negative	4-8	1	260 nm	5
TiO_2 [19]	Negative	8000	2	5 μm	1.4
Si [20]	Negative	80,000	2	15 nm tip (implanted in channeling geometry)	15 nm at the tip, 600 nm at the bottom, sloped steeply at an angle of 85°
TADEP [21]	Negative	125-238	2	110 nm	18
ma-N 2401 [22]	Negative	40	1	60 nm	1.6
ma-N 2410 [18]	Negative	70-200	1	250 nm	2.4
AR-P 3250 [22]	Negative	30-50	1	330 nm	10.6
AR-P 3250: AR 300-12=1:3 [22]	Negative	50	1	120 nm	2.3
KMPR [23]	Negative	140	2	1 μm	10
ma-P 1275 HV [24]	Negative	20	1	10 μm	0.17
Diaplate [25]	Negative	10	2.7	10 μm	7
PADC (CR-39) [26]	Positive	600	2	5 μm	0.0048
Forturan [27]	Positive	1	2	3 μm	13.3
ma-N 440 [28]	Negative	200	2.25	400 nm	*
GaAs [29]	Negative	100,000	2	12 μm	1.4

*Data not given

In this section we will discuss several new kinds of photoresists that were tested during my work with PBW: ma-N series and ARP series. Because the tested negative resist before are not suitable for making Ni molds, new negative resist have to be investigated. PMMA was also used in this project since it is a very good positive resist which is also suitable for making Ni molds.

2.3.1 ma-N series

ma-N is a commercial e-beam resist developed by Microresist Technology in Germany [30]. The resists used here belong to ma-N 2400 series. ma-N 2400

is a negative tone photoresist series that can be used in both e-beam and deep UV lithography (wavelength: 248 nm.)It is well suited as an etch mask, exhibiting high dry and wet etch resistance. In addition, the thermal stability of the resist patterns is very good. 80 nm lines and spaces have been obtained at film thickness of 0.3 μm with ma-N 2400 at 20 keV acceleration voltage using electron beam lithography [31].

There are 4 kinds of photoresists with different viscosities in the ma-N 2400 series, which are ma-N 2401, ma-N 2403, ma-N 2405 and ma-N 2410 aiming at different resist thickness ranging from 100 nm up to 1.0 μm. In our experiment, we use ma-N 2401 and ma-N 2410 with PBW for thin and thick layer of photoresist. After PBW, the resists are developed in developer ma-D 525, and the final structures are obtained. Fig. 2.9 shows the experimental procedures of structuring ma-N resist with PBW:

a. A thin layer of Cr and Au was coated on a Si wafer as a seed layer for electroplating (more details will be given in the next chapter). Since Au has a poor adhesion with Si, usually a layer of Ti or Cr is first coated on Si to promote adhesion [32, 33, 34].
b. The wafer was cleaned by isopropanol (IPA) and rinsed in DI water, followed bake at 200 ℃ for 30 mins to remove all the water and impurities. Then ma-N resist was spin coated onto the Si wafer. For ma-N 2410, it was spin coated at 3000 rpm for 30 s followed by a prebake at 90 ℃ for 150 s. The thickness of ma-N 2410 was about 1.0 μm as observed through cross section SEM analysis. For ma-N 2401, it was spin coated at 3000 rpm for 30s. Then, the sample was prebaked at 90 ℃ for 60s. This gave a layer of 100 nm thick ma-N 2401.

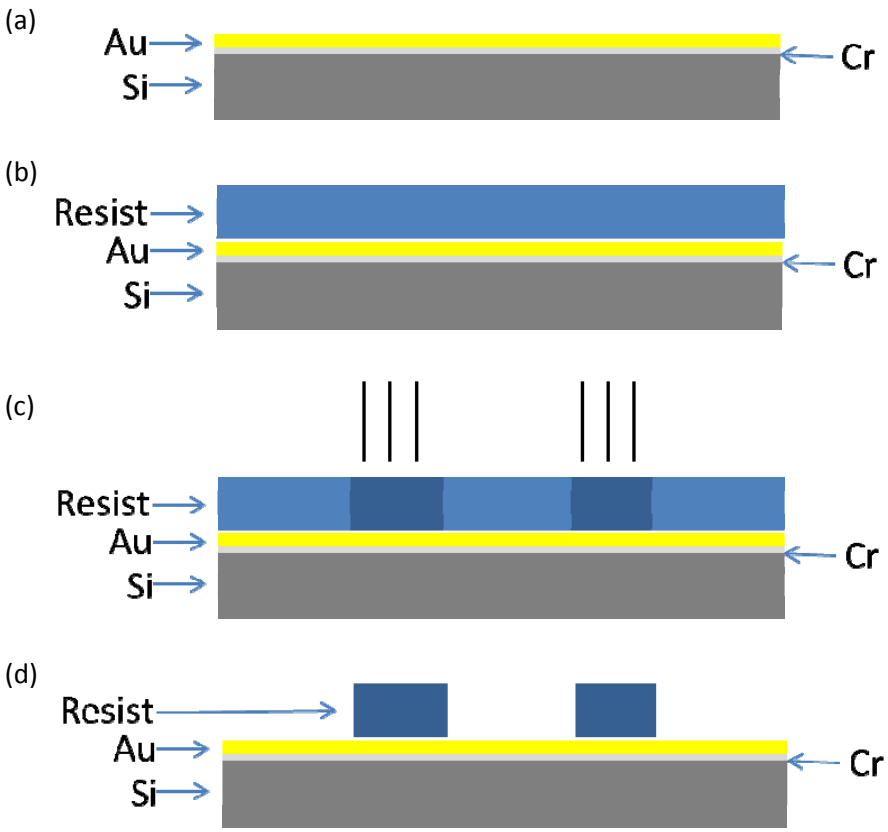

Fig. 2.9 Experimental procedure of PBW for micro- and nanostructures in ma-N (a) Cr and Au sputtering, (b) spin coat resist, (c) PBW, (d) development

c. PBW was performed with a 1 MeV proton beam which crosslinks the photoresist.

d. The sample was put into its recommended developer ma-D 525 to remove the resist which is not exposed with proton. Finally the sample was rinsed in DI water and air dried, this left the PBW structures in the resist.

ma-N 2410

ma-N series resist is relatively new resist to PBW. A dose test needs to be first accomplished. Fig. 2.10 shows the dose test for ma-N 2410 using PBW.

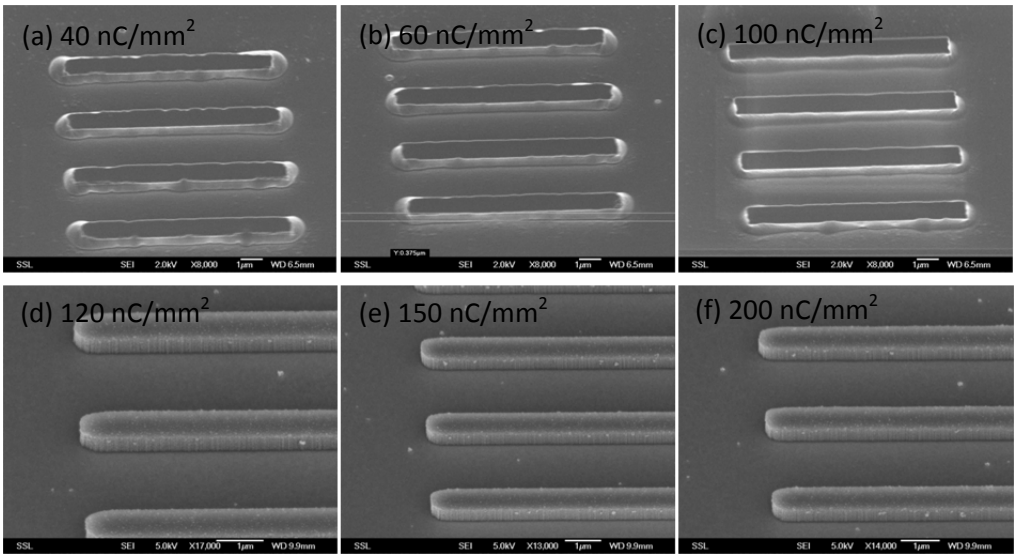

Fig. 2.10 Dose calibration using 1 MeV proton beam (a---f) the dose of proton is 40 nC/mm^2, 60nC/mm^2, 100nC/mm^2, 120nC/mm^2, 150nC/mm^2, 200nC/mm^2.

All the structures are fabricated by 1 MeV proton beam focused down to 100 nm × 150 nm in X and Y direction respectively. After exposure, all the structures are developed in ma-D 525 for 130 s and rinsed in DI water for 30 s. For structures a, b and c, the structures featuring 1 μm height and 1 μm width become better defined by increasing the dose from 40 nC/mm^2, 60 nC/mm^2 to 100 nC/mm^2. For structures d, e and f, there is no obvious difference using a proton dose of 120 nC/mm^2, 150 nC/mm^2 or 200 nC/mm^2. The optimized dose for ma-N 2410 is around 120 nC/mm^2, this is applicable for 1 micron but needs to be optimized for different thickness.

Fig. 2.11 shows 250 nm wide lines in 600 nm thick ma-N 2410, which is about a factor of 2 smaller than reported earlier [28]. In this experiment, ma-N 2410 was spin coated at 8000 rpm for 30 s followed by a pre-bake at 95 ℃ for 100 s. A 1 MeV proton beam was focused down to 100 nm × 120 nm to expose 10

μm long lines at a dose of 120 nC/mm^2. Then the sample was developed in ma-D 525 for 130 s and rinsed in DI water for 30 s and air dried. As can be seen from the figure, the structures feature vertical and smooth sidewalls. Pillars whose diameter was 330 nm in 600 nm thick ma-N 2410 were also fabricated under the same conditions.

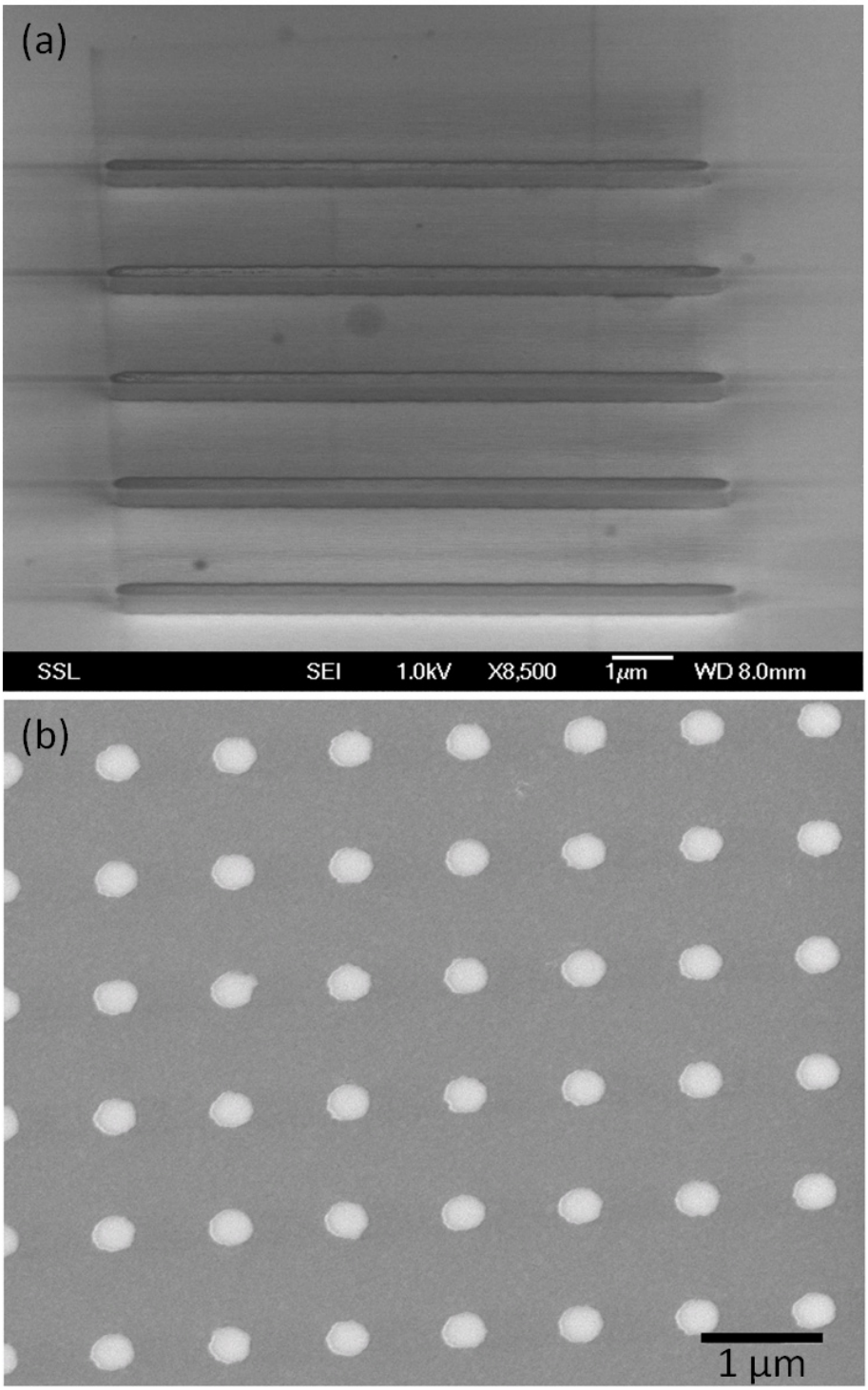

Fig. 2.11 (a)250 nm wide lines, (b) 330 nm diameter pillar in a 600 nm thick ma-N 2410 resist layer written with 1 MeV proton beam

ma-N 2401

ma-N 2401 is designed to achieve film thicknesses down to 100 nm. Figure 2.12 shows the dose test for ma-N 2401. The development procedure was optimized, the best results were obtained after 13 s in ma-D 525. The structures are 1 μm and 200 nm wide lines.

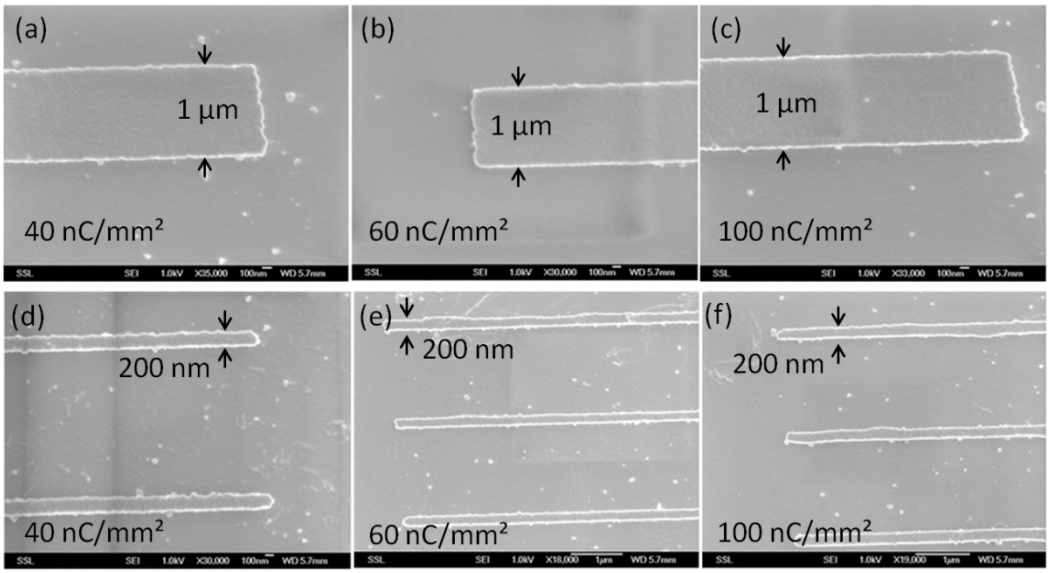

Fig. 2.12 Dose calibration using 1 MeV proton beam, the dose of proton is (a,d) 40nC/mm^2 (b,e) 60nC/mm^2 (c,f) 100nC/mm^2

ma-N 2401 was exposed by proton beam at a dose of 30 nC/mm^2, 40 nC/mm^2, 60 nC/mm^2, and 100 nC/mm^2. Proton beam of 30 nC/mm^2 is not enough to induce resist polymerization. After development, the structures at dose of 30 nC/mm^2 were all gone. In addition, for the dose higher than 40 nC/mm^2, the structures look identical. This means 40 nC/mm^2 is enough for ma-N 2401. However, the sidewall of the structures seems very rough; this is because ma-N 2401 is very sensitive to developer ma-D 525. The development time is very critical (different results were found if the resist was developed for 11s, 12s or 13s). Even for same development time, sometimes the results are different. Ma-N 2401 is not easy to control or to fabricate nice structures.

The best results are shown in Fig. 2.13. ma-N 2401 was exposed by 1 MeV proton beam (40 nC/mm^2) focused down to 60 nm × 100 nm in X and Y, and developed in ma-D 525 for 13 s. A 60 nm wide line has been fabricated in the 100 nm thick ma-N 2401, see Fig. 2.13a. Fig. 2.13b shows the sidewall of 100 nm wide line; the figure was taken at a tilt angle of 30°. The results show good resolution of ma-N 2401in PBW.

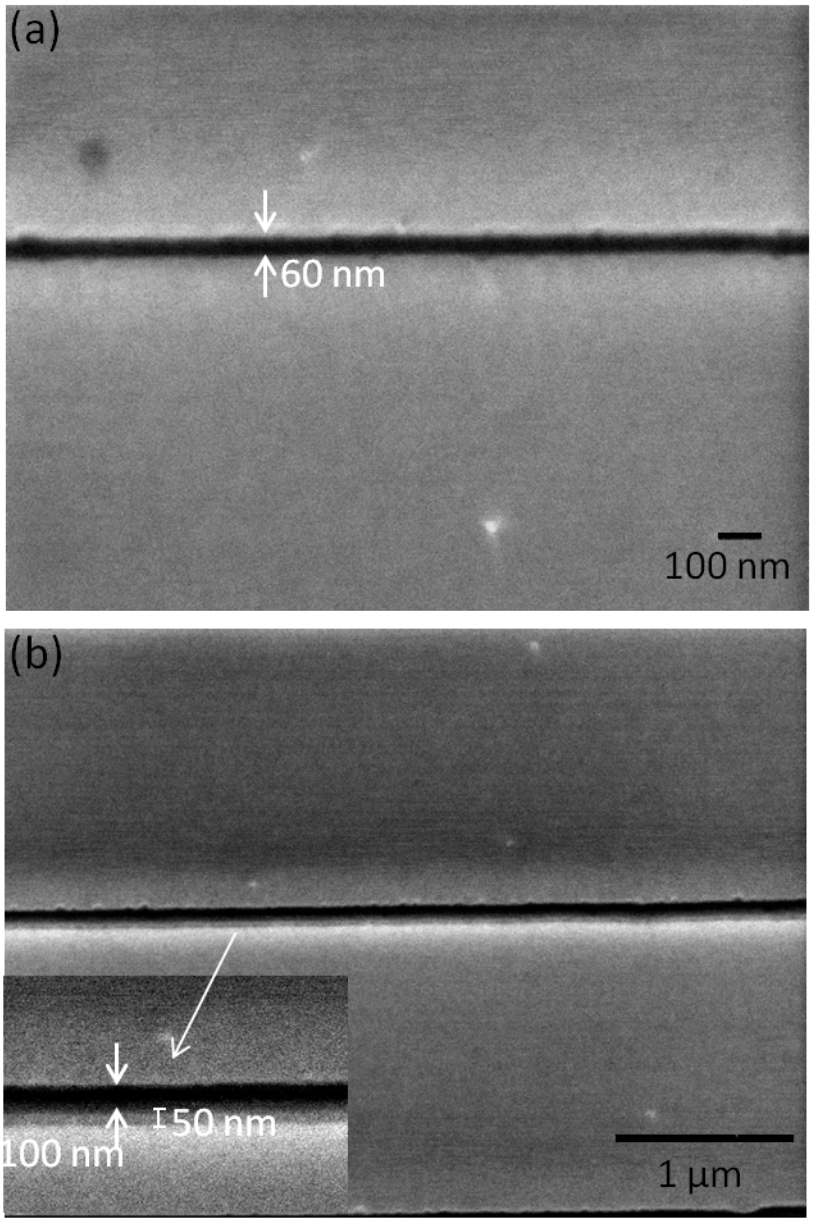

Fig. 2.13 (a) 60 nm line in 100 nm thick ma-N 2401 (b) side wall of 100 nm wide line in 100 nm thick ma-N 2401

2.3.2 PMMA series

Polymethyl Methacrylate (PMMA) is an optically transparent amorphous polymer derived from free radical polymerization of methylmethacrylate (MMA), whose molecular structure is shown in Fig. 2.14.

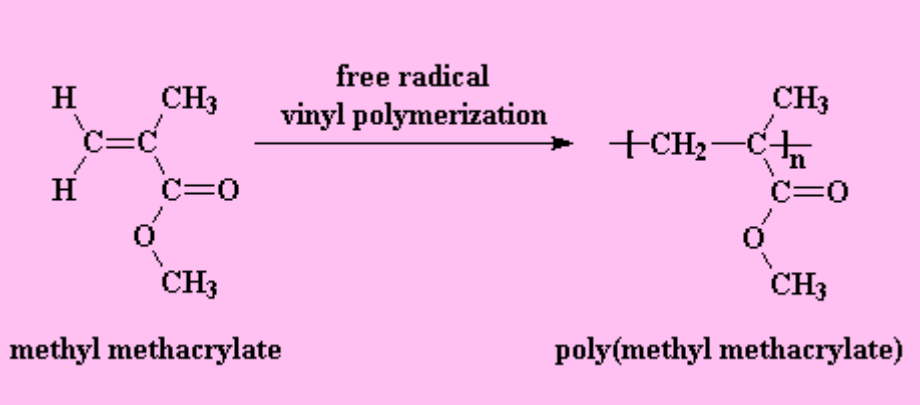

Fig. 2.14 PMMA structural construction

PMMA is normally white powder which can be dissolved in chlorobenzene or anisole to make up the PMMA resist, called PMMA C resist and PMMA A resist respectively. Usually PMMA resist can be purchased from MicroChem Inc. PMMA resist has been tested with protons in 1985 [35]. When exposed to an energetic proton beam, the resist experiences main-chain scission and the exposed region is dissolved away as shown in Fig. 2.15. However, experiments have shown that PMMA exposed at high doses in PBW presents negative tone performance. This part is not studied in this project.

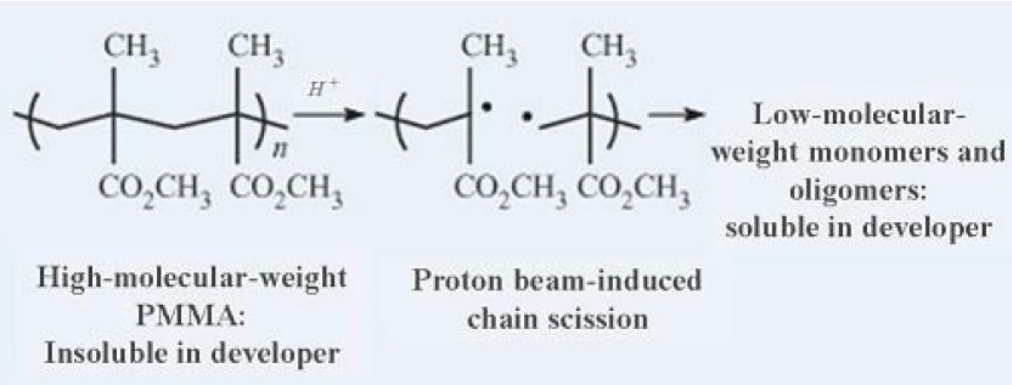

Fig. 2.15 Mechanism of radiation-induced chain scission in PMMA

In our experiment, we usually use PMMA A resist. There are many kinds of different PMMA A resists classified by their molecular weight (MW) and the concentration of the PMMA solids in the solvent. For example, 495 PMMA A11 means the MW of PMMA powder is 495000, and the concentration is 11% by weight in anisole. Basically, different molecular weight of solid content gives different thickness after spin coating. With larger MW and higher concentration, PMMA gives a higher thickness at a certain spin coating speed. The developer we used is isopropanol (IPA) mixed with DI water (IPA: DI water = 7:3) [36]. Compared with the traditional GG PMMA developer, which contains 60% diethylene glycol monobutyl ether, 20% morpholine, 5% ethanolamine and 15% water, IPA is much less viscous and is therefore more suitable to develop out high aspect ratio nano-structures [16].There are also some groups using IPA mixed with MIBK. However, water mixed with IPA has superior lithographic performance due to the high sensitivity and contrast of water/ IPA compared to standard MIBK/ IPA developer [36].

The experimental procedures are shown in Fig. 2.16.

a. Au and Cr coating.
b. 950 PMMA A4 resist is spincoated at 4000 rpm for 30 s on the Si wafer and baked at 180 ℃ for 90 s.
c. A fine focused proton beam is applied to pattern the resist.
d. The sample is developed in IPA: Di water= 7:3 and rinsed in DI water.

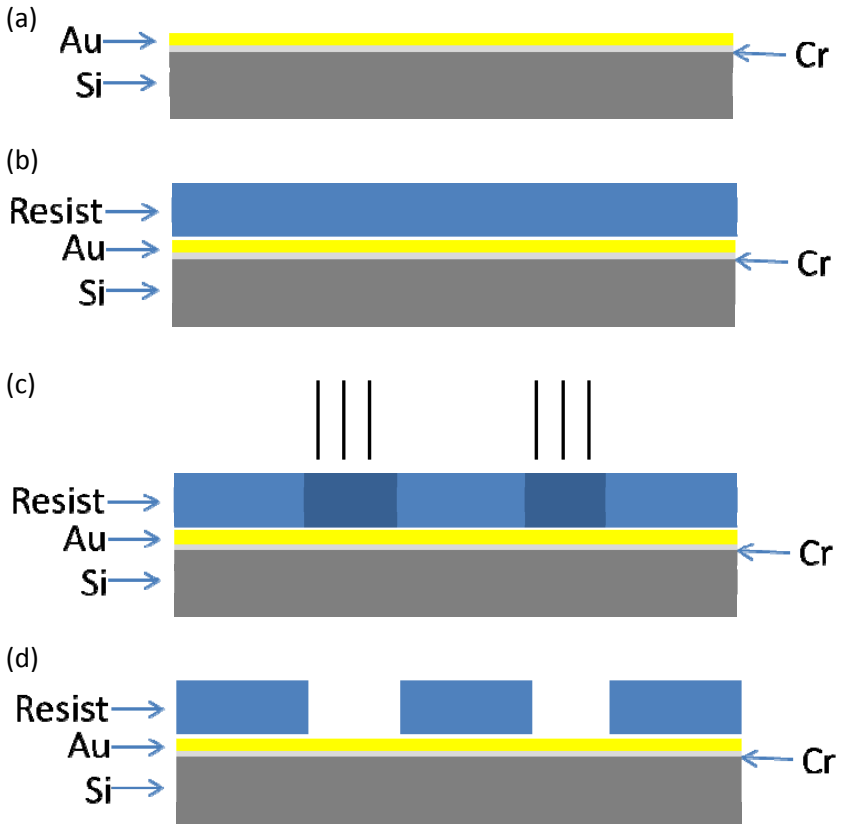

Fig. 2.16 Experimental procedure of PBW for micro- and nanostructures in PMMA (a) Cr and Au sputtering, (b) spin coat resist, (c) PBW, (d) development

Fig. 2.17 shows some PMMA channels with 200 nm thickness written using 1 MeV proton beam with a dose of 150 nC/mm^2. The proton beam is focused down to 100 nm × 150 nm in X and Y direction, respectively.

The width of the PMMA channels is about 100 nm. The distance between the channels can also be well controlled to a very small width. As shown in Fig. 2.17 I and (d), the smallest distance can reach about 50 nm. PMMA is a very good positive resist with high resolution and smooth side walls. In the next chapter, I will introduce Ni electroplating combined with proton beam written PMMA.

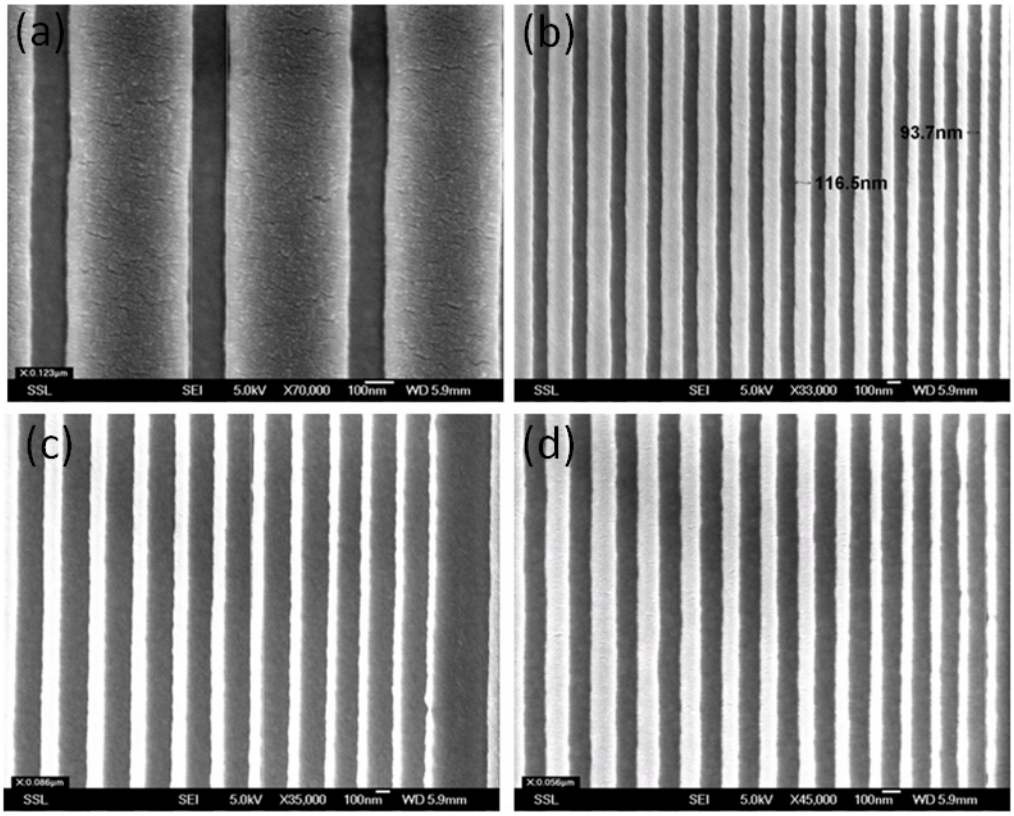

Fig 2.17 SEM image of proton beam written PMMA with a dose of 150 nC/mm^2

2.3.3 AR-P series

AR-P 3250

AR-P is a relatively high sensitive UV (365 nm) photoresist [37]. AR-P 3250 (ALLRESIST GmbH) is an interesting photoresist because it shows positive resist behavior under UV irradiation, i.e., the molecular chains are scissioned [38]. Under proton exposure the molecular chains cross link, i.e., it shows negative resist behavior. Therefore before development, the photoresist should further be exposed to UV. The photoresist that is exposed to UV becomes

soluble to the photoresist developer. The resist that has only been exposed by UV can be easily removed with the developer. However, in areas exposed by proton beam and UV, the UV irradiation can break the molecular chains that have been crosslinked by the proton exposure. There is a delicate balance between the UV and proton exposure. It requires optimization of UV as well as proton dose. The experimental procedure is shown in Fig. 2.18.

a. Au and Cr coating
b. ARP-3250 is spin coated on the Si wafer.
c. A fine focused proton beam is applied to pattern the resist.
d. A flood UV exposure on the whole surface of the sample.
e. The sample is developed in AR-300-26: DI water= 1: 1, rinsed with DI water and air dried.

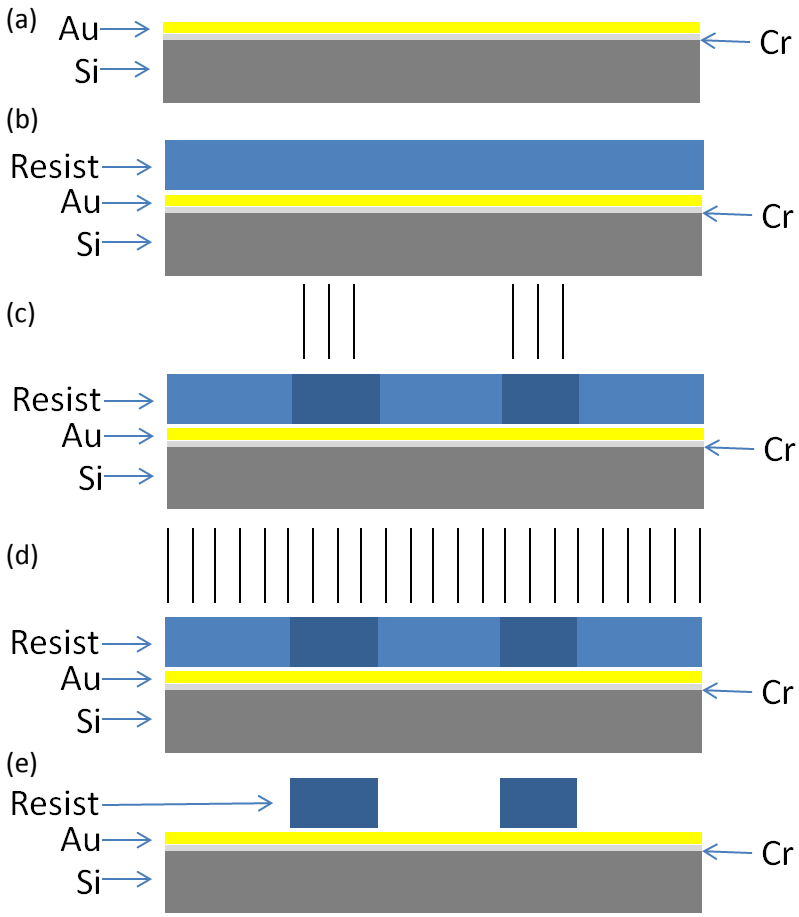

Fig 2.18 Experimental procedures for micro- and nanostructures using PBW and UV exposure (a) Cr and Au sputtering, (b) spincoat resist, (c) PBW, (c) UV exposure, (e)development

To optimize the exposure dose of the proton beam and UV three samples were prepared. All samples were coated with a 4 μm thick layer of ARP-3250 spin coated at 6000 rpm for 30 s. The 1 MeV proton beam was focused down to 100 nm × 150 nm in X and Y to pattern some grids in the resist with a dose of 20 nC/mm^2, 30 nC/mm^2 and 50 nC/mm^2. Then the samples were exposed with UV (365 nm using a 100 W lamp) for 5 min (Sample 1), 7 min (Sample 2) and 10 min (Sample 3) varying different exposure dose. The designed width of the structure is 5 μm, 3μm, 2μm, 800 nm, 500 nm and 340 nm from left to right as shown in Fig. 2.19.

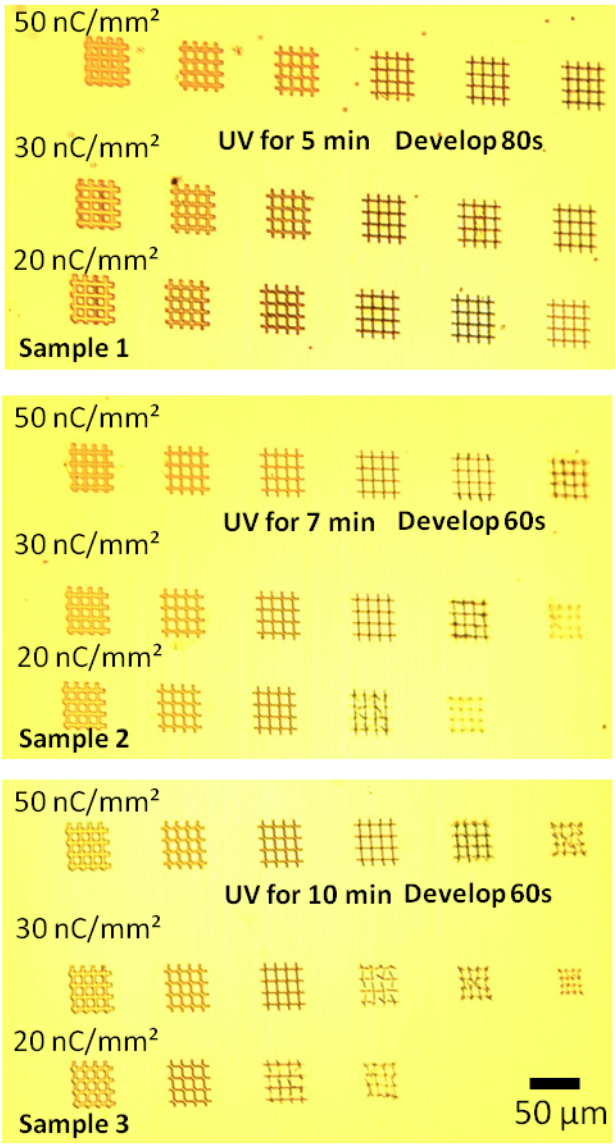

Fig 2.19 optical image of ARP-3250 grids (exposed with 1 MeV proton)(three samples)

Sample 1 was first developed in AR-300-26: DI water =1: 1 for 60 s, it is noticed there was still some resist not removed on the surface of the sample. Then we developed the sample for another 20 s. As a result, the total developed time for sample 1 was 80 s. Sample 2 and sample 3 were developed for 60 s.

As can be seen from Fig. 2.19, the 20 nC/mm^2 proton exposed structures are very sensitive to UV exposure. Longer UV exposure time can counteract the cross linking by the proton irradiation, as a result the parts exposed by proton

will become soft and not hard enough to remain standing. However, if the UV exposure dose is low, the resist cannot be completely developed.

As can be seen from Fig. 2.20, the structure was exposed with UV for 5 min (365 nm 100 W lamp), and developed in AR-300-26: DI water=1: 1 for 80 s. The designed width is 800 nm with a height of 4 μm. However, the height of the structures only about 1 μm, and in the center of the grids some resist is developed because the development time is too long and the UV exposure dose is not enough respectively.

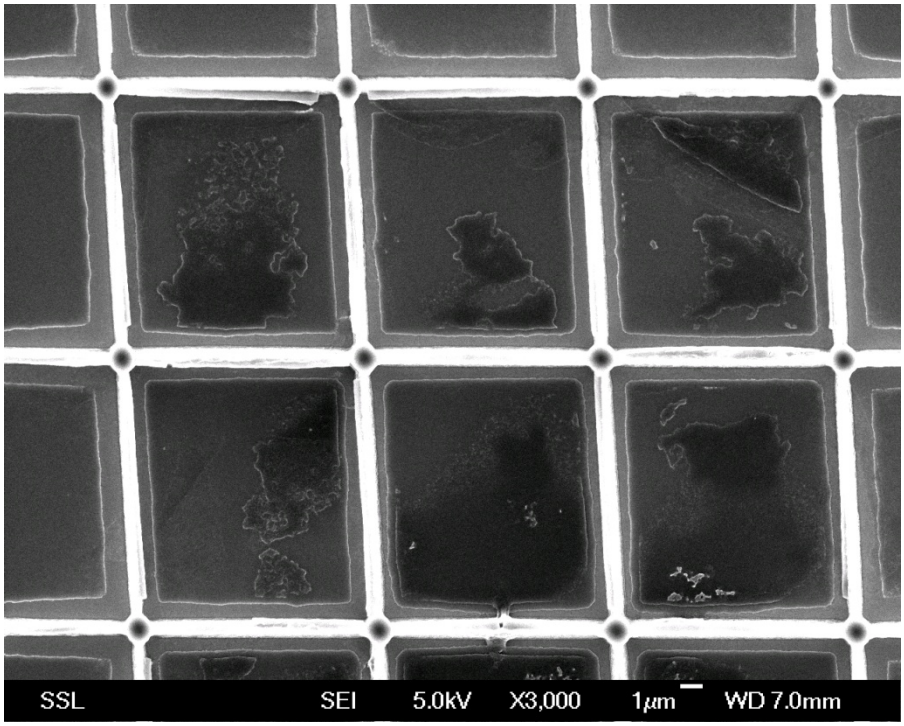

Fig 2.20 Sample 1 proton dose 50 nC/mm^2 exposed with UV (365 nm using a 100W lamp) for 5 min and developed for 80 s.

Longer UV exposure time can ensure proper resist development and at the same time reduces the development time which protects the proton beam written structures. Fig. 2.21 shows structures which were exposed by UV (365 nm using a 100W lamp) for 7 min and developed in AR-300-26: DI water=1: 1 for 60 s. The structure features 800 nm wide and 4 μm tall grid bars with smooth and vertical side walls, free from unwanted resist.

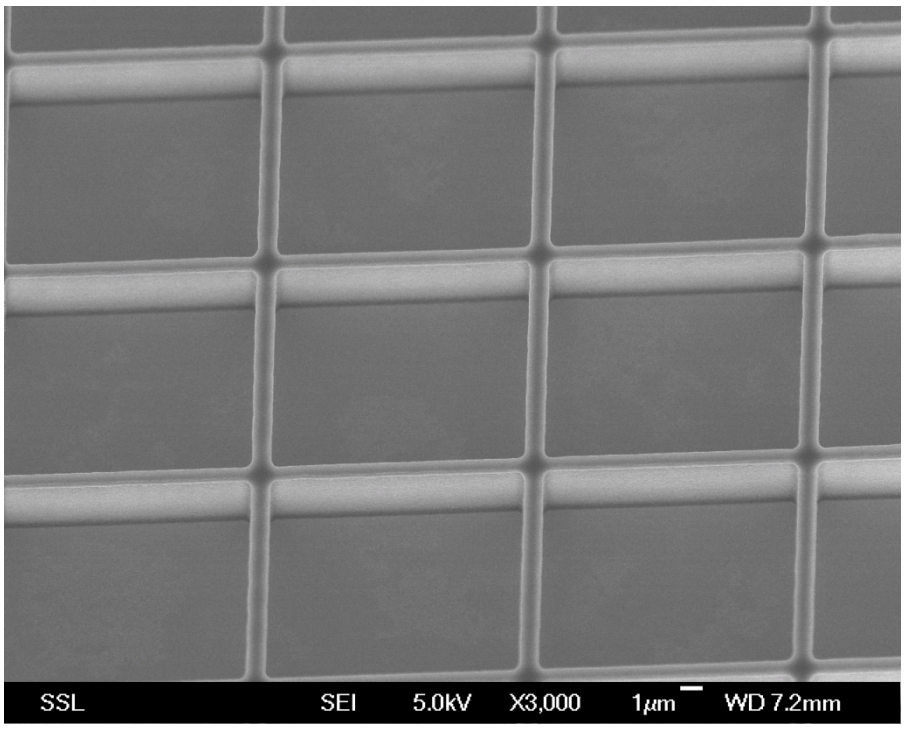

Fig 2.21 Sample 2 proton dose 50 nC/mm^2 exposed with UV (365 nm using a 100W lamp) for 7 min

For even longer UV exposure time, the grids fabricated by PBW are affected. A longer exposure of 10 min results in weakening of the resist and as shown in Fig. 2.22 prolonged UV exposure can counteract the cross linking by proton irradiation, as a result the parts exposed by protons will weaken.

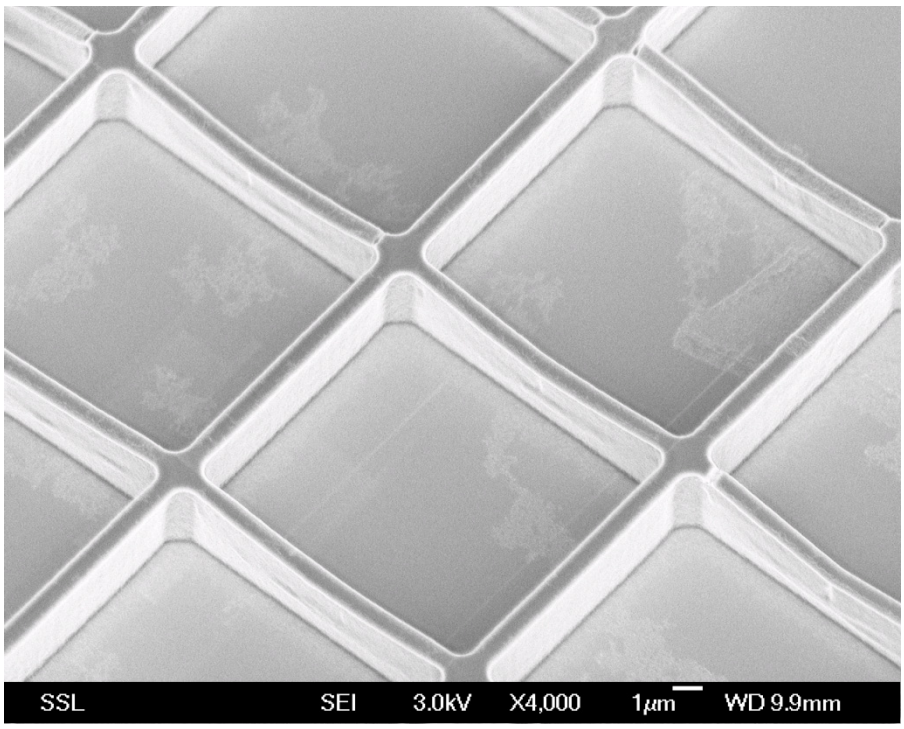

Fig 2.22 Sample 3 proton dose 50 nC/mm^2 exposed with UV (365 nm using a 100W lamp) for 10 min

The optimum UV exposure is at 7 min for a proton exposure of 50 nC/mm^2. Fig. 2.23 shows the normalized contrast curve (height of the resist as a function of exposure dose) for AR-P 3250 exposed to 1 MeV protons followed by UV exposure and chemical development. The contrast curve was measured with the structures at a width of 500 nm. Here the contrast is defined as $\gamma = 1/[\log(Df) - \log(Di)]$ where Df is the dose at which the resist is fully insoluble and Di the dose where the resist becomes insoluble in the developer. The measured contrast value is $\gamma = 3.5 \pm 0.5$ which is higher than previously reported [38]. This is due to different sizes of the structures. The contrast reported earlier was measured using large structures (of 10x10 μm^2), which are much more porous than the 500 nm structures used here. A relatively low proton dose is enough for large porous structures, however, a higher dose is needed to support high aspect ratio nano-structures.

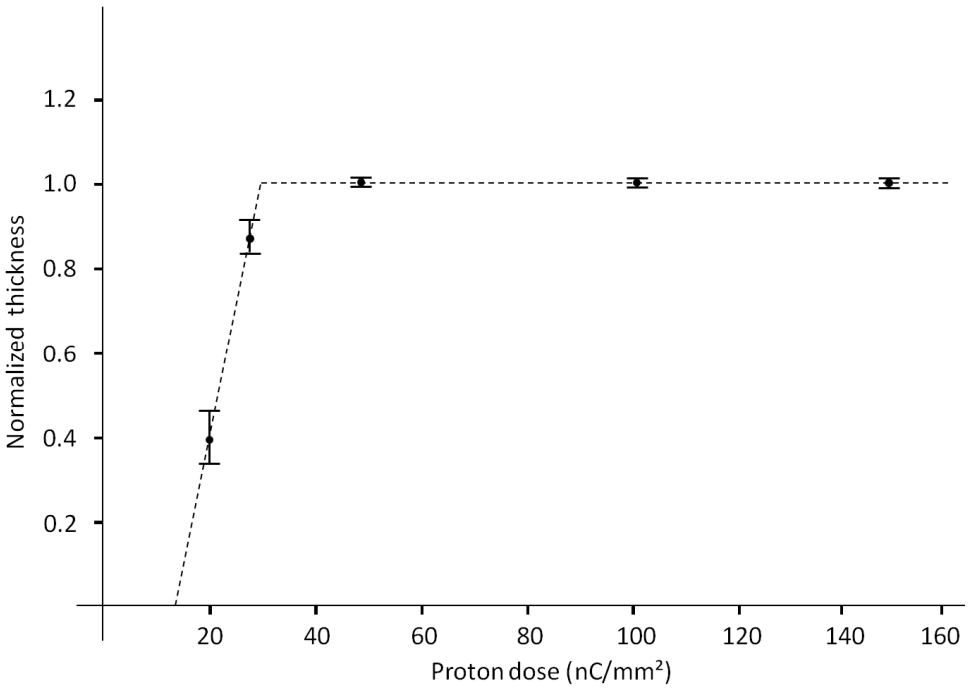

Fig. 2.23 Contrast curve of AR-P 3250, obtained for 500 nm wide structures in a 4 μm coated resist layer using 1 MeV protons, 7 min UV and 60 s development

Fig. 2.24 (a) shows a SEM photograph of the grid featuring lines down to about 500 nm in width, in 4 μm thick AR-P 3250, written with a proton dose of 50 nC/mm^2 and UV exposure for 7 min. The width of the lines matches with the designed file. Fig. 2.24 (b) is a high magnification SEM photograph of the horizontal line marked in Fig. 2.24 (a).

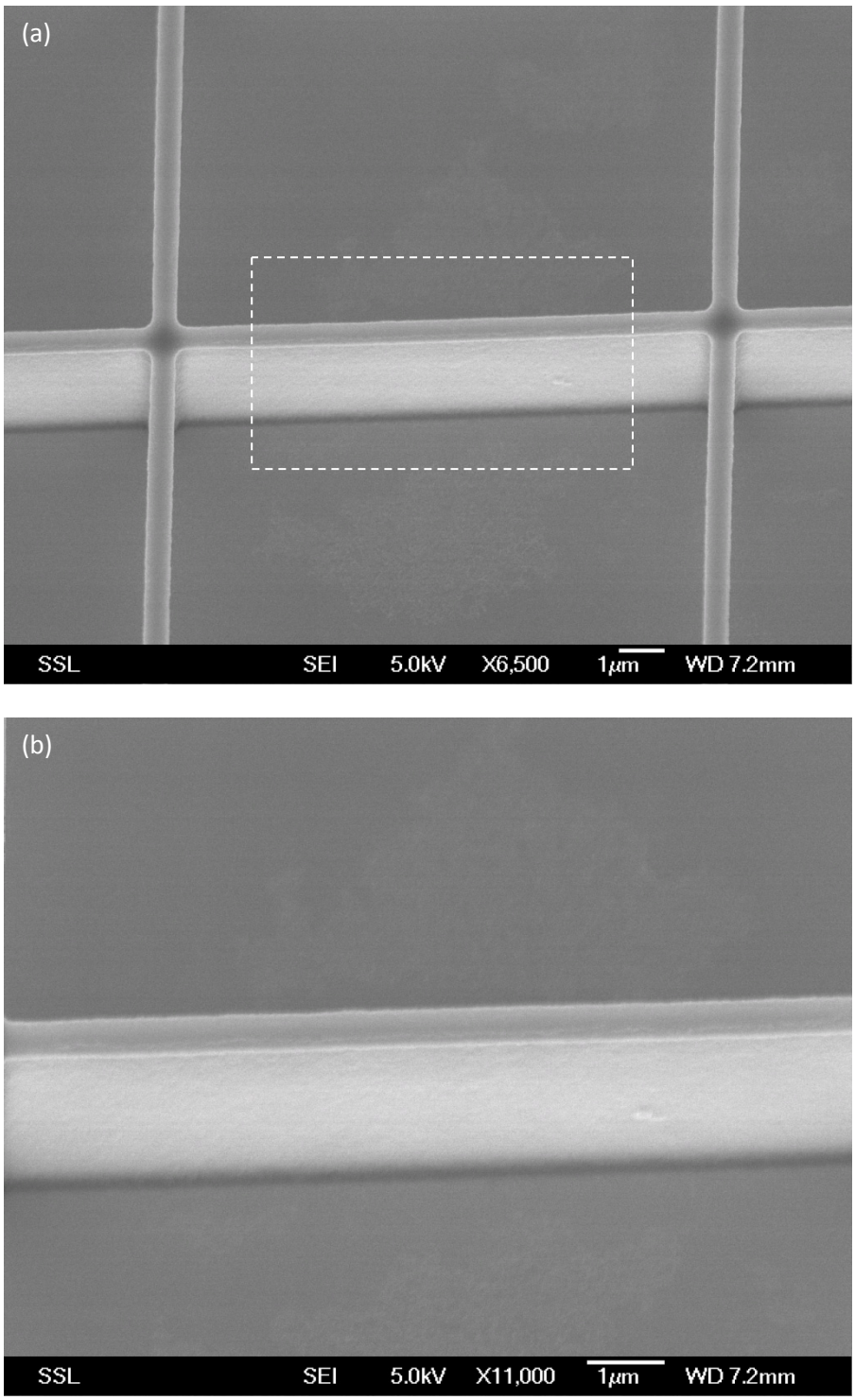

Fig. 2.24 (a) electron microscope image of AR-P 3250 grids in 4 μm thick layer featuring 500 nm wide lines (b) a high magnification SEM image of the 500 nm wide line in 4 μm thick AR-P 3250

As can be seen from Fig. 2.24 (a) and (b), the structures are well defined with sidewalls of high smoothness and vertically. In fact, in the 4 μm thick AR-P 3250, structures down to 200 nm can be realized, however high aspect ratio (20) leads to resist collapse (Fig. 2.25). A thinner resist layer was spin coated at 8000 rpm for 30 s, yielding a layer of 3.5 μm. Fig. 2.26 shows the SEM image of 330 nm wide line in the resist. The aspect ratio of the structure is more than 10. The side wall is also smooth and vertical.

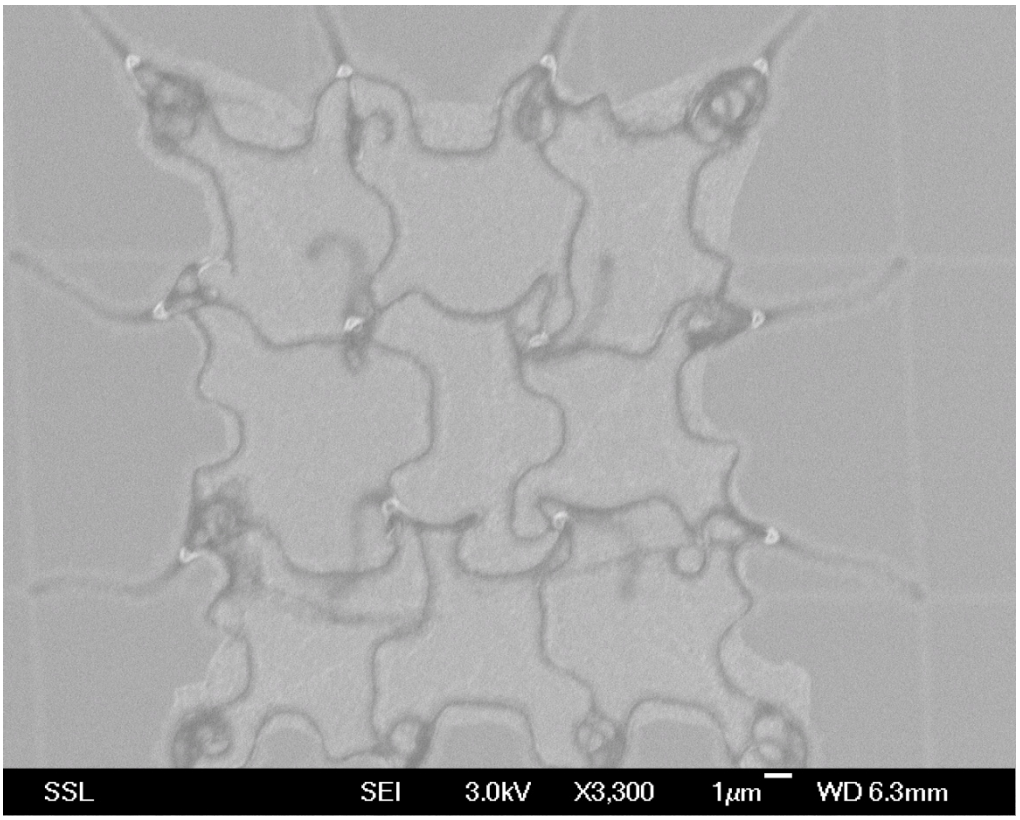

Fig.2.25 AR-P 3250 200 nm wide lines collapse

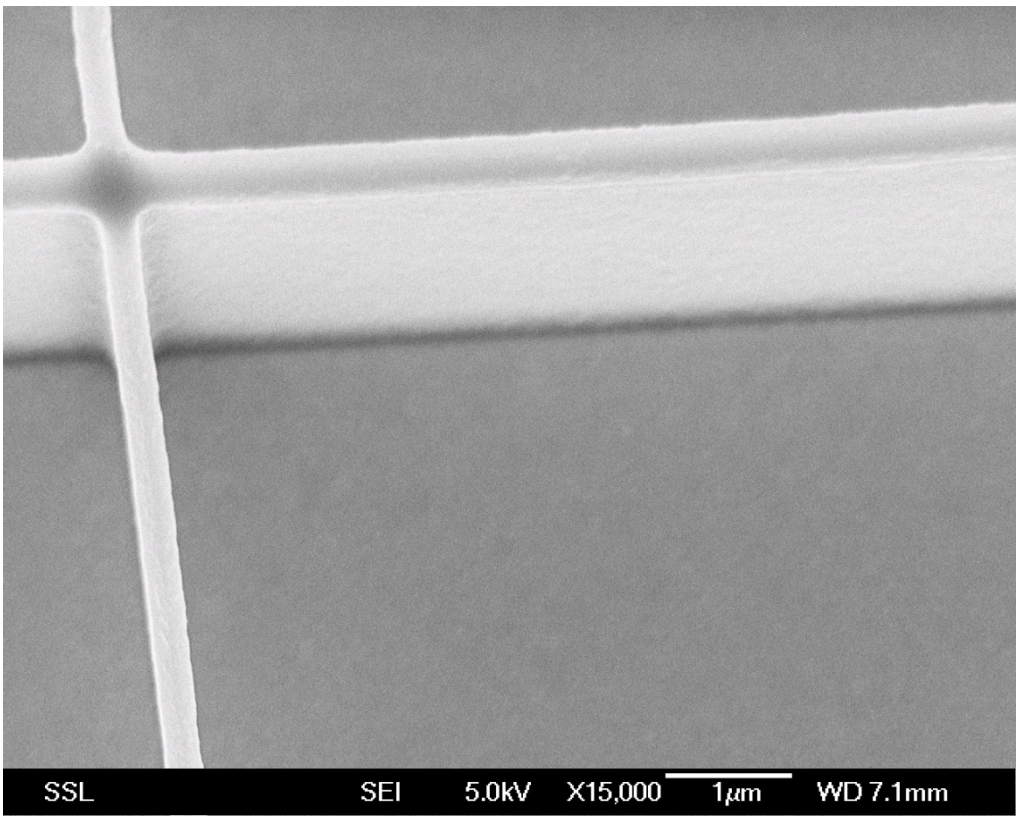

Fig. 2.26 330 nm wide line in 3.5 μm thick AR-P 3250

In order to characterize AR-P resist in more detail, the absorption of AR-P 3250 was measured as a function of wavelength using a DH-2000 BAL from 330 to 2000 nm and a spectrometer (QE 65000) to analyze the light intensity (λ>400 nm). AR-P 3250 was spin coated at 4000 rpm on a quartz substrate for 30 s, this yielded a layer of 5 μm thick. The resist was exposed by 2 MeV protons at using 30, 50, 100, 150 and 200 nC/mm^2 at an area of 500 μm^2. This corresponds to an equivalent dose of 18, 30, 60, 90 and 120 nC/mm^2 for a 1 MeV proton exposure, corrected for the increased stopping power [39]. The exposed area for each dose is around 500 μm × 500 μm. Next the absorption was measured for the bare and proton exposed AR-P 3250 resist. To establish the effect of the UV exposure on the proton exposed areas all the samples were exposed to 10 min UV (365 nm, 100 W Lamp) and the absorption of the AR-P 3250 was measured again.

The intensity of light, traveling in a medium, reduces according to the equation

$$I\,(z) = I_0\, e^{-\alpha z} \tag{2.1}$$

where α is the absorption coefficient and z is the distance along the propagation direction of light.

In our experiment, the first step was to measure the transmission of a pure quartz as a reference as shown in Fig. 2.27. Then the sample coated with resist was measured.

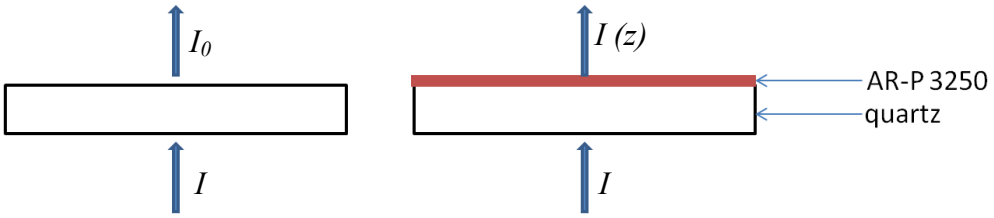

Fig. 2.27 Schematic of measurement method

The absorption coefficient

$$\alpha = ln\frac{I_0}{I\,(z)} / z \tag{2.2}$$

I_0 is the intensity transmitted through the quartz, $I\,(z)$ is the intensity transmitted through the quartz and resist, z is the thickness of the resist, which is 5 µm. Here we neglect internal reflections at the quartz resist interface.

Because of the limitation of our spectrometer, only the light with a wavelength between 400 to 1000 nm is analyzed. The intensity of light is very small, so it doesn't affect the resist.

Non exposed AR-P 3250 resist was measured as a reference and compared to resist exposed for 10 min UV (365 nm 100 W lamp). As can be seen in Fig. 2.28 the UV exposure greatly reduces the absorption in the resist as expected according to the data sheet from the supplier. Next the AR-P 3250 resist was exposed to 30, 50, 100, 150 and 200 nC/mm^2 using 2 MeV protons (30 nC/mm^2 resist was not measured because of low color contrast). As can be seen from the Fig. 2.28, resist exposed to protons has absorption between the absorption of plain resist and standard UV exposed resist, an increased proton

dose results in an increased absorption. Since unexposed AR-P resist has high absorption and is not affected by the development it is expected that proton exposed resist with a higher absorption is able to withstand the development procedure. This explains the fact that AR-P 3250 is a negative resist under proton exposure followed by UV exposure.

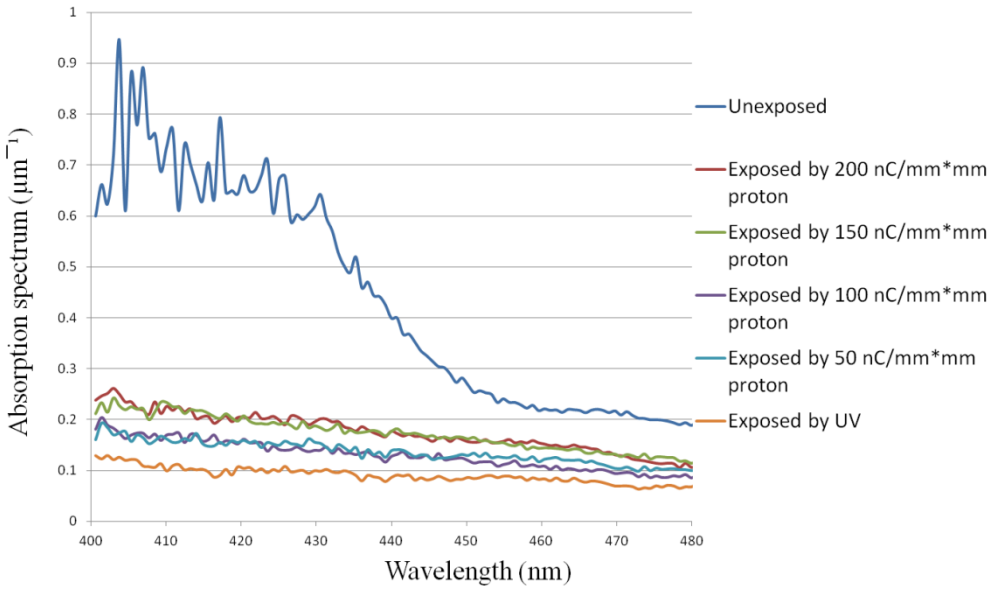

Fig. 2.28 Absorption spectrum of AR-P 3250

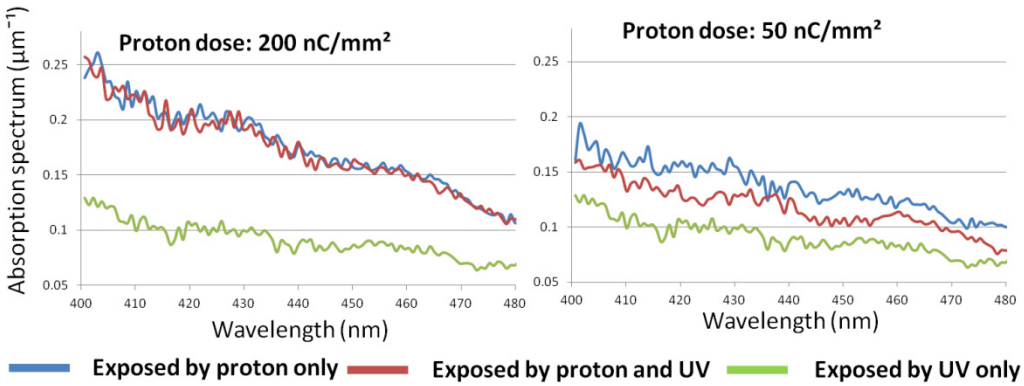

Fig. 2.29 Absorption spectrum of resist

Following step d in Fig. 2.18 all the proton exposed resist is exposed to UV for 10 min (365 nm 100 W lamp), followed by another absorption measurement. As can be seen from Fig. 2.29, after proton exposure at 50 nC/mm^2 followed by UV exposure the absorption is reduced and becomes

closer to the standard UV exposed resist. This observation implies that UV exposer changes the properties of proton exposed resist and brings its characteristics closer to standard UV exposed resist. The sample was developed in AR 300-26: DI water=1: 1.

Fig. 2.30 shows the height of the structure versus proton dose. As can be seen from the figure, as the proton dose increases, the height of structure also increases. This supports the effects shown in Fig. 2.20 that proton plus UV exposed resist can be easier removed for lower proton doses.

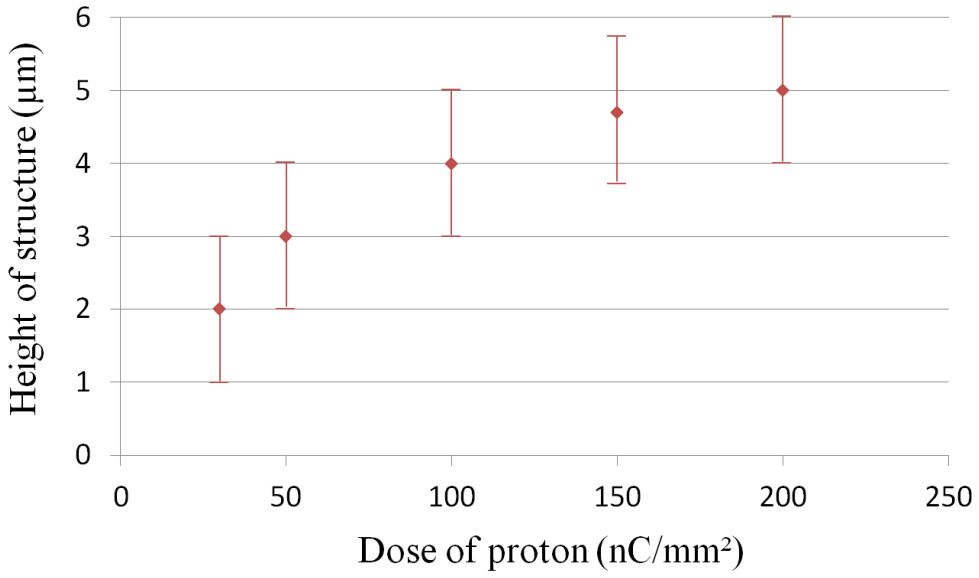

Fig. 2.30 Height of the structure for proton (1MeV) beam and 10 min UV exposure after development (size of the structures is 500 µm × 500 µm)

Mixture resist: AR-P 3250: AR 300-12= 1: 3 for thinner layer

AR-P 3250 is a resist for thick layer up to 3 or 4 µm. To evaluate the minimum feature size of AR-P resist a thinner resist is needed, AR 300-12 is a colourless mixture of organic solvents mainly intended to adjust the film thickness. Table 2.2 shows the properties of AR 300-12thinner.

Table 2.2 Parameters of thinner AR 300-12 [40]

Properties	AR 300-12	
Density (20 ℃)	g/cm^3	0.97
Refractive index (20 ℃)	%	1.402
Water content max.		0.1
Surface tension	mN/m	27
Non-volatile matter max.	ppm	50
Flash point	℃	42
Grade of filtration	μm	0.2

Here, we mixed 2 ml AR-P 3250 and 6 ml AR 300-12 together while stirring in a beaker. The mixture has the same property as AR-P 3250 resist. Under proton exposure the molecular chains cross link, i.e., it shows negative resist behavior. Before development, the photoresist should also be exposed to UV. The resist can be easily removed with the developer after UV exposure. The experimental procedures are the same as for AR-P 3250, see Fig. 2.30.

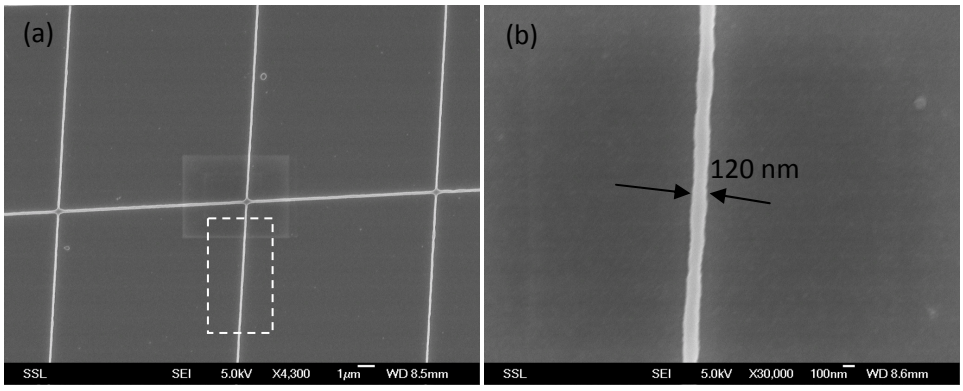

Fig.2.31 (a) electron microscope image of grids in 280 nm thick layer featuring 120 nm wide lines (b) a high magnification SEM image of the 120 nm wide line in 280 nm thick AR-P 3250：AR300-12= 1: 3

Au and Cr were first coated on Si wafer. Then the Si wafer was baked at 200 ℃ for 30 min to remove any moist. The resist was spin coated at 4000 rpm for 30 s, yielding a layer of 280 nm. The optimized dose of proton is also 50 nC/mm^2, and a 1 min UV (365 nm using a 100 W lamp) exposure. It takes 20 s to completely develop the area that has only been exposed by UV using

developer AR-300-26: DI water = 1:1. Fig. 2.31 shows the resist structures by PBW. As can be seen from the figures, the mixture resist has an even higher resolution than AR-P 3250.

2.4 Summary

I have studied several new photoresists including ma-N 2401, ma-N 2410, AR-P 3250 and diluted AR-P 3250 with AR 300-12. Table 2.3 shows the achieved results. As can be seen from this table, ma-N 2401 shows good resolution in PBW. In ma-N 2410, 250 nm wide lines and pillars with 330 nm diameter were fabricated in 600 nm thick resist. AR-P 3250 is a very interesting resist which is negative to PBW and positive to UV. Structures with aspect ratio up to 10 can be fabricated in 3.5 μm thick resist with vertical and smooth side walls. Because high aspect ratio structures easily collapse, diluted AR-P 3250 with AR 300-12 was used to achieve thin layer resist. A 120 nm wide line in 280 nm thick resist was fabricated in this mixed resist (AR-P 3250: AR 300-12=1:3). In the next chapter, Ni electroplating with these resist structures is discussed.

Table 2.3 Results for new resists for PBW presented in this thesis

Resist	Dose (nC/mm^2)	Energy of proton (MeV)	Minimum size (nm)	Aspect ratio
ma-N 2401	40	1	60*	1.67
ma-N 2410	250	1	250**	2.4
AR-P 3250	50	1	330**	10.6
Mixture (AR-P 3250: AR 300-12=1:3)	50	1	120**	2.3

* Limited by beam focus

** Limited by resist characteristic

References

[1] Mous D.J.W, Haitsma R.G.; Butz T., Flagmeyer R.H., Lehmann D., Vogt J, *The novel ultrastable HVEE 3.5 MV Singletron(R) accelerator for nanoprobe applications*, Nuclear Instruments and Methods in Physics Research Section B: Beam Interactions with Materials and Atoms, V 130, p 31-36, 1997

[2] J. A. van Kan, A. A. Bettiol, B. S. Wee, T. C. Sum, S. M. Tang, and F. Watt, *Proton beam micromaching: a new tool for precision three-dimensional microstructures*, Sens. Actuators A 92,p 370-374, 2001

[3] http://www.ciba.nus.edu.sg/index.html#

[4] Oxford Microbeams Ltd., Oxford Microbeams 89 Wroslyn Road Freeland Oxford OX7 2HL (0993) 881460. Nuclear Microprobe Quadrupole lens system.

[5] F. Watt, G.W. Grime, G.D. Blower, J. Takacs, *A Coupled Triplft Configuration of the Oxford Microprobe*, IEEE Transactions on Nuclear Science, V 28, 1981

[6] J.A. van kan, A.A. Bettiol, F. Watt, *Proton beam Nano-Machining: End station Design and Testing*, Nanostructuring Materials with Energetic Beams. Symposium, Mater. Res. Soc. Symposium Proceedings Vol.777, p 79-88, 2003

[7] J.A. van Kan, A.A. Bettiol, and F. Watt. *Proton beam writing of 3D nanostructures in Hydrogen SilsesQuioxane*, Nano Letters 6, 579-582, 2006

[8] A.A. Bettiol, C.N.B. Udalagama, J.A. van Kan, and F. Watt, *Ionscan: scanning and control software for proton beam writing*, Nuclear Instruments and Methods in Physics Research B, 231:400–406, 2005

[9] A.A. Bettiol, J.A. van Kan, T.C. Sum, F. Watt, *A LabVIEW-based scanning and control system for proton beam micromachining*, Nucl. Instr. and Meth. B 181 49, 2001

[10] J.A. van Kan, P.G. Shao, P. Molter, M. Saumer, A.A. Bettiol, T. Osipowicz, and F. Watt, *Fabrication of a free standing resolution*

standard for focusing MeV ion beams to sub 30 nm dimensions, Nuclear Instruments and Methods in Physics Research B, 231:170–175, 2005

[11] F. Zhang, J.A. van Kan, S.Y. Chiam, and F. Watt, *Fabrication of free standing resolution standards using proton beam writing*, Nuclear Instruments and Methods in Physics Research B, 260:474–478, 2007

[12] S. Ban, H. Hirayama, Y. Namito, S. Tanaka, H. Nakashima, Y. Nakane, and N. Nariyama, *Calibration of silicon pin photodiode for measuring intensity of 7-40 keV photons*, Journal of Nuclear Science and Technology, 31(2):163–168, 1994

[13] I. Britvitch, Y. Musienko, and D. Renker, *Investigation of a photon counting avalanche photodiode from hamamatsu photonics*, Nuclear Instruments and Methods in Physics Research A, 567:276–280, 2006

[14] Si pin photo-diode: S1223 series. http://sales.hamamatsu.com/assets/pdf/parts S/.

[15] J.A. van Kan, J.L. Sanchez, B. Xu, T. Osipowicz and F. Watt, *Resist materials for proton micromachining*, Nuclear Instruments and Methods B158 179-184, 1999

[16] J.A. van Kan, A.A. Bettiol, F. Watt, *Three dimensional nanolithography using proton beam writing*, Appl. Phys. Lett. 83 (8) 1629, 2003

[17] Y. Yao, P.S. Raman, J.A. van Kan, *Orthogonal and fine lithographic structures attained from the next generation proton beam writing facility*, 2013, Submitted to microsystem technologies

[18] J.A. van Kan, P. G. Shao, Y.H. Wang and P. Malar, *Proton beam writing a platform technology for high quality three dimensional metal mold fabrication for nanofluidic applications*, Microsystem Technologies 17:1519-1527, 2011

[19] J.A. van Kan, A.A. Bettiol, S.Y. Chiam, M.S.M. Saifullah, K.R.V. Subramanian, M.E. Welland, F. Watt, *New resists for proton beam writing*, Nucl. Instr. Meth. B 260 460-463, 2007

[20] E.J. Teo, M.H. Liu, M.B.H. Breese, E.P. Tavernier, A.A. Bettiol, D.J. Blackwood, F. Watt, *Fabrication of silicon microstructures using a high-energy ion beam*, Proc. SPIE 5347, Micromachining Technology for Micro-Optics and Nano-Optics II, 264, 2004

[21] E. Valamontes, M. Chatzichristidi, N. Tsikrikas, D. Goustouridis, I. Raptis, C. Potiriadis, J.A. van Kan, F. Watt, *Realization and simulation of high-aspect-ratio micro/nanostructures by proton beam writing*, Jpn. J. Appl. Phys., Vol. 47, No. 11, 2008

[22] Y.H. WANG, P. Malar, J. A. van Kan, *Resist evaluation for proton beam writing, Ni mold fabrication and nanoimprinting*, Submitted to microsystem technologies.

[23] M.D. Ynsa, P. Shao, S.R. Kulkarni, N.N. Liu, J.A. van Kan, *Exposure parameters in proton beam writing for KMPR and EPO Core negative tone photoresists*, Nuclear Inst. and Methods in Physics Research, B, V 269, p. 2409-2412, 2011

[24] Liu Nan Nan, Shao Peige, Shripad R. Kulkarni, Zhao Jianhong and Jeroen A van Kan, *Nickel Injection Mould Fabrication via Proton Beam Writing and UV Lithography*, Key Engineering Materials Vols. 447-448 pp 188-192, 2010

[25] Y. Gonin, F. Munnik, F. Benninger, F. Dias, S. Mikhaílov, *Comparison of a new photoresist (DiaPlate 133) with SU-8 using both x-ray and ion beam lithographies*, J. Vac. Sci. Technol. B 22 1982, 2004

[26] I. Rajta, E. Baradács, A.A. Bettiol, I. Csige, K. Tőkési, L. Budai, Á.Z. Kiss, *Optimization of particle fluence in micromachining of CR-39*, Nucl. Instr. Meth. B, 231384-388, 2005

[27] I. Rajta, M.I. Gomez, M.H. Abraham, Á.Z. Kiss, *Proton beam micromachining on PMMA, Foturan and CR-39 materials*, Nucl. Instr. Meth. B, 210 260-265, 2003

[28] F. Menzel, D. Spemann, S. Petriconi, J. Lenzner, T. Butz, *Proton beam writing of microstructures at the ion nanoprobe LIPSION*, Nucl. Instr. Meth. 260 419, 2007

[29] P. Mistry, M.I. Gomez, R.C. Smith, D. Thomson, G.W. Grime, R.P. Webb, R. Gwilliam, C. Jeynes, A. Cansell, M. Merchant, K.J. Kirkby, *Maskless proton beam writing in gallium arsenide*, Nucl. Instr. Meth. B, 260 437-441, 2007

[30] Microresist Technology GmbH, http://www.microresist.de

[31] Voigt A, Elsner H, Meyer H G, Gruetzner G, *Nanometer patterning using ma-N 2400 series DUV negative photoresist and electron beam lithography*, SPIE, V.3676, part 2, p.485, 1999

[32] J. Noetzel, T. Tønnesen, J. Binder, and G. Mader, *Quasianalog accelerometer using microswitch array*, Sensors and Actuators., A54:574–578, 1996.

[33] P. Rombach, H. Steiger, and W. Langheinrich, *Planar coils with ferromagnetic yoke for a micromachined torque sensor*, J. Micromech. and Microeng., 5:136–138, 1995

[34] J. Gergqvist and J. Gobet, *Capacitive microphone with a surface micromachined backplate using electroplating technology*, J. Microelectromechanical Systems., 3:69–75, 1994

[35] Ilesanmi Adesida, *Fine line lithography using ion beams*, Nucl Instrum Method B (Beam Interactions with Materials and Atoms), v B7-8, pt.2, p 923-8, 1985

[36] S. Yasin, D.G. Hasko, H. Ahmed, *Comparison of MIBK/IPA and water/IPA as PMMA developers for electron beam nanolithography*, Microelectron. Eng. 61–62 745-753, 2002

[37] Haller I, Hazakis M, Srinivasan R, *High resolution positive resists for electron beam exposure*, IBM J.Res.Develop., 12, p.251, 1986

[38] P. Malar, Zhao Jianhong, J.A. van Kan, *Fabrication of metallic molds for injection moulding applications by combining proton beam writing and UV lithography*, Applied Surface Science 258 (2012) 4191-4194

[39] J. F. Ziegler, *The stopping of energetic light ions in elemental mater*, J. Appl. Phys/Rev. Appl. Phys., 85, 1249-1272, 1999

[40] http://allresist.de/wMedia/pdf/wEnglish/produkte_photoresists/AR300_12.pdf

Chapter 3 Fabrication of Ni mold using proton beam writing and Ni electroplating

In this chapter, I will first introduce the technique of Ni electroplating as a method of fabricating a Ni mold, in the second half I will talk about the Ni mold fabrication process using proton beam writing (PBW). Electroplating has a really very long history. It was first invented by Italian chemist Luigi V. Brugnatelli in 1805. By 1876, the Norddeutsche Affinerie in Hamburg had already used modern electroplating plant starting its production [1]. Now electroplating is widely used in industry for coating metal objects with a thin layer of metal typically used as decoration or protection.

3.1 Ni electroplating

Electroplating is a process that uses direct electrical current to dissolve and move metal cations to an electrode to realize metal coating. It is primary used to change surface properties of objects, build up thickness or to form objects by electroforming. There are 3 parts in our electroplating cell which are electrolyte, a set of electrodes (anode and cathode), and an external power supply as shown in Fig. 3.1. The anode and cathode are both connected to the external power supply. The anode is connected to the positive pole, while the cathode is connected to the negative pole. When the power is on, the anode is oxidized to form cations with positive charge. The cations flow with the current and deposit on the cathode.

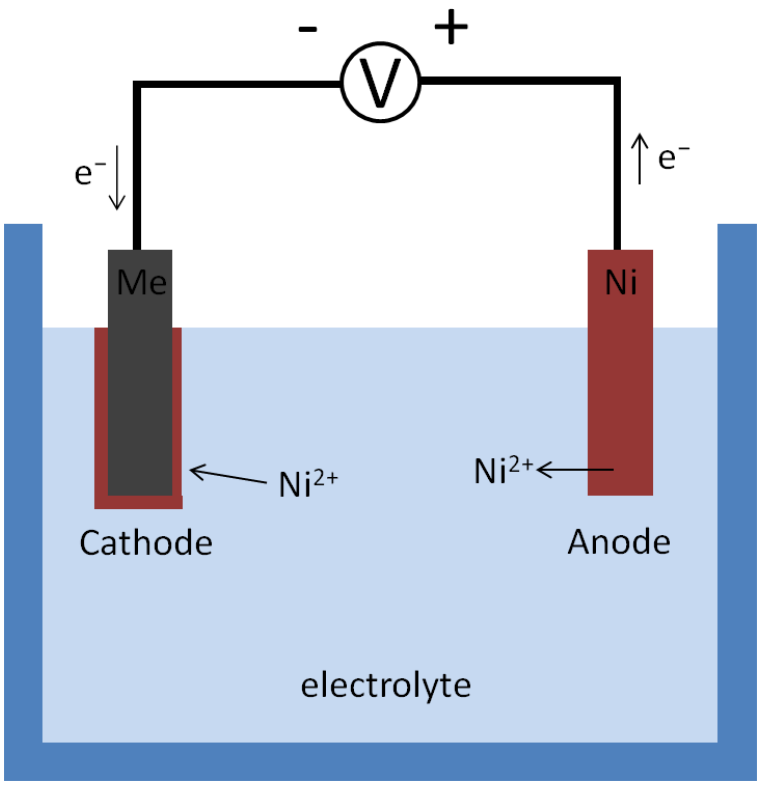

Fig. 3.1 Electroplate a metal (Me) with Ni in a Ni electrolyte bath

In this thesis I will only introduce Ni electroplating. The Ni anode is dissolved into the electrolyte.

$$Ni \rightarrow Ni^{2+} + 2e^{-} \tag{3.1}$$

When current flows, the positive ions react with two electrons ($2e^{-}$) and convert to metallic Ni at the cathode.

$$Ni^{2+} + 2e^{-} \rightarrow Ni \tag{3.2}$$

As can be seen from equations 3.1 and 3.2, the anode with metallic Ni is dissolved to form divalent, positively charged ions which enter the solution. The Ni ions discharged at the cathode are thus replenished by those formed at the anode.

However, the discharge of Ni ions is not the only reaction that occurs at the cathode; a small percentage of the current is consumed in hydrogen ions from water. This reduces the cathode efficiency for Ni deposition from 100% to 95 +/- 3% depending on the nature of the electrolyte. The discharged hydrogen atoms form bubbles of hydrogen at the cathode surface.

Hydrogen evolution at the cathode is accompanied by the production of hydroxide ions:

$$2H_2O + 2e^- \rightarrow 2OH^- + H^2 \qquad (3.3)$$

If the cathode efficiency is lower than the anode efficiency, the electrolyte becomes more alkaline (pH increases). If the pH of the solution is too high, hydroxyl ions may be discharged which hampers the dissolution of Ni, and oxygen will be formed, shown in equation 3.4.

$$2H_2O \rightarrow O_2 + 4H^+ + 4e^- \qquad (3.4)$$

Under those conditions, the Ni anode becomes passive and ceases to dissolve Ni. Activated Ni anode materials are available commercially that resist the onset of passivity and replenish the solution with Ni ions over a wide range of plating conditions.

Since Watts developed a new Ni electroplating solution in 1916, it has replaced all others in use up to that time [2]. This solution contains $NiSO_4 \cdot 7H_2O$; $NiCl_2 \cdot 6H_2O$ and H_3BO_3. It was found that this bath can be operated at elevated temperatures and is capable of being used with high current densities.

The amount of Ni dissolved at the anode and the amount deposited at the cathode are directly proportional to the product of the current and time and can be calculated from the following expression,

$$m = \frac{M}{nF} \times a \times I \times t \qquad (3.5)$$

where m is the mass of Ni deposited at the cathode (or dissolved at the anode) in grams; M is the atomic weight of Ni (58.69); n is the number of electrons in the electrochemical reaction (2); and F is Faraday's constant 26.799 ampere-hours; I is the current that flows through the electroplating cell; t is the time that the current flows in hour; and a is the current efficiency (CE).

Current efficiency is a very important parameter in electroplating. It is the ratio between the weight of Ni actually deposited at the cathode and the amount theoretically expected from Faraday's laws if there are no side reactions. In reality, there are always some other reactions. It is known that when two or more reactions occur simultaneously at an electrode, the total number of coulombs of electricity passed corresponds to the sum of the number of equivalents of each reaction. The current efficiency CE of the ith process, namely of any one of the simultaneous reactions, is defined as the number of coulombs required for that reaction Q_i, divided by the total number of coulombs passed Q_{total},

$$\text{CE}=\frac{Qi}{Q_{\text{total}}} \tag{3.6}$$

3.2 Ni electroplating system: Technotrans AG, RD. 50 plating system

Although Ni electroplating has a more than 100 years' history, it is a relatively new process in Microsystems. Our molds are fabricated using a Technotrans AG, RD.50 plating system as shown in Fig 3.2.

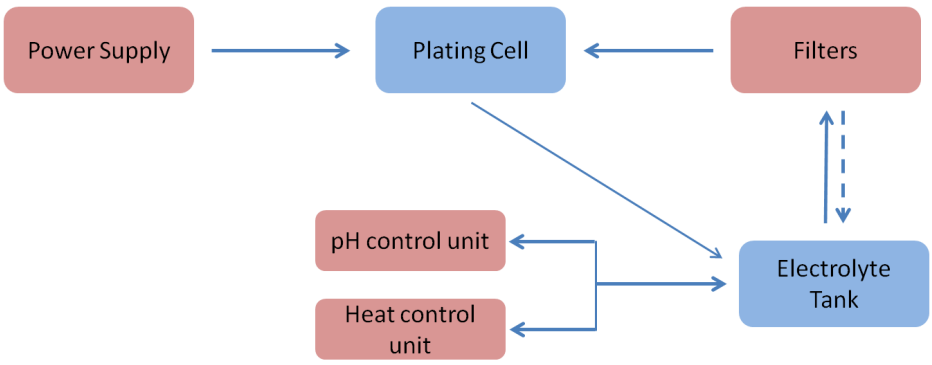

Fig. 3.2 System schematic for electroplating cell

In our electroplating machine, there are several factors influencing the plating process and the plated structures. The power supply should maintain stable plating current with minimum ripple during the plating process. The electrolyte is stored in a collection tank, heated by thermostat-controlled porcelain heaters, and continuously cycled through a 10 μm pre-filter and a 0.5 μm fine filter to clean and maintain a low particle concentration. With the aim of maintaining the concentration during the process of electroplating, pH value and temperature are constantly controlled and adjusted automatically by sensors attached to the electrolyte tank.

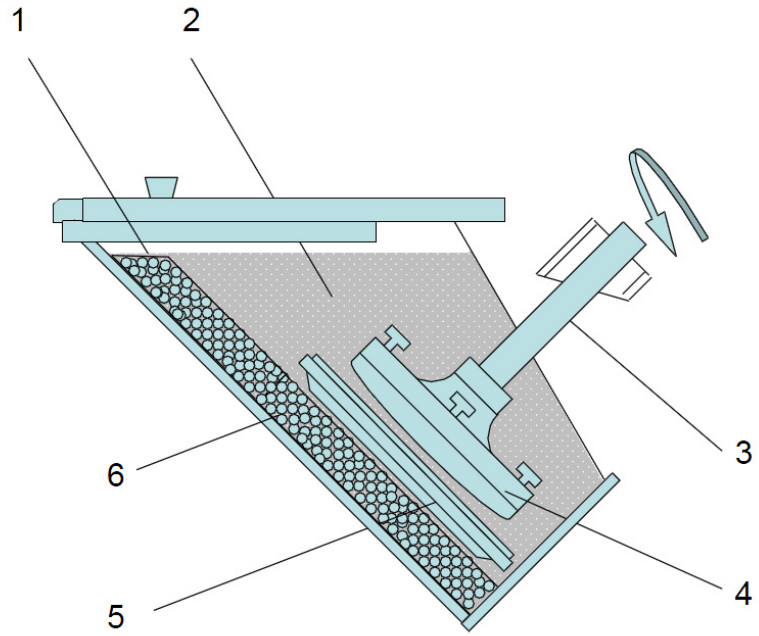

Fig. 3.3 Schematic of the RD.50 Electroplating Cell.1) Anode Basket 2) Electrolyte 3) Spindle Drive 4) Cathode plus Sample Holder 5) Tunnel Battle 6) Anode Material

In the electroplating cell, there are three main parts: 1）the anode basket 2) the electrolyte and 4）the Cathode as shown in Fig. 3.3. The samples are mounted on a titanium plate connected to a spindle drive. The electroplating bath consists of Ni sulfamate ($Ni(SO_3NH_2)_2$), Ni chloride ($NiCl_2 \cdot 6H_2O$), boric acid (H_3BO_3) and wetting agent shown in table 3.1.

Table 3.1 compositions for Ni electroplating solution

Composition	Density
Ni sulfamate $Ni(SO_3NH_2)_2$ (g/L)	370 ~ 390
Ni chloride $NiCl_2 \cdot 6H_2O$ (g/L)	10
Boric acid H_3BO_3 (g/L)	40 ~ 55
Wetting agent (mL/L)	0.05 ~ 0.10

Wetting agent is used in Ni baths to prevent bubbles of hydrogen from adhering to the cathode and causing pits in the deposit. It reduces the surface and interfacial tension [3, 4]. The normal operating temperature of the Ni electroplating solution is 50 ~ 52 ℃ and pH value is about 3.5 ~ 3.8. Ni sulfamate solutions are most commonly used electrolyte for electroplating in engineering applications. They are capable of high plating rate, low residual stress and good ductility [5].

3.3 Ni electroplating of proton beam fabrication resist structures

Ni mold fabricated with PBW and electroplating has already proven to be a remarkable approach. Details down to 100 nm wide and 2 μm high ridges have been fabricated in Ni mold fabricated by PBW of PMMA resist and electroplating [6]. Up to now thick negative resist materials are a challenge in combination with PBW and Ni electroplating; SU-8 is negative photoresist which can't be easily removed after PBW and Ni electroplating and is therefore not suitable for Ni mold fabrication. HSQ is also a negative photoresist having a very high resolution, but the thickness of HSQ is limited to sub-micron thickness. Ni molds have been used in many application areas, such as advanced printed circuit board [7], polymer microlens replication [8] and some other optical devices [9]. However, most of the applications based on high aspect ratios (can be over 20) feature Ni molds with large structure sizes (several microns) [7] or high resolution (sub-100 nm) Ni molds with low aspect ratio (typically less than 2) [9]. Ni molds with high aspect ratio and high resolution structures are still hard to achieve.

In this section, we present Ni electroplating for micro- and nanostructures with some new negative photoresists as well as PMMA. The micro- and nanostructures are first fabricated in these resists, for a detailed description see

chapter 2. Then the sample is put into the electroplating cell shown in Fig 3.2 to perform electroplating. Basically, there are two methods of electroplating to transfer the resist structures to Ni. In the first method the resist is taller than Ni, here typically the Ni remains on the Si and forms the final product. In the second approach the Ni is grown much thicker than the resist layer and is removed from the Si substrate to form a Ni mold.

In both methods a conductive Au/Cr layer is required on the Si wafer as a seed layer for the plating process. After development the resist structures are electroplated with Ni. As can be seen from Fig. 3.4, Ni starts to grow on the surface of the Au layer. In this method, we need to make sure that the height of Ni is lower than the height of resist. After Ni electroplating, the resist is removed and the intended Ni structures remain on the Si wafer.

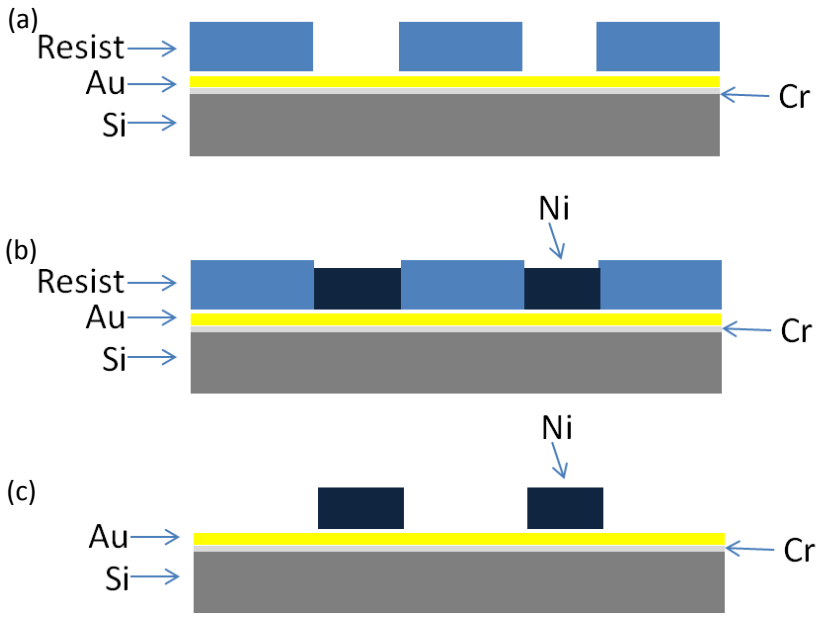

Fig. 3.4 Ni electroplating (a) resist structures, (b) Ni electroplating (Ni is lower than resist), (c) resist removal

In the second method the goal is to fabricate Ni mold, shown schematically in Fig. 3.5. The first step is the same as in the first method. To achieve a conductive layer on top of the resist, required for a smooth plating process, a thin layer of Ti is applied on the surface of the sample using filtered cathodic arc vacuum deposition method, followed by Ni electroplating. As can be seen

from Fig. 3.5, Ni keeps depositing on the sample when Ni reaches the top surface of the resist. In this way, after Ni electroplating and removing Si and resist, an entire Ni mold with structures is fabricated. In our research, both methods have been tested and can achieve high quality Ni structures.

SU-8 and HSQ are popular resist materials in PBW and sub-60 nm details with high aspect ratio have been demonstrated [10, 11]. However, SU-8 and HSQ are not easily removed after PBW and electroplating. In order to expand the applications of PBW in nanoimprinting as well as injection molding, it is very important to investigate new resist materials which are suitable for the combination of PBW and nanoimprinting as well as injection molding. Several kinds of resist consisting of ma-N series, PMMA series and ARP series will be discussed in combination with Ni electroplating. We will give the results based on these materials in the next sections.

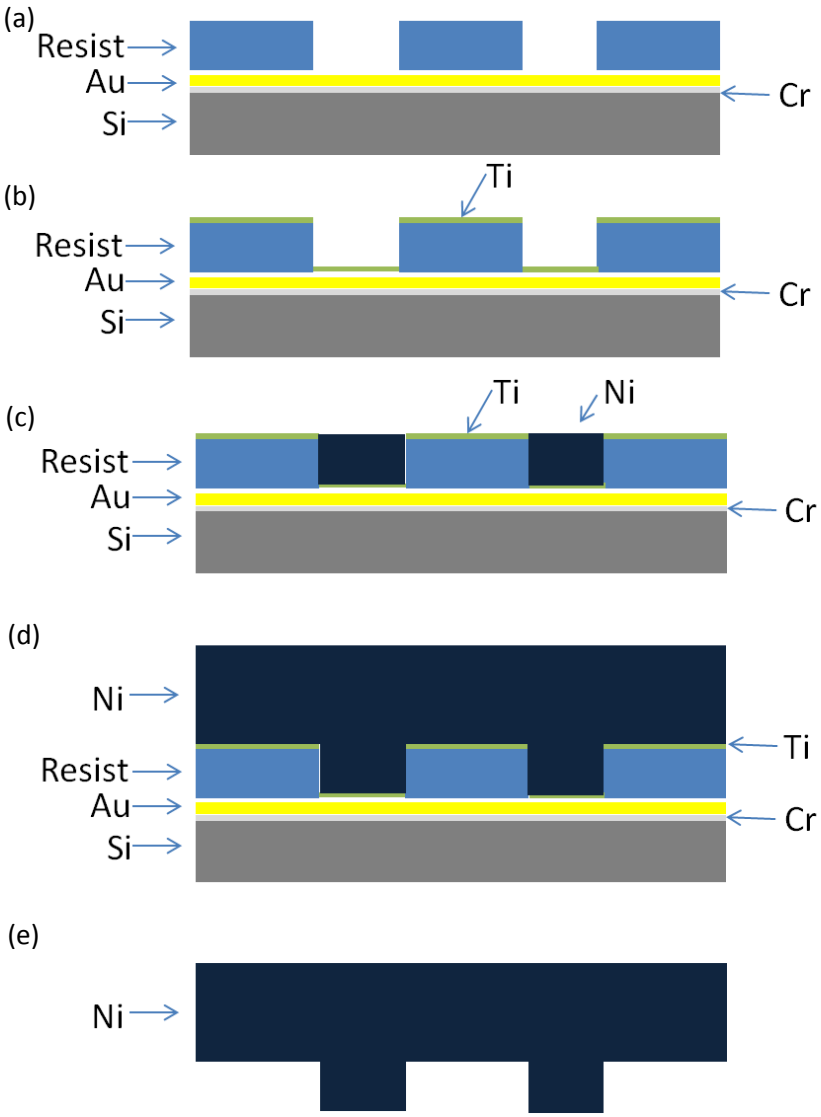

Fig. 3.5 Ni mold fabrication (a) resist structures, (b) Ti sputtering, (c) Ni electroplating to the top layer of resist, (d) over Ni electroplating, (e) resist removal

3.3.1 Ni molds fabricated with ma-N series resist

ma-N series resist is negative tone resist to PBW, since it forms a dense cross-linked network after PBW it can't be easily removed after Ni electroplating. ma-N 2401 is a high resolution negative resist for PBW. Line width down to 60 nm has been fabricated with PBW (see chapter 2). However, ma-N 2401 has a similar problem as SU-8 that it cannot be easily removed after Ni electroplating when the size of the structure is small. It is difficult to make a high resolution Ni mold with ma-N 2401. However, ma-N 2401 is designed to achieve high resolution structures in thin resist layers. ma-N 2410 belongs to the same series with ma-N 2401. ma-N 2410 is designed to achieve hundreds of nm structures in μm range thick resist. It also has the same problem of removing after electroplating if the structures are very small. ma-N 2410 was spin coated at 3000 rpm for 30 s which yielded a layer of 1 μm thick. ma-N 2410 was exposed using a 1 MeV proton beam focused down to a spot size of 100 nm × 120 nm using a dose of 70 nC/mm^2. After PBW the sample was developed in ma-D 525 for 130 s, rinsed with DI water for 3 min and air dried.

The experimental procedures for electroplating with resist ma-N 2410 are shown in Fig. 3.5. Ni will be deposit on the conductive surface area of the sample that is exposed to the electrolyte. Ni is electroplated at a plating rate of 52.08 A/dm^2 for 100 min reaching 10 μm followed by 520.8 A/dm^2 for 41.5 hours reaching 2490 μm, yielding a total thickness of 2.5 mm.

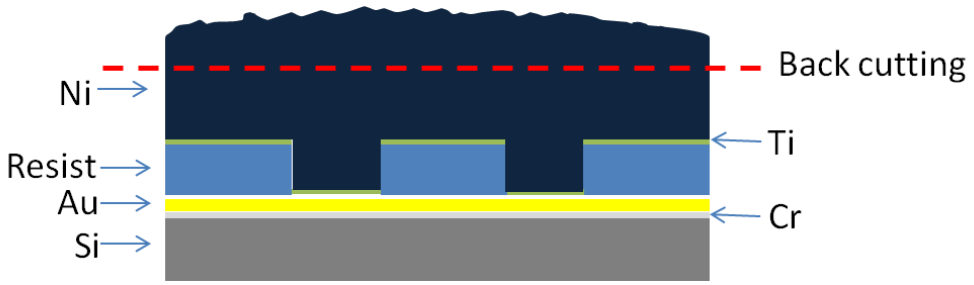

Fig. 3.6 Schematic sectional back cutting of the sample after plating

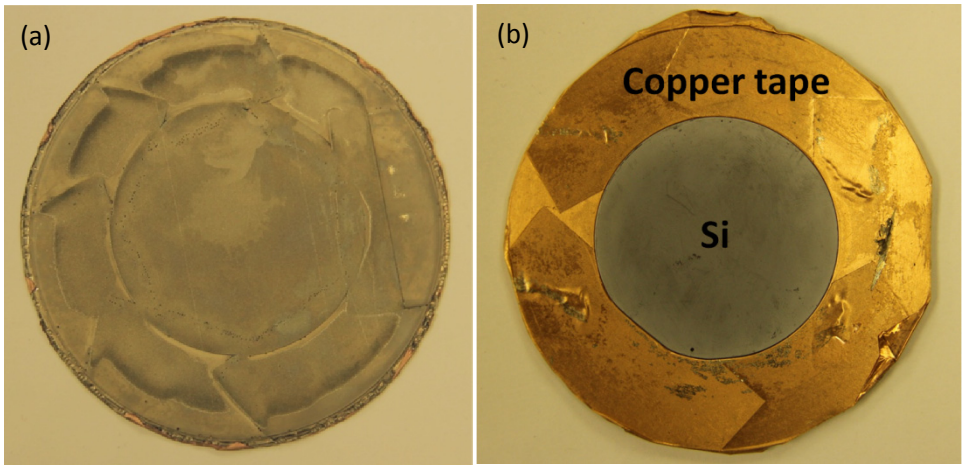

Fig. 3.7 Sample after Ni electroplating (a) Back side after cutting, the central part is very flat, (b) Front face of Ni, the central part is Si wafer, the other part is copper tape

After Ni electroplating the whole sample has a round shape with a diameter of 8.5 cm, regardless of the sizes of micro- or nano-structures. However, the surface of the Ni mold is not very flat. As a result, back cutting of Ni needs to be done. Fig. 3.6 shows the back cutting of Ni. Ni was plated to 2.5 mm, and it was cut to achieve a thickness of 2.0 mm using Sodick wire-cut machine.

Fig. 3.7a shows the back side of the mold after cutting. The front face of the Ni mold is shown in Fig. 3.7b. The grey part in the center is a Si wafer. The surrounding part is copper tape.

After back cutting, the whole sample was put into acetone for 2 hours to separate the Ni mold and Si wafer, the resist was dissolved in acetone. The next step is to cut the sample to a square of 21 mm × 23 mm. The machine we used is wire spark erosion machine. Fig. 3.8 shows the procedures of cutting. To protect the micro- and nano-structures on the Ni mold, a 5 µm thick layer of AR-P 3250 was spin coated on the Ni mold to act as a protection layer. Since we used wire spark erosion, the material needs to be electrically conductive and therefore free from resist. A piece of aluminum foil was put on the top of the area of the structures to avoid UV exposure, while other areas

were exposed. The sample was then put into AR 300-26 to remove the exposed resist. As a result, only the resist covering structures stayed on the Ni. Then the Ni mold was cut to a 21 mm × 23 mm square. After side cutting, the 21 mm × 23 mm square was rinsed in acetone for 5 min to remove the unexposed AR-P 3250, yielding a Ni mold that can be used in nanoimprint lithography experiments.

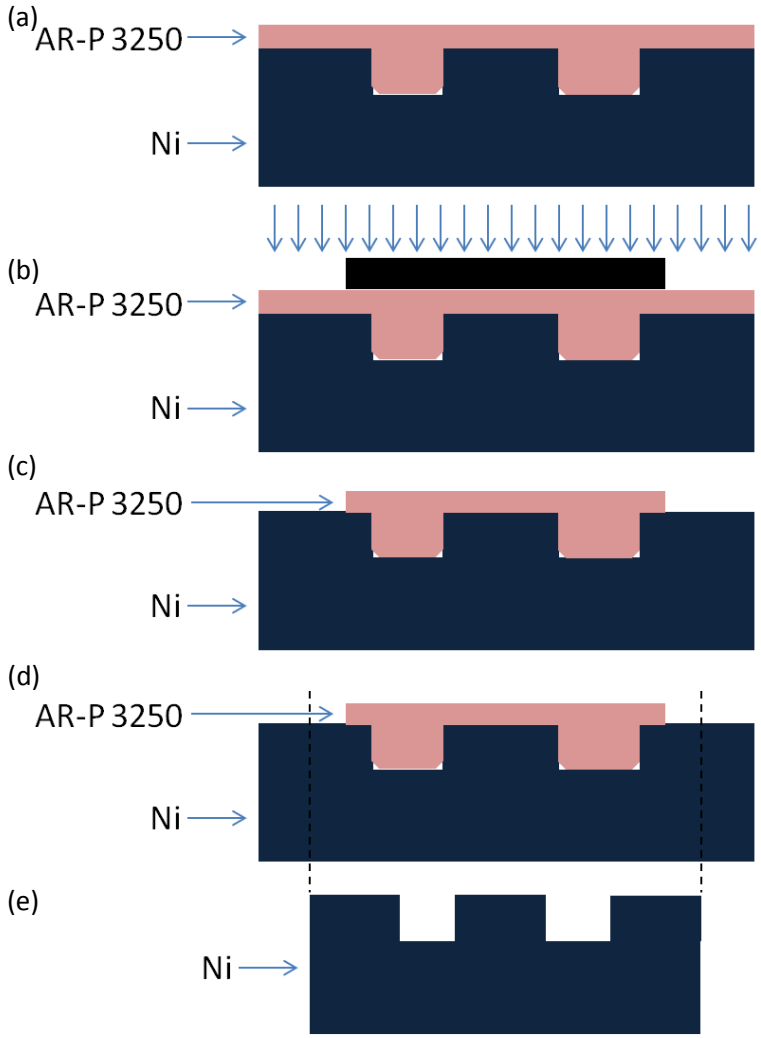

Fig. 3.8 Procedures from coating protection layer to side cutting (a) coating of AR-P protection layer, (b) UV exposure, (c) development, (d) wire spark erosion cutting to obtain the desired size, (e) mold cleaning with acetone

Fig. 3.9 shows SEM image of the structures in ma-N 2410 and Ni mold. As can be seen from the Fig. 3.9a, the smallest line is 500 nm wide and 1 μm

high. After resist structures are fabricated, a 6 nm Ti layer was coated on the sample as a secondary seed layer for Ni electroplating. Fig 3.9b shows an electron microscope image of the narrowest grooves in the Ni mold. As can be seen from the figure, the resist structures were accurately transferred to Ni. The smallest channel is 500 nm wide and 1 µm deep. The Ni mold has been used for nanoimprinting as well as injection molding, see chapters 4 and 5 for more details.

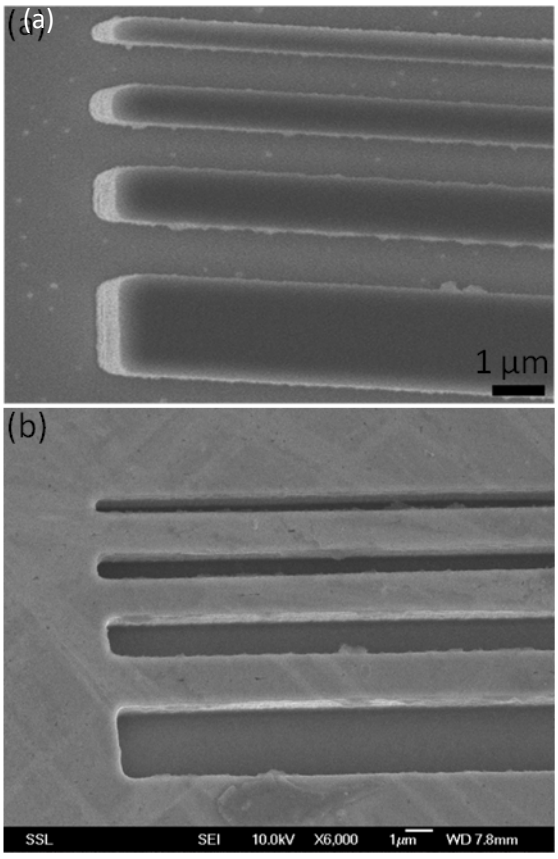

Fig. 3.9 (a)Electron microscope image of ma-N 2410 structures written with a 1 MeV proton beam in a 1 µm thick resist layer (b) SEM image of the micro-channels in Ni mold

3.3.2 Ni pillars and molds fabricated with 950k PMMA

PMMA is positive resist to both PBW and UV (wavelength: 248 nm). This resist is suitable for Ni electroplating, because after Ni electroplating, the resist can be easily removed with acetone. Ni molds with structures down to 100 nm and high aspect ratio (~20) features, 7-nm RMS-side-wall roughness have been realized [6]. In our research, PMMA was used to fabricate Ni pillars on Si as well as Ni molds with micro- and nanofeatures.

Ni pillars

As the interest of field emission applications is growing, it is critical to fabricating uniform, vertically aligned and well-ordered pillars for field emission [12]. Using our technique, it is easier to realize this. In our experiment, the Si wafer was pre-coated with a 60 nm Au layer which acts as a seed layer for electroplating and a 30 nm Cr layer acting as a glue layer. Before spin coating, the wafer was baked at 200 ℃ for 30 min followed by air cooling for 3 min. PMMA 950 A11 from MicroChem was spin coated at 2000 rpm for 30 s, followed by a bake at 180 ℃ for 90 s. Totally 3 coats were applied. This procedure yielded a layer of 9 μm thick PMMA. In the p-beam writing experiments an array of 20 × 20 holes spaced 10 μm was exposed with 2 MeV protons. The beam was focused down to a spot of 100 nm × 150 nm. Large proton doses in one pillar lead to a large size pillar, and also the shape of the pillar becomes more elliptical because of the different focusing size in X and Y directions as well as more slit scattering in Y direction [13]. We put 40,000 protons per pillar. The development time was 10 min. Ni electroplating was also performed with current density of 52.08 A/dm^2 corresponding to a speed of 0.1 μm/min. The height of the Ni pillars is aimed at about half of the height of the resist. In order to ensure the height of Ni pillar not exceed the height of PMMA, a much thicker layer of PMMA (9 μm) was used. After electroplating the resist was removed in acetone for 30 min the resulting Ni

pillars had a height of about 4.5 μm. As can be seen from Fig 3.10, the size of the pillar at the top is about 500 nm. However, at the bottom the size is much larger, which is about 820 nm. This can be attributed to the following reasons; firstly, the beam spread as it penetrates into the thick photoresist. Fig. 3.11 shows the distribution of proton in the 9 μm thick PMMA. The crossing point between the curve and the arrows means 90% of the protons land within this distance. For 1, 2 and 3 MeV protons, the crossing point obtained from SRIM [14] is 185 nm, 90 nm and 41 nm respectively. As a result, higher energy proton beam spreads less. If 3 MeV protons are used, the size of the pillar would be smaller at the base compared to the results presented here, choosing a thinner resist layer would also have resulted in a narrower base.. However, considering the stability of accelerator, the highest energy is usually 2 MeV. Secondly, 40,000 protons per pillar are too much. According to SRIM simulation, if we take 99.5% of the 40,000 protons at the depth of 4.5 μm and 9 μm, the beam will spread 113 nm and 355 nm, respectively. This gives a simulated pillar size of 376 nm (113+113+150) and 855 nm (355+355+150) which is close to the actual pillar. Thirdly, the development time is an important factor in the final size of the pillars, and it also affects the roughness of the pillar. Control of these parameters will enable to the production of smaller and smoother metallic nanowires.

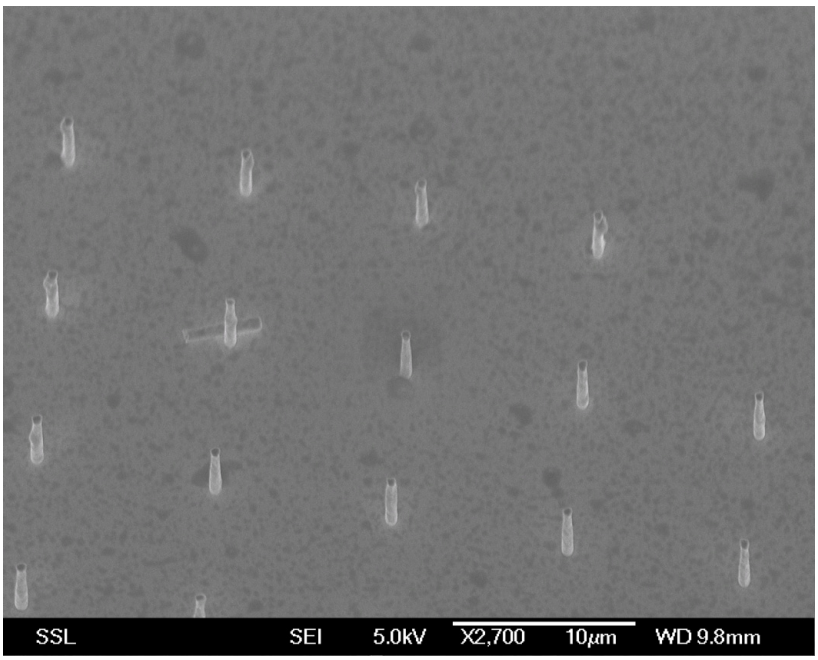

Fig. 3.10 Ni pillars with a diameter of 500 nm at the top

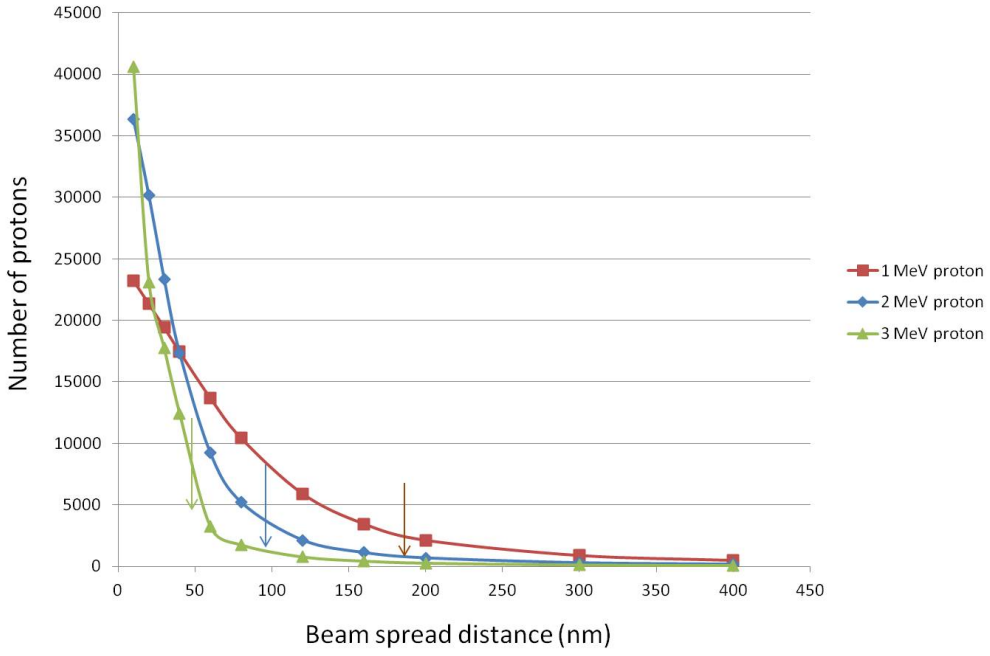

Fig. 3.11 The distribution of 1, 2 and 3 MeV protons into 9 μm thick PMMA, the crossing point between the curve and arrows means 90% of protons land within this distance [14]

Ni molds

To fabricate Ni molds with PMMA resist, the second method of electroplating was carried out (see Fig 3.5). The process starts with coating of 20 nm Cr and 60 nm of Au on a Si wafer, this layer acts as a seed layer for Ni electroplating. Next a layer of PMMA 950 A11 is spin coated on the wafer at 6000 rpm for 30 s. The thickness of PMMA 950 A11 is about 1 μm. The PMMA layer is exposed using a 1 MeV proton beam focused down to a spot size of 130 nm × 150 nm using a dose of 100 nC/mm². During the exposure, we use the focused beam to draw a circle whose diameter is 300 nm. After PBW the sample is developed in a mixture of IPA and DI water (7:3) for 2 min, rinsed with DI water for 3 min and air dried. To guarantee a smooth formation of the Ni mold during the electroplating process, a 6 nm Ti layer is coated on the sample as a secondary seed layer for the Ni electroplating using the filtered cathodic arc vacuum deposition method. Then the sample was mounted on the Ti plate using conductive copper tape to cover the edge of the sample which is then covered with isolation tape. The Ti plate is mounted in the plating machine and electroplating is carried out. During electroplating, Ni is first plated in the holes. When Ni grows up to the top of the holes and touches the Ti on the surface of the PMMA, Ni will be electroplated on the whole surface of the sample. Ni is electroplated at a plating rate of 1681 A/dm² for 1000 min reaching 500 μm. Then we put the whole sample into acetone for about 10 min to separate the Si and resist from the Ni mold. Fig. 3.12 shows a SEM image of Ni pillars in Ni mold featuring vertical and smooth sidewall. The size of the pillars is about 300 nm × 500 nm. The pillars are not perfectly circular. When we use the focused beam to draw a circle, the beam spot in X and Y is not the same size, because there is considerable beam scattering in Y direction due to the small object slit setting in Y direction.

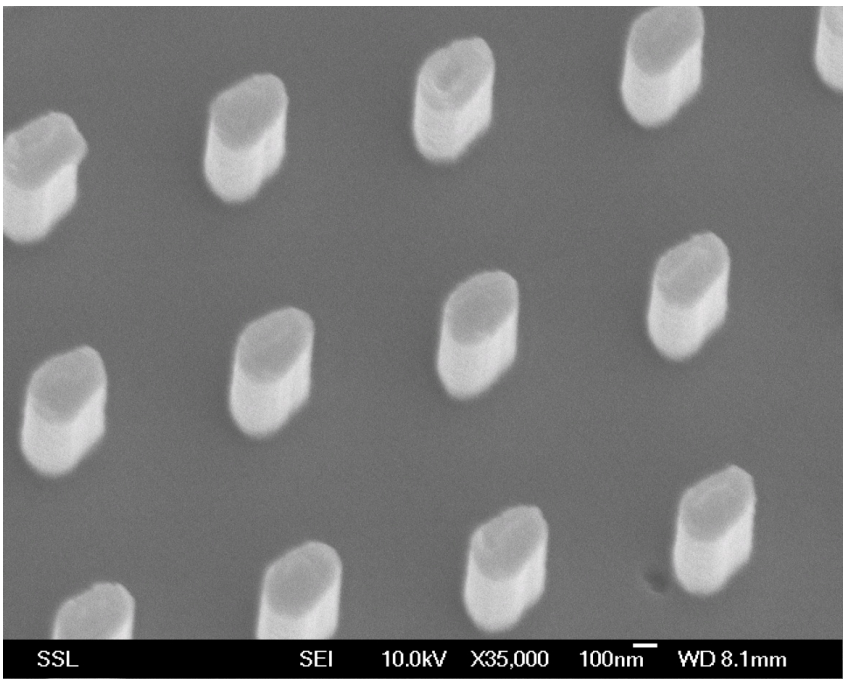

Fig. 3.12 Ni electroplated mold featuring 300 × 500 nm^2 wide and 1 μm high pillars plated in a 1 μm thick PMMA resist layer written with a 1 MeV proton beam

Ni molds with micro- and nanochannels were also fabricated with the same method. Au and Cr were pre-coated on a Si wafer as seed layer for electroplating. Then PMMA 950 A11 was spin coated at 6000 rpm for 30 s and baked at 180 ℃ for 90 s. This yielded a layer of 1μm thick PMMA. The resist was exposed by 2 MeV proton beam which was focused down to 120 nm × 150 nm with a dose of 150 nC/mm^2. After irradiation, the sample was developed in IPA: DI water=7: 3 for 2 min, rinsed in DI water for 3 min and air dried. Fig 3.13 shows an optical image of the structures after development the center 40 μm × 100 μm was written with the proton beam using magnetic scanning. The 5 μm wide feeding channels were written using a combination of stage and beam scanning. The length of the 5 μm wide channel is 1.5 mm. The width of the 13 parallel channels in the center of the design is about 500 nm.

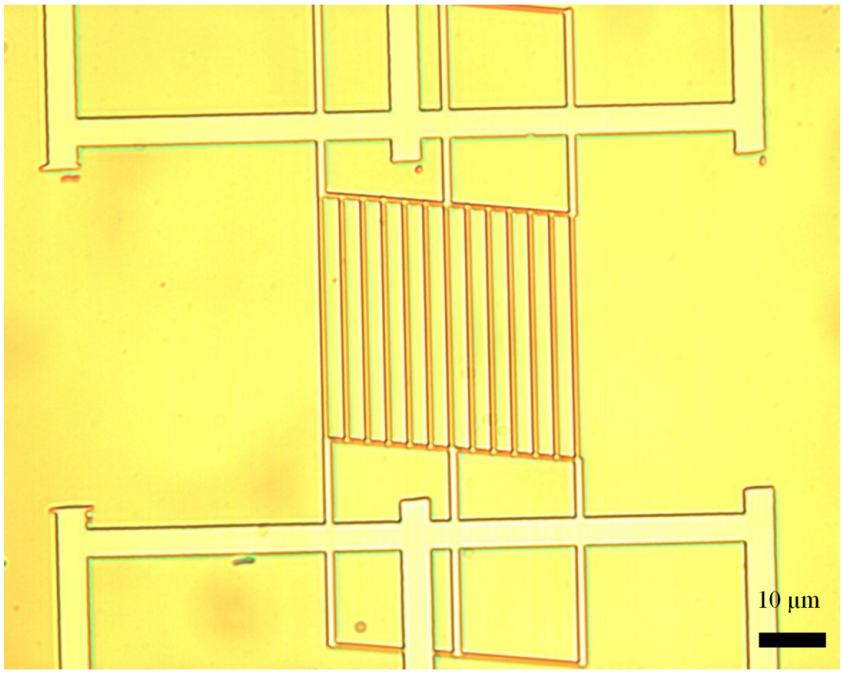

Fig. 3.13 Optical image of channels fabricated using a 2 MeV proton beam in a 1 µm thick PMMA layer

After PBW, a layer of 6 nm Ti was coated as the second seed layer for electroplating. The plating rate was first set at 0.1 µm/min corresponding to a current density of 52.08 A/dm^2 for 100 min, reaching 10 µm followed by 520.8 A/dm^2 for 41.5 hours reaching 2490 µm, yielding a total thickness of 2.5 mm. The mold was first cut from the back to reach a thickness of 2.0 mm, yielding a flat backside surface parallel to the front surface. Following the steps in Fig. 3.8, a Ni mold with the desired dimensions of 21 mm × 23 mm × 2 mm was fabricated.

Fig 3.14 shows SEM images of the fine ridges in the Ni mold, the width of the smallest ridges is 500 nm and the height of the ridges is 1 µm, corresponding to an aspect ratio of 2. As can be seen, all the resist was completely removed by rinsing in acetone for 30 min. The Ni mold will be used in both nanoimprinting and injection molding experiments (more details can be found in Chapters 4 and 5).

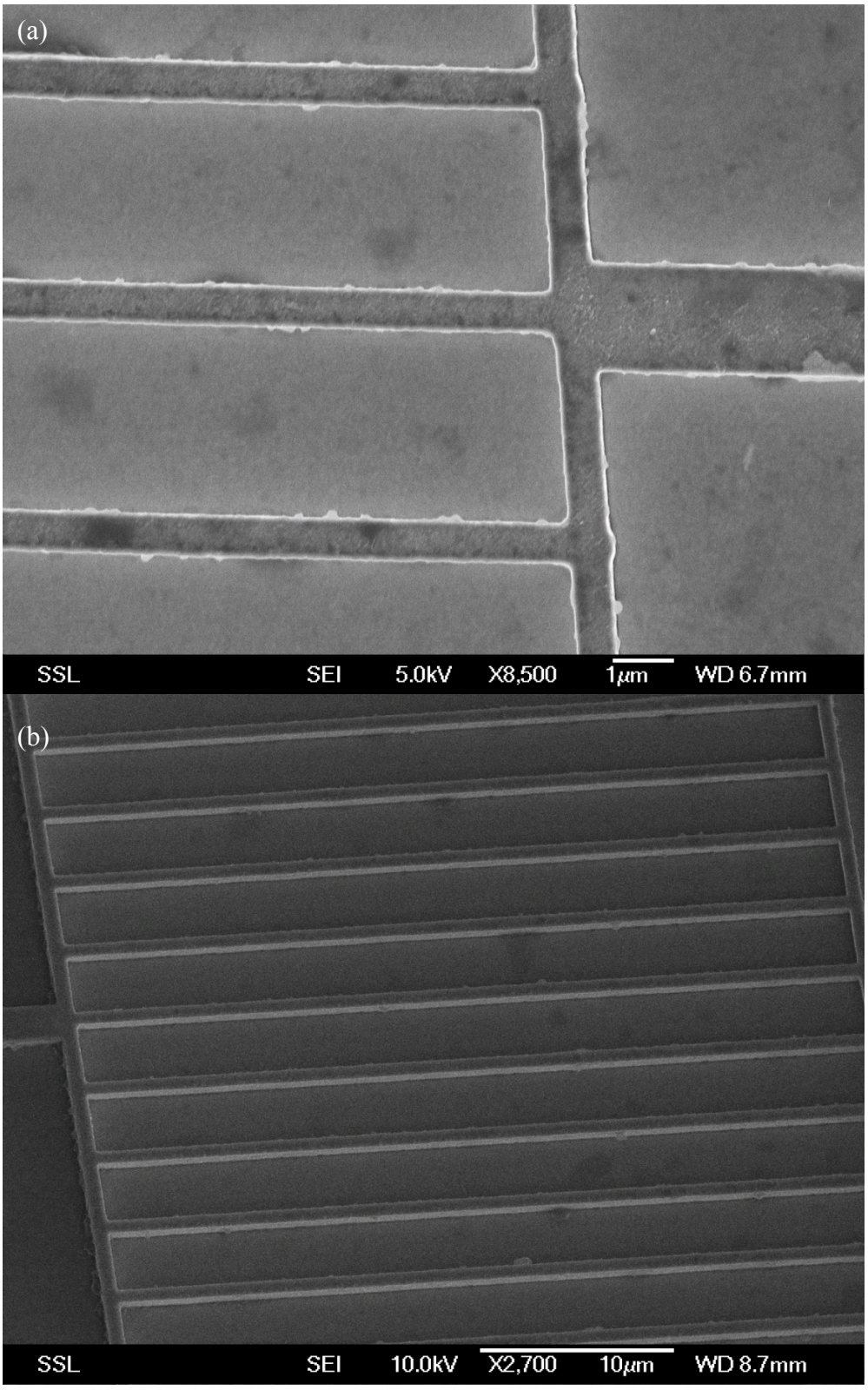

Fig. 3.14 (a) Top view of ridges in the Ni mold (b) tilted view of ridges (15^{o}tilt)

3.3.3 Ni molds fabricated with AR-P 3250

To evaluate Ni molds fabricated using PBW in combination with AR-P 3250 resist high aspect ratio nanostructures were written with the proton beam. A 4 μm thick AR-P 3250 layer was spin coated at 6000 rpm, irradiated with 1 MeV protons at a dose of 50 nC/mm^2, followed by UV exposure for 7 min using the 100 W lamp (365 nm) and development in AR 300-26: DI water=1: 1 for 1 min. After development, the sample was rinsed in DI water for 1 min and air dried. A second seed layer---6 nm Ti as a seed layer for electroplating was coated on the sample. Electroplating was carried out at a plating rate of 260.4 A/dm^2 for 1000 min reaching 0.5 mm. Si and Ni were separated by acetone for 10 min with agitation. The Ni mold was trimmed to the correct dimensions (21 mm x 23 mm x 2 mm) using wire spark erosion, following the procedure as described in Fig. 3.6 & 3.8. The sample was coated with a 6 nm thick Ti layer. Electroplating was at a rate of 260.4 A/dm^2 for about 33.5 hours, yielded a total thickness of 1.0 mm. SEM figures of the structure after resist removal are shown in Fig 3.15.

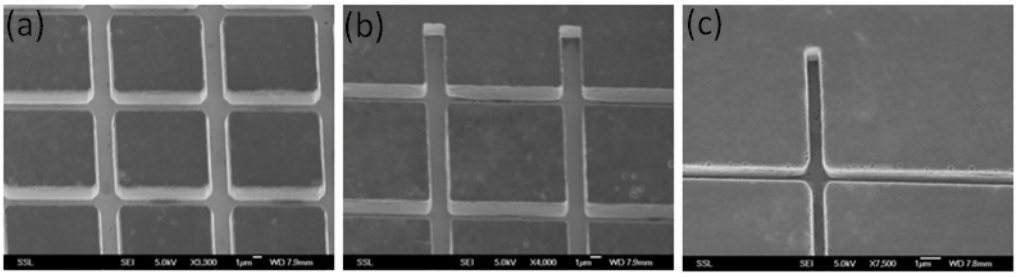

Fig. 3.15 Grooves with a depth of 4 μm in the Ni mold obtained via electroplating on AR-P3250 resist, featuring groove width of (a) 1.8 μm, (b) 1.4 μm and (c) 500 nm

As can be seen from Fig. 3.15, the resist in the channels is completely removed. The depth of the grooves is also 4 μm nicely matching the height of the original AR-P 3250 resist layer. In order to get even smaller structures, AR-P 3250 was spin coated at 8000 rpm to get a 3.5 μm layer. After

electroplating and resist removal for 2 hours in acetone, 330 nm wide grooves were realized in Ni, see Fig 3.16.

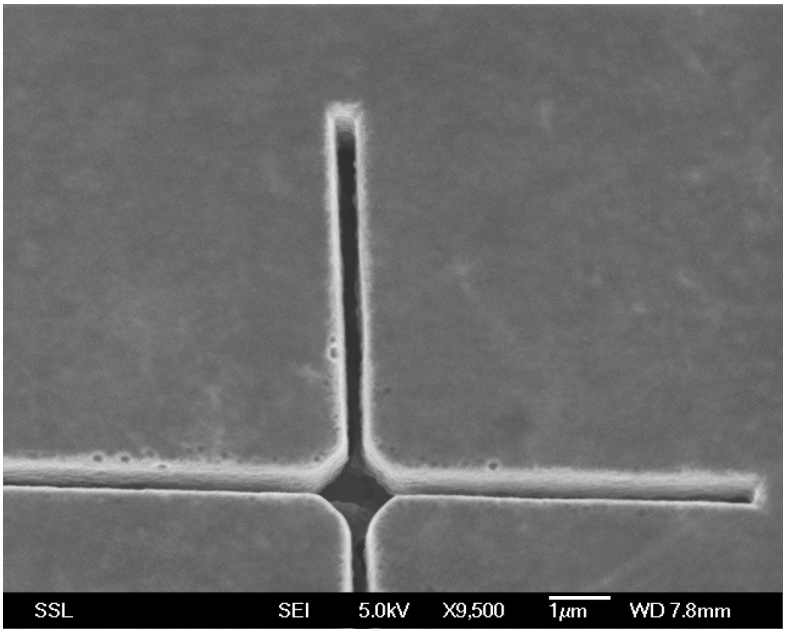

Fig. 3.16 SEM images of 330 nm wide and 3.5 μm deep grooves in Ni mold

3.3.4 Ni molds fabricated with mixture resist (AR-P 3250: AR 300-12= 1:3)

It is well known that high aspect ratio resist structures are not very stable and can fall over [15]. In our experiment, AR-P 3250 and AR 300-12 were mixed with a ratio of 1:3. Before resist coating, a Si wafer was coated with Au and Cr and baked at 200 ℃ for 30 s to remove any moist. Then, the mixture was spin coated at 4000 rpm for 30 s followed by a pre bake at 95 ℃ for 30 s. This yielded a layer thickness of 280 nm. A 1 MeV proton beam focused down to 100 nm × 150 nm was used to pattern the resist. Details down to 120 nm have been fabricated at a dose of 50 nC/mm^2 by PBW and UV (365 nm, 100 W lamp) exposure for 1 min, followed by development in AR 300-26 developer (1:1 diluted with DI water) for 20 s. The aspect ratio of the line is about 2.5. To perform electroplating, a layer of 6 nm Ti was coated to act as a secondary seed layer for electroplating. Electroplating at a rate of 104 A/dm^2 for about 42

hours, yielded a total thickness of 0.5 mm. After electroplating, the Si wafer and Ni mold were separated by ultrasonic and acetone cleaning for 20 min. As can be seen in Fig. 3.17, the structures were accurately transferred to Ni and all the resist in the grooves was completely removed by the acetone. As a result, the mixture resist is a suitable resist for higher resolution structures in Ni mold fabrication.

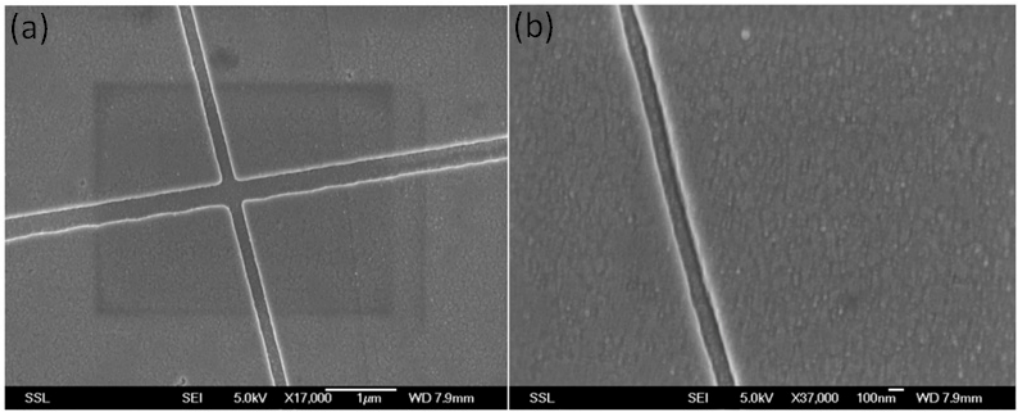

Fig. 3.17 (a) 150 nm and (b) 120 nm wide with 280 nm height grooves in Ni mold

3.4 Summary

In this chapter, the theory of Ni electroplating was introduced followed by the facility used for Ni electroplating in our project. Then the Ni mold fabricated with the new negative photoresists ma-N, AR-P 3250, and diluted AR-P 3250 with AR 300-12 were introduced. Table 3.2 shows the results achieved in Ni mold fabricated by different resists.

Table 3.2 Results achieved in Ni mold fabricated by different resists

Resist	Minimum size (nm)	Aspect ratio
ma-N 2410	500	2
AR-P 3250	330	10.6
Mixture resist (AR-P 3250: AR 300-12=1: 3)	120	2.3

Ni mold with an aspect ratio of 2 with a minimum structure size of 120 nm can be achieved. A higher aspect ratio up to 10 with structures down to 330 nm was achieved using AR-P 3250.

Ni pillars and Ni mold fabricated with PMMA were also studied in this chapter. The molds were used in nanoimprinting and injection molding to realize mass production of plastic replication. In the next two chapters, I will give an introduction of nanoimprinting and injection molding. Some results based on these techniques will also be given.

References

[1] Stelter, M., Bombach, H., *Process Optimization in Copper Electrorefining*". Advanced Engineering Materials 6: 558, 2004

[2] Watts, O. P., Transations of the American Electrochemical Society, v 29, p 395-03, 1916

[3] T. Saito, E. Sato, M. Matsuoka, and C. Iwakura, *Electroless deposition of Ni-B, Co-B, and Ni-Co-B alloys using dimethylamineborane as a reducing agent*, Journal of Applied Electrochemistry, 28:559–563, 1998

[4] S. Alec Watson, *Organic addition agents for nickel electroplating solutions*, NiDI Technical series N 10 048, 1989

[5] M. Schlesinger and M. Paunovic, *Modern electroplating*, Prentice Hall, Englewood Cliffs, New Jersey, 1991

[6] K. Ansari, J. A. van Kan, A. A. Bettiol and F. Watt, *Fabrication of high aspect ratio 100 nm metallic molds for nanoimprint lithography using proton beam writing*, Applied Physics Letters 85, 476-478**,** 2004

[7] H-S Lee, H-H Yang, S Ra, J-B Yoon, Fabrication of a large-scale Ni stamp using a multi-level SU-8 photoresist mold for advanced printed circuit board, J. Micromech. Microeng. 21 (2011) 065026

[8] R.K. Dutta, J.A. van Kan, A.A. Bettiol, F. Watt, Polymer microlens replication by nanoimprint lithography using proton beam fabricated Ni stamp, Nucl. Instr. Meth. B260 (2007) 464-467

[9] S.H. Oh, S.U. Cho, C.S. Kim, Y.G. Han, C-S Cho, M.Y. Jeong, Fabrication of nickel stamp with improved sidewall roughness for optical devices, Microelectronic Engineering 88 (2011) 2900-2907

[10] J.A. van Kan, T.C. Sum, T. Osipowicz, F. Watt, *Sub 100 nm proton beam micromachining: theoretical calculations on resolution limits*, Nucl. Instr. Meth. B 161, 366-370, 2000

[11] J.A. van Kan, A.A. Bettiol and F. Watt, *Proton Beam Writing of 3D Nanostructures in Hydrogen SilsesQuioxane*, Nano letters, 6, 579-582, 2006

[12] Hua Qin, Hyun-Seok Kim, Robert H Blick, *Nanopillar arrays on semiconductor membranes as electron emission amplifiers*, Nanotechnology 19 095504, 2008

[13] J. A. van Kan, F. Zhang, A. A. Bettiol, F. Watt, *Proton beam writing: a platform technology for nano-integration*, Proc. SPIE 6921, Emerging Lithographic Technologies XII, 69210K, March 20, 2008

[14] J. F. Ziegler, *The stopping of energetic light ions in elemental mater*, J. Appl. Phys/Rev. Appl. Phys., 85, 1249-1272, 1999

[15] H. Duan, Joel K.W. Yang, K. K., *Controlled collapse of high-aspect-ratio nanostructures*, Berggren Small, 7, 2661-2668, 2011

Chapter 4 Introduction to Nanoimprint Lithography and Applications of Ni Molds

In this chapter, I will first give an introduction to nanoimprint lithography (NIL) and discuss its' recent development. In the second half I will present some results based on Ni molds fabricated using PBW and electroplating for NIL applications.

4.1 Introduction to Nanoimprint Lithography (NIL)

NIL is a method of fabricating micro or even nanometer scale patterns which enables low cost, high throughput and high resolution. This technique creates patterns by mechanical deformation of imprint resist and subsequent processes. The resist that can be used in NIL is usually a polymer formulation that can be cured by heat or UV light during imprinting.

This idea was first proposed in 1995 when Stephen Y. Chou reported sub-25 nm holes made in polymethyl methacrylate (PMMA) polymer with an imprinting mold [1] (patented in 1998) [2]. Since then NIL has undergone phenomenal growth, NIL has been the subject of active research and development in the last 15 years. In 1997, 6 nm diameter and 65 nm period holes were fabricated in PMMA on Si substrate. NIL was also used together with optical lithography to fabricate Si quantum dot, wire, and ring transistors, Chou showed [3] that NIL fabricated devices showed the same behavior as those fabricated using conventional e-beam lithography. In 1999 the first polymer-based optical device was realized [4] and an alignment system with 1 μm accuracy over 4 inch wafer was introduced [5]. In 2003, NIL was added to

the International Technology Roadmap for Semiconductors (ITRS) for the 32 and 22 nm nodes [6].

Over these years of development, NIL has been used to fabricate devices for electrical, optical, photonic and biological applications. Si nanotransistors, GaAs metal-semiconductor-metal high speed photo-detectors, ring resonators and organic film transistors have been achieved using NIL [3, 7, 8, 9].

In 2011, inclined NIL was performed to realize 3D nanofabrication, this showed great application potential in photonics, plasmonics, nanotribology and NEMS [10]. In 2012, 25 nm pitch bit patterned media production was successfully realized by NIL [11].

Although NIL is a very simple and capable of high resolution, there are still problems and limitations. To provide a uniform parallel pressure distribution over a large area substrate is a challenge in NIL, hindering high quality large area imprinting. Many different approaches have been developed to overcome this difficulty such as air cushioning [12], and parallel flat imprinting under vacuum [13].

Traditional nanoimprinting requires relatively high temperature to soften the polymer and relatively high pressure to press the mold into the polymer. Heating and cooling cycle prolongs the nanoimprinting process which it is not ideal for high-throughput manufacturing. The need for high pressure can increase the wear of mold. As a result, other forms of NIL which don't require high temperature and high pressure like UV-cured nanoimprinting have been developed. In this section, I will introduce the two most important NIL methods: thermoplastic nanoimprint lithography and UV-cured nanoimprint.

4.1.1 Thermoplastic nanoimprint lithography

Thermoplasitc nanoimprint lithography was the first proposed replication process at nanometer scale [1]. Sometimes it can be confused with hot embossing, as hot embossing refers to the same replication process as thermoplastic nanoimprint lithography. However, the main difference between them is the size of the structures they can replicate. Hot embossing usually refers to making structures above a micrometer or tens of micrometers, while nanoimprinting refers to making small structures often less than a micrometer. For thermoplastic nanoimprint lithography, the basic process is schematically illustrated in Fig. 4.1. A mold with micro- and nanostructures is first fabricated. Then a layer of polymer is coated on a flat substrate. The sample is heated to a temperature above the glass transition temperature (T_g) of the polymer so that it can be deformed.

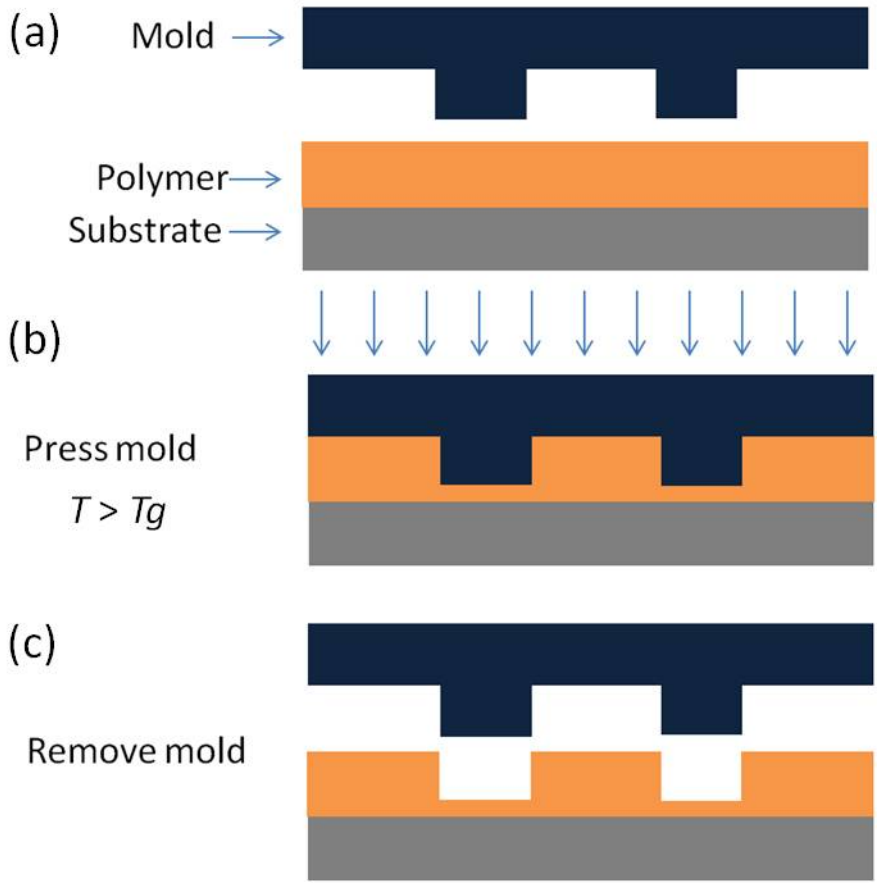

Fig. 4.1 Schematic of nanoimprinting process

Then the mold with micro- and nanostructures is pressed into the polymer layer at a certain pressure, depending on the viscosity of polymer. The next step is to separate the sample and the polymer layer when they are still warm [14]. The thickness of the polymer layer should be larger than the height of the structures in the mold in order to avoid hard contact with the substrate and prevent any damage to the mold. Fig. 4.2 shows a plot of temperature and pressure at different stages of the imprinting process.

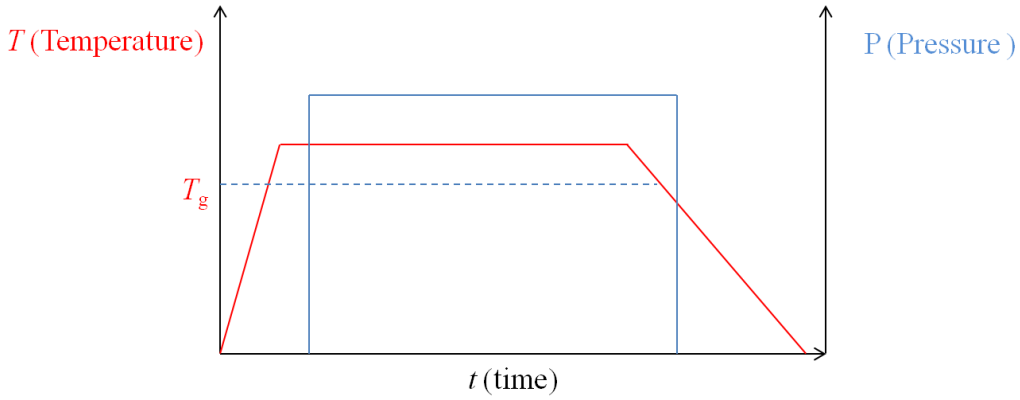

Fig. 4.2 Temperature and pressure evolution during thermal press nanoimprinting

First the mold and substrate are brought in contact, next the temperature is raised above T_g and the pressure is increased and held for a certain amount of time. This is followed by temperature release to about 10 ℃ below T_g, at which point the pressure is released. Finally after cooling a bit more, the mold and the imprinted sample are separated. After separation, the impression of the mold pattern is left in the polymer layer.

Nanoimprint molds

In the replication process, the mold plays a key role in replicating micro-nanostructures in polymer, because the replicated structures can only be as good as the structures in the master. For thermoplastic nanoimprint lithography, the molds should be capable to withstand high temperature and high pressure without significant wear. There are many materials that can be used as nanoimprint molds. The most commonly used materials are silicon, silicon dioxide, silicon nitride and various metals. The molds made of silicon, silicon dioxide and silicon nitride are fabricated via resist patterning followed by reactive ion etching (RIE) [15, 16, 17, 18]. Molds made of oxide or nitride can be easily broken under a non-uniform pressure. The best and most durable mold is made of Ni [19]. The Ni mold fabrication process has been discussed in Chapter 3. There are also other molds---Hydrogen silsesquioxane (HSQ) resist with a post bake after development at 500 ℃ transforming HSQ

essentially into silicon dioxide which can directly be used as a mold for nanoimprint [20].

Nanoimprint Polymers

A good quality high-resolution mold is important for NIL, however, the polymers that can be used in NIL are also critical. The characteristics of good nanoimprinting polymers are a low glass transition temperature (T_g) to enable low imprinting temperature, low viscosity [21] to help facilitate easy flow of the polymer to and low shrinkage to maintain pattern fidelity after imprinting. Once a polymer is heated above its glass transition temperature, it will fill the cavities of the mold under applied pressure. The force F can be expressed by Eq. (4.1) [22]:

$$F = -\frac{3\pi R^4}{4h_0^3}\frac{\mathrm{d}h}{\mathrm{d}t}\eta_0, \tag{4.1}$$

Where R is the radial flow distance, h_0 is the initial thickness of polymer layer, dh/dt is the speed of polymer being pressed in depth direction, and η_0 is the viscosity of the polymer. From this equation, we can see that large radial flow distance, small thickness of polymer layer and large viscosity of the polymer requires large imprinting force. Small molecular weight polymer has a low viscosity [23]. The viscosity of a polymer decreases with the increase of heating temperature [24]. A reduction in temperature has to be compensated by corresponding increases in imprinting pressure and time to obtain satisfactory results [25]. The imprinting process may take hours at 140 ℃, while at 200 ℃ it only needs several seconds for PMMA [26].

Generally speaking, smaller features are easier to imprint than larger features. Thomas Hoffmann showed that at 100 bar pressure and 140~150 ℃, 500 nm periodical PMMA lines can be imprinted within 5 min, however, at same pressure and temperature, 100 μm periodical lines cannot be realized unless the temperature rises to 200 ℃ [26]. Thermoplastic nanoimprint lithography is

more suitable for uniform, small and similar sized structures. If the structures are not similar in thermoplastic nanoimprint lithography, the flow speed of the polymer in the mold cavity is different because of the size difference. The filling of the cavity is also not uniform [27]. The dependence of polymer filling on feature dimension and density can be treated as the imprinting proximity effect [28]. Optimization of the pressure, temperature and imprinting time with appropriate polymer material can minimize the proximity effect and achieve uniform filling of mold cavity with dimension from sub-100 nm to millimeter [29].

There are some new polymer materials for thermoplastic nanoimprint lithography nowadays, such as the NXR series [30] and mr-I series [31]. These polymers are engineered to have high resolution, wafer-scale uniformity, fast response and excellent flow, low processing temperature and pressure and strong adhesion to substrates.

Demolding

To achieve high quality structural detail in replicated polymers, demolding is a very critical step. Demolding is the process of separating the mold from the imprinted polymer structure, it is typically performed after cooling down the mold and polymer below the glass transition temperature of the polymer. During this step, the friction drag forces between the polymer material and the mold surface, caused by the roughness of the mold sidewall can lead to structural damage of the replicated polymer. Demolding can also be hampered by a negative trapper angle of the features in the mold, therefore a positive slope of mold sidewall is needed. To address these problems, firstly we should choose a mold material which has low surface energy; secondly mixing a mold release agent with polymer [32] and thirdly coating the surface of the mold with an antistiction layer. Teflon^{TM} or Teflon-like fluorocarbon or fluorosilane release agent are all able to modify the mold surface to make the surface hydrophobic and of low surface energy [27].

4.1.2 UV-cured Nanoimprint

UV-cured Nanoimprint was first proposed in mid-1990s [33]. Fig. 4.3 shows the basic steps of UV-cured Nanoimprint. The process is almost the same as thermoplastic nanoimprint lithography. The key differences are the transparent mold, UV-curable polymer and low imprinting pressure.

Quartz or silica molds with nanoscale surface-relief features are fabricated by e-beam lithography and then used as the molding tool. Recently, Elastomers [34] and plastomers [35] have been used for UV-cured Nanoimprint with sub-100 nm resolution. In UV-cured Nanoimprint, the pressure applied to press the mold is usually less than 1 bar. The solidification of the polymer is done via UV illumination through the transparent mold. People are still pursuing large area imprinting at low cost and high-through-put. In 2010, UV-cured Nanoimprint realized fabricating microlenses in suitable full wafer patterning with different diameters and sag heights [36]. Roll-to-roll UV-cured Nanoimprint realized patterning 700 nm period grating structure created on Polyethylene terephthalate (PET) substrate with a total size of 570 mm (width of 10 mm) [37]. Up to now, roll-to-roll UV-cured Nanoimprint has been used in fabricating flexible electronics, bottom-up transistors, active matrix backplanes for flexible displays, and organic light-emitting devices [38, 39, 40, 41].

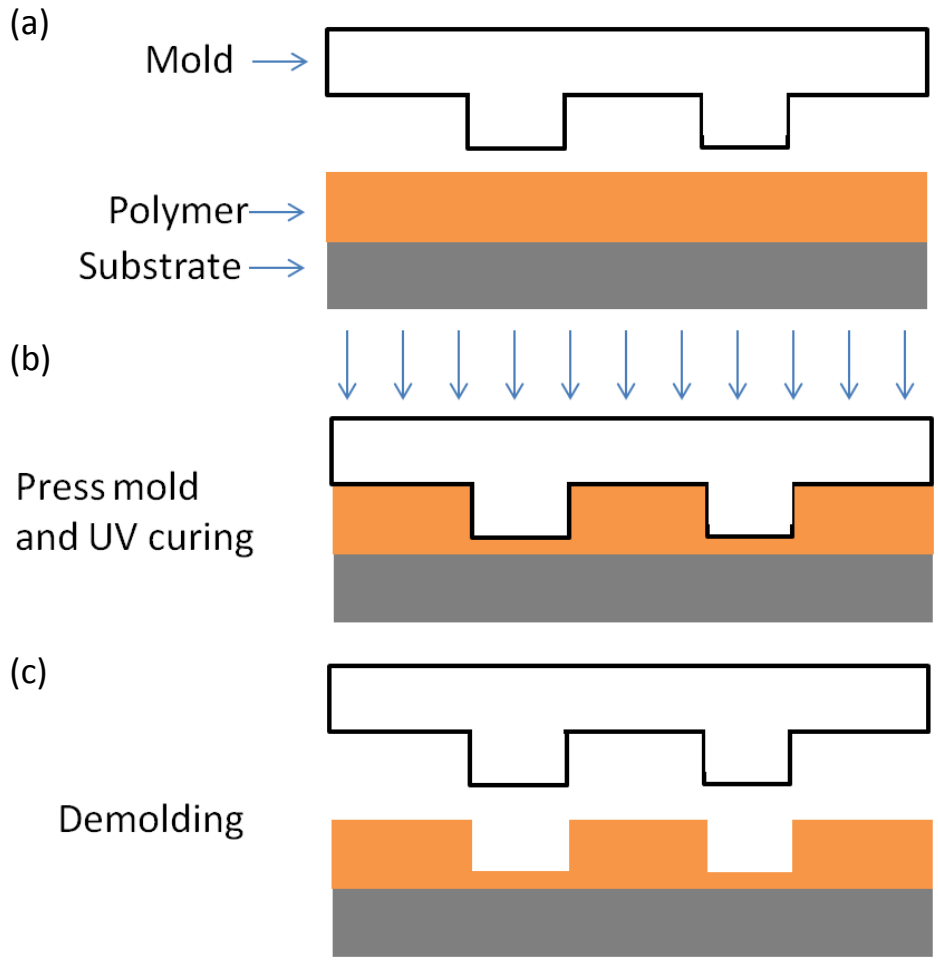

Fig. 4.3 Schematic of UV-cured Nanoimprint: (a) transparent mold, polymer and substrate, (b) UV exposure to cure the polymer, (c) demolding

4.2 Applications of Ni molds fabricated by PBW and electroplating

As mentioned in Chapter 3, Ni molds fabricated with PBW and electroplating have very good quality presenting vertical and smooth sidewalls. A Ni mold featuring 100 nm wide and 2 μm high ridge with very smooth and vertical sidewalls was realized with PBW and electroplating [42]. In addition, the structure was accurately transferred to PMMA via nanoimprinting. In order to expand the applications of PBW in nanoimprinting as well as injection

molding, it is very important to investigate new resist materials which are suitable for the combination of PBW and nanoimprinting as well as injection molding. In this section, I will give some imprinted results based on the Ni molds fabricated with new resist materials. All the experiments were done with a commercial nanoimprinter (Obducat Technologies AB, NIL-2-Pl 2.5 in. nanoimprinter).

4.2.1 Imprinting results of Ni mold fabricated by AR-P 3250

In Chapter 3, Ni molds fabricated with AR-P 3250 were introduced. The structures in the Ni molds show vertical and smooth sidewalls which is very important in thermoplastic nanoimprint lithography [43]. Here we show NIL results with these molds on spin coated PMMA layers. Fig. 4.4 shows the SEM image of the structures in a Ni mold (4 μm deep) fabricated by AR-P 3250 resist and electroplating. Details of fabrication process were introduced in Chapter 3. As can be seen, the resist was completely removed.

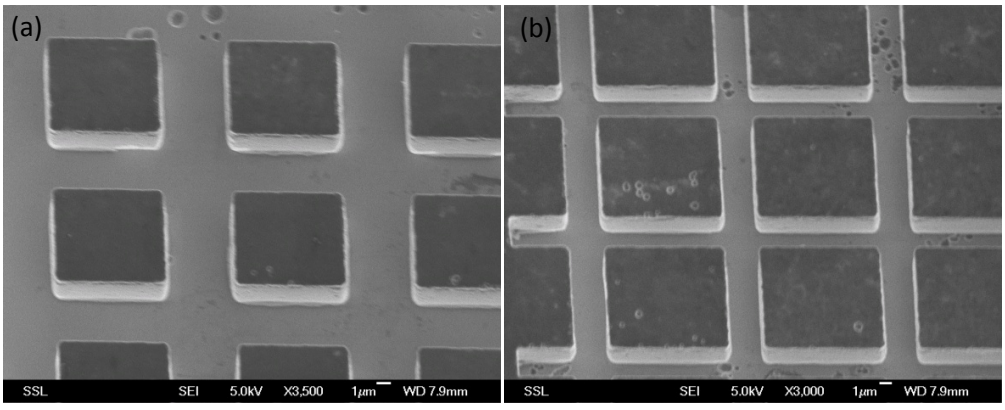

Fig. 4.4 Grooves in Ni mold (a) 5 μm wide (b) 2.5 μm wide. The height of the structure is 4 μm

Next a 5 μm thick PMMA 950 A11 was spin coated at 1000 rpm for 30 s on a Si wafer followed by a pre baked at 180℃ for 90 s to completely remove any

solvent. Then the spin coated PMMA was imprinted by the Ni mold in Obducat Technologies AB, NIL-2-Pl 2.5 in. nanoimprinter. Four samples were tested in this experiment. All the samples were first under a pressure at 20 bar and temperature of 100 ℃ for 20 s, followed by next step where the differences are, then pressure was released right after the temperature decreased below 80 ℃. Fig 4.5 shows the imprinted PMMA lines of the four samples.

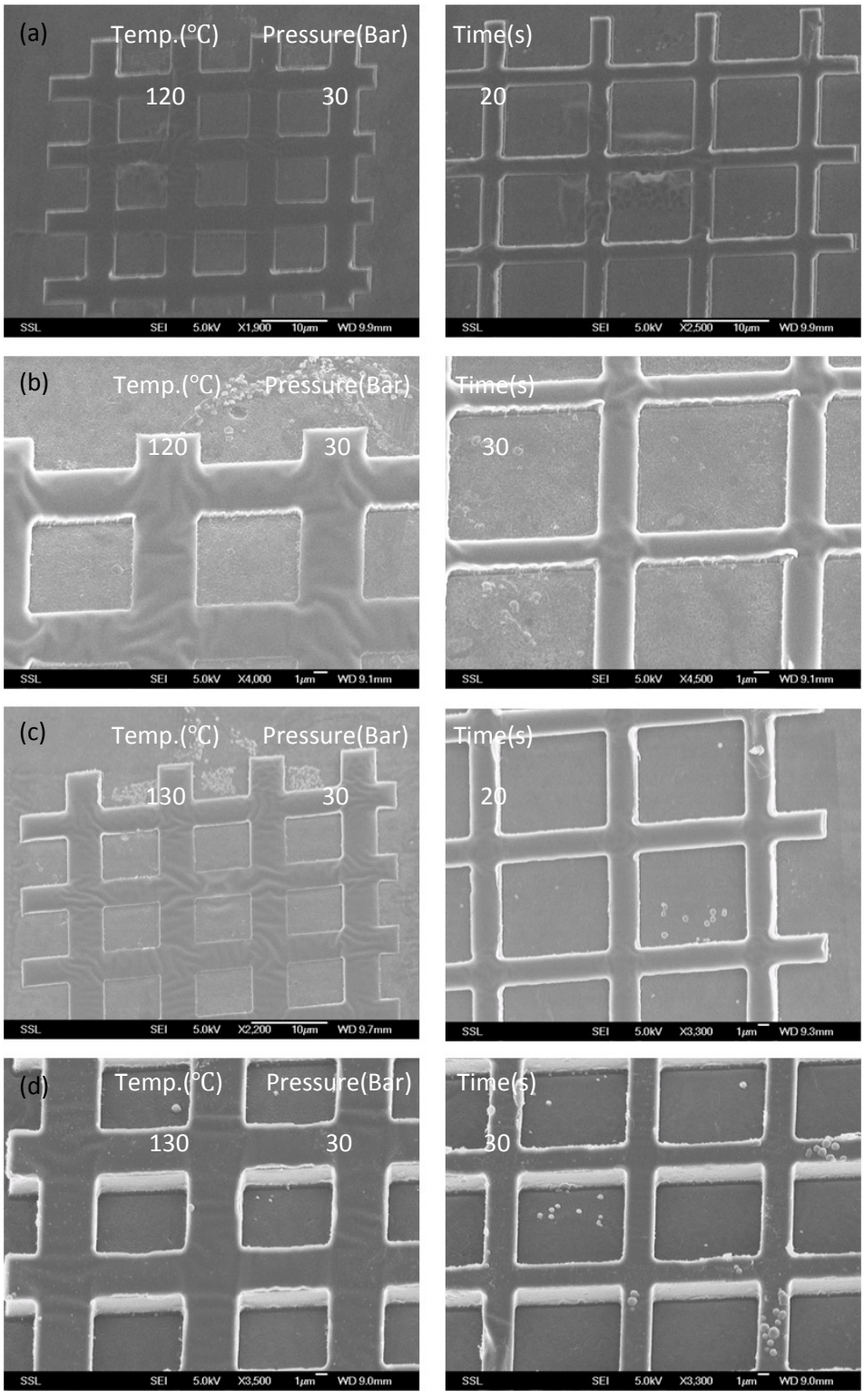

Fig. 4.5 SEM image of the nanoimprinted PMMA structures with width of 5 μm and 2.5 μm: samples (a)-(d)

From Fig. 4.5a and b, we can see that at temperature of 120 ℃ and pressure of 30 bar, a longer time of imprinting will help the polymer flow into the grooves and completely fill them. The structures in Fig. 4.5b are higher than the structures in Fig. 4.5a. If we keep the temperature at 120 ℃, the structures don't improve under even higher pressure or even longer imprinting time. For Fig. 4.5c and d, the temperature was increased to 130 ℃ with a pressure of 30 bar and imprinted for 20 s and 30 s respectively. As can be seen, the structures in Fig. 4.5d were accurately replicated from the Ni mold. PMMA fully filled the Ni grooves, while in Fig. 4.5c the PMMA practically didn't penetrate the grooves. This means at an optimized temperature, longer imprinting is needed to fill the groove completely. The optimized parameters for the 5 μm and 2.5 μm wide lines are: 20s at 100 ℃ and 20 bar, followed by 30 s at 130 ℃ and 30 bar. The pressure was also released after cooling just below 80 ℃.

Nonetheless, there is nanoimprinting proximity effect---small feature can be imprinted quickly while large cavities may not get filled up completely. With the parameters shown in Fig. 4.5d, smaller structures 500 nm wide and 4 μm high ridges sink into the base because of the high temperature and longer time of imprinting as shown in Fig. 4.6b. PMMA cannot be replicated with this parameter with the Ni mold shown in Fig. 4.6a. Fig. 4.6c shows another imprinted 500 nm wide ridge in spin coated PMMA. The imprinting parameters are 120 ℃ and 30 bar for 30 s. As can be seen from the figure, the 500 nm wide ridge is accurately replicated.

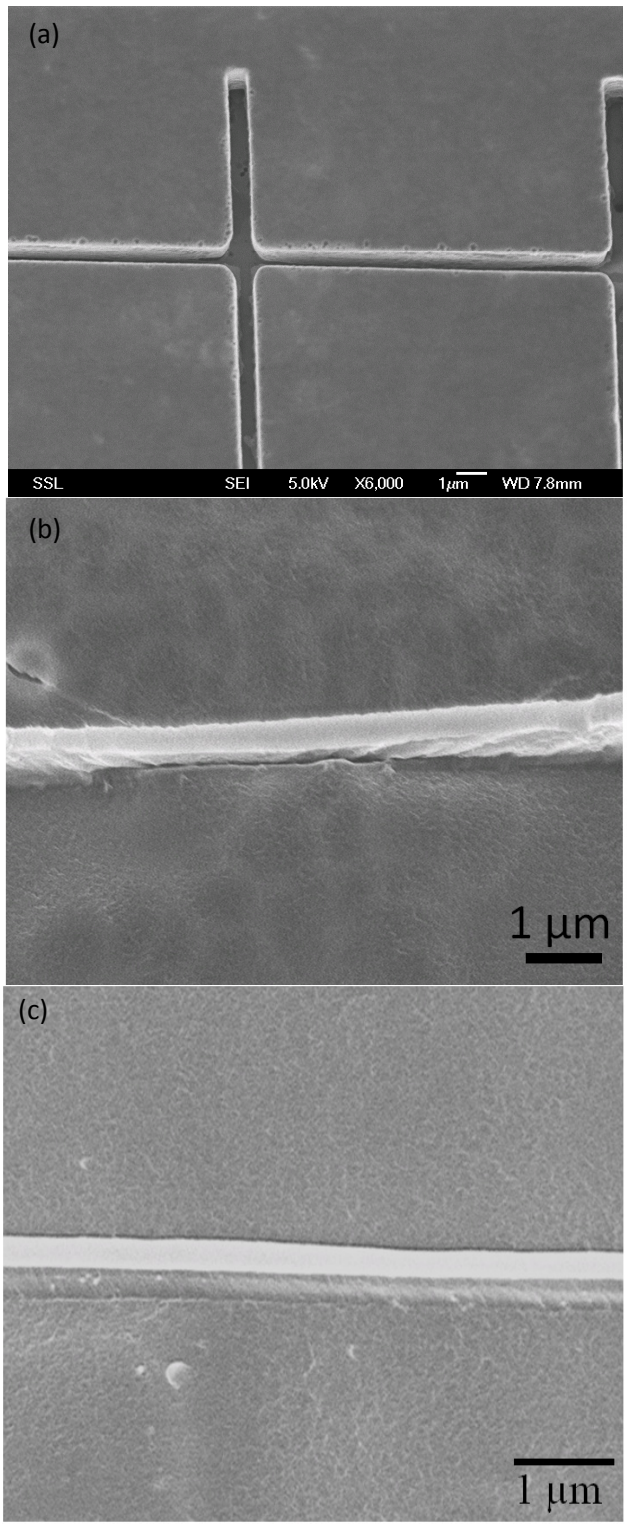

Fig. 4.6 (a) Ni mold with 500 nm wide and 4 μm deep groove, (b) PMMA ridge imprinted at 130 ℃ and 30 bar for 30 s, (c) PMMA ridge imprinted at 120 ℃ and 30 bar for 30 s

4.2.2 Imprinting results of Ni mold fabricated by mixture resist (AR-P 3250: AR 300-12=1:3)

The Ni mold with a 120 nm wide and 280 nm deep groove was used in the experiment. The imprinting cycle consists of 20 s at 100 ℃ and 20 Bar, followed by 15 s at 120 ℃ and 30 Bar. The pressure was released after cooling just below 80 ℃. Fig. 4.7 shows the PMMA ridge imprinted in a 5 μm thick PMMA layer spin coated at 1000 rpm for 30 s. The replicated pattern featuring 120 nm wide and 280 nm high wall was accurately transferred from the Ni mold to the 5 μm thick spin coated PMMA.

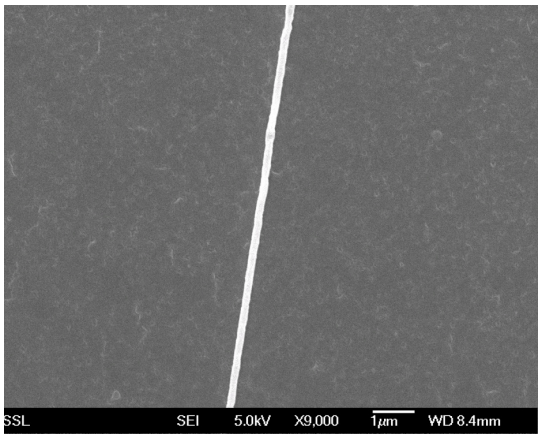

Fig. 4.7 SEM image of 120 nm wide and 280 nm high line imprinted on spincoated PMMA

4.3 Microfluidic particle separation device fabrication and test

4.3.1 Particle separation design

In order to realize low cost and high-through-put microfluidic device fabrication, PMMA bonding and nanoimprinting were combined. Fig. 4.8 shows the microfluidic design. This is a design from a collaborative research project "Development of Novel Methods of Fabricating Metallic Injection

Molds for Lab on Chip Biomedical Sample Preparation and Cell Analysis Applications" between the Center of Ion Beam Applications (CIBA) and the Singapore Institute of Manufacturing Technology (SIMTech). The chip is used to separate particles of different sizes. Micro pillar arrays are designed on biochips inside micro channels to act as filtration structures to filtrate out particles in biomedical fluidic sample analysis.

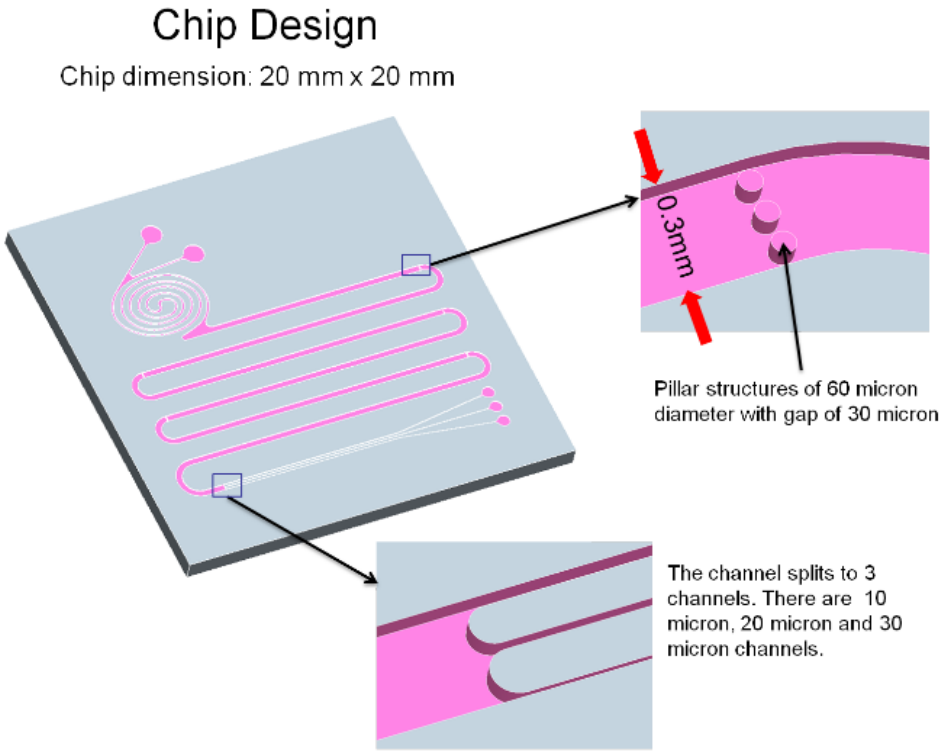

Fig. 4.8 Design showing the dimensions of the microfluidic device

As can be seen from the figure, the large channel is designed to be 300 µm, and the split channels are 10 µm, 20 µm and 30 µm wide. In the 300 µm wide channel, there are 5 sets of 3 pillars. The pillars have a 60 µm diameter with a spacing of 30 µm.

4.3.2 Ni mold fabrication for particle separation device

Fig. 4.9 shows the procedures of fabricating the microfluidic device. First, Si wafer was coated with Cr and Au as seed layer for electroplating. Then, AR-P 3250 was spin coated at 500 rpm for 2 min, and 800 rpm for 5 sec to reduce

edge beads. The sample was baked at 95 ℃ for 13 min to remove any solvent. This yielded a layer of 11 μm. The pillars, a critical part of the particle separation design, were fabricated by PBW since PBW enables vertical and smooth sidewalls.

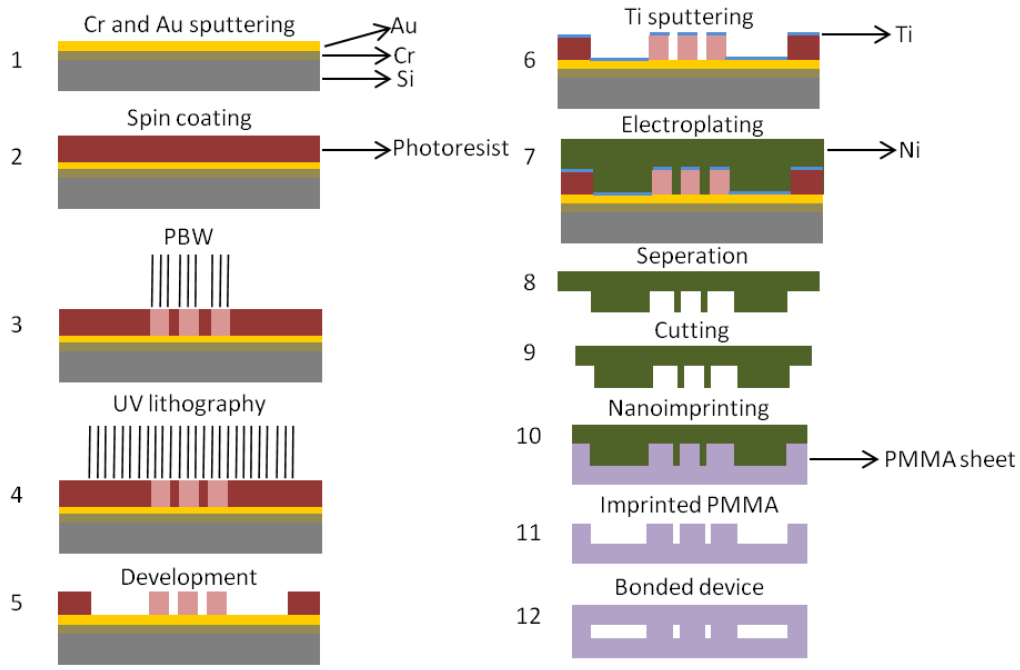

Fig. 4.9 Schematic procedures of microfluidic device fabrication

2 MeV protons were focused to 300 nm × 300 nm to expose AR-P 3250 at a dose of 50 nC/mm^2. After PBW, the pillars were visible due to the color difference between the exposed and unexposed area due to different reflectivity. This facilitates an aligned exposure so that the large features can be fabricated via masked UV lithography (30 min 365 nm 100 Watt) accurately positioned around the proton beam fabricated pillars, following the same procedure as in Fig. 2.19d. After PBW and UV lithography, the sample was developed in AR 300-26 for 3 min, rinsed in DI water for 2 min and air dried. Optical photographs of different parts of the fabricated resist structure are shown in Fig. 4.10. Fig.4.11a shows an SEM image of the sidewall of one of the ARP 3250 resist pillars (10 μm tall). As can be seen, the sidewall is vertical and smooth.

After development, the sample was coated with a 6 nm Ti layer as seed layer for electroplating using filted cathodic arc vacuum deposition method. Electroplating was performed in our plating machine at a rate of 260.4 A/dm^2 for 200 min reaching a thickness of 100 µm, followed by 520.8 A/dm^2 for 40 hours, yielding a total thickness of 2.5 mm. After separating the Ni mold and Si wafer, the Ni mold was cut into 21 mm × 23 mm × 2 mm (details were introduced in Chapter 3). Fig. 4.11b shows the Ni mold featuring a vertical and smooth sidewall.

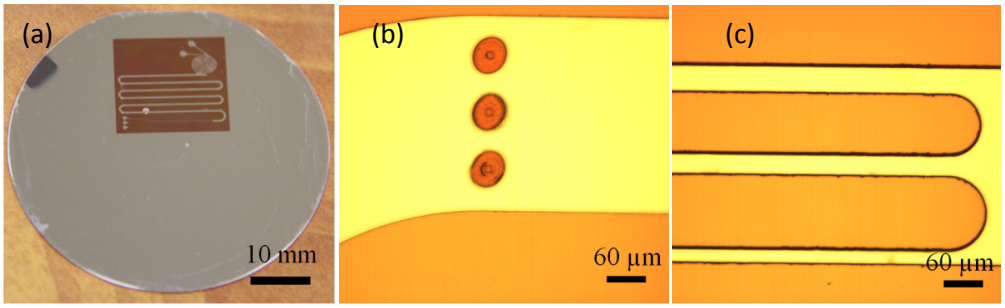

Fig. 4.10 AR-P 3250 resist structures (a) The whole structure in Si wafer as exposed via UV and PBW (b) Pillars in the large channel fabricated by PBW (c) The collection channels fabricated by UV lithography

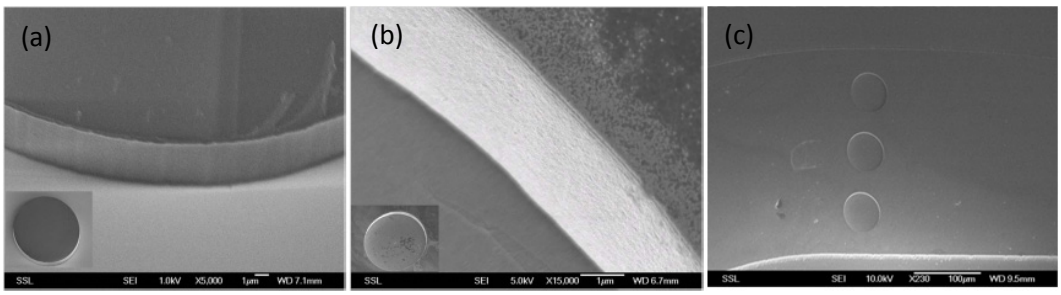

Fig. 4.11 (a) sidewall of 10 µm AR-P resist structure (b) sidewall of 10 µm hole in Ni mold (Height: 10 µm) (c)three holes in a large channel(depth: 11 µm; this mold was used in nanoimprinter. this sample was obtained from 11 µm tall AR-P pillars)

4.3.3 NIL of the microfluidic device

The Ni mold was used in our nanoimprinter to fabricate microfluidic channels by imprinting on an 850 μm PMMA sheet. The imprinting cycle consists of 20 s at 100 ℃ and 20 bar, followed by 240 s at 120℃ and 30 Bar. The pressure was released after cooling just below 80℃.

The depth of the hole is 11 μm with a diameter of 60 μm. Fig. 4.12 shows the imprinted results. As can be seen from the figure, the pillars have very vertical and smooth sidewall which is almost comparable with the resist structures. This mold was used for more than 100 times, and the results were similar with initial imprinted results.

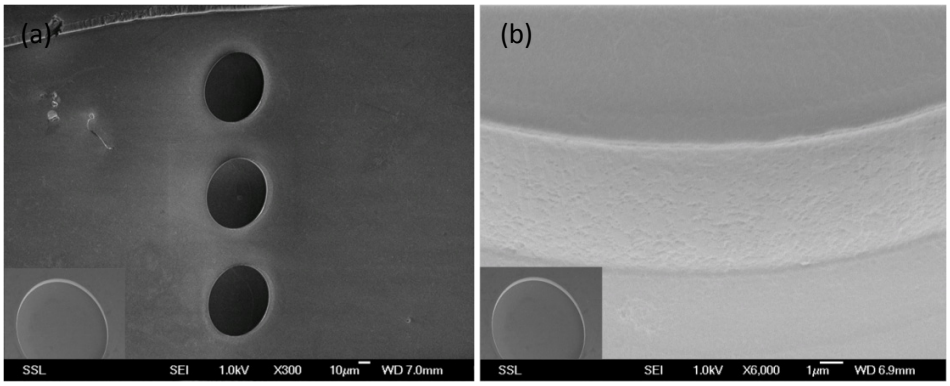

Fig. 4.12 (a) three pillars in a large channel imprinted in PMMA sheet, (b) sidewall of the 11 μm high pillar

4.3.4 Thermal bonding of the microfluidic device

After imprinted PMMA structures were realized, the samples were bonded to a thin PMMA sheet to form a lab on chip device. Two different PMMA resist layers were spincoated on kapton. Kapton is a polyimide film developed by DuPont that can remain stable in a wide range of temperatures, from -237 to +400 ℃ [44]. One layer was spin coated at 2000 rpm for 30 s to yield a thickness of 3 μm, the other was spin coated at 2000 rpm for 30 s for three times to yield a thickness of about 9 μm. Next the imprinted sample was

rinsed with IPA for 2 min and DI water for 5 min, and air dried; then the spin coated PMMA on kapton was placed on the nanoimprinted sample. The whole stack was put on a hot plate at 110 ℃ and a pressure of 1.2 bar was applied for 2 hours (see Fig. 4.13).

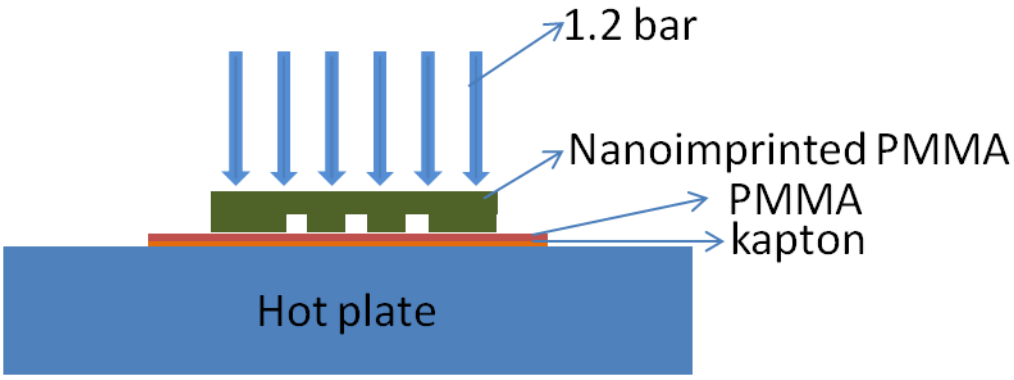

Fig. 4.13 The configuration of PMMA bonding at 110 ℃ and 1.2 bar for 2 hours

After bonding, the sample was cooled down to room temperature. Next the kapton was peeled off, leaving the layer of spin coated PMMA on the nanoimprinted PMMA sheet. After bonding the 3 μm thick PMMA fell in the large channel due to low young's modulus of PMMA. The other sample with 9 μm thick PMMA was bonded strong enough to span 300um. This sample was tested with fluidics.

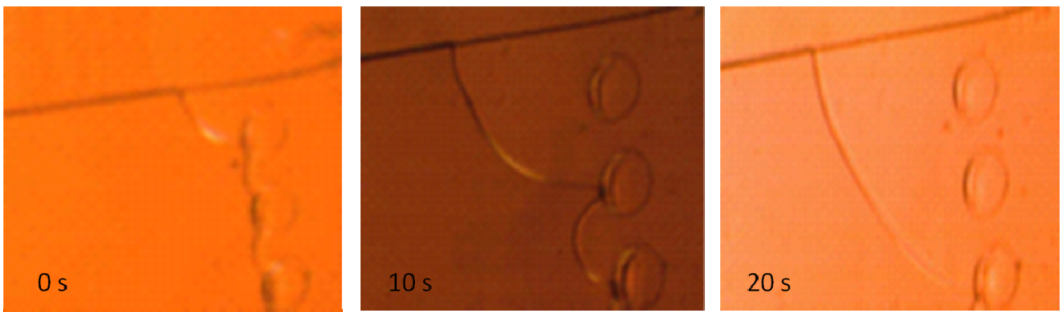

Fig. 4.14 Liquid flows in the channel passing through the pillars while filling the chip

Fig. 4.14 shows the optical image of liquid flowing in the channel passing through the pillars during the filling process. There is no leakage in the

channel which demonstrates that this is a well bonded PMMA microfluidic device. The bonded PMMA layer can be even thicker to get better bonding results. This bonding process is easy to operate after optimizing the process.

4.4 Summary

In this chapter, Nanoimprinting technology and its recent development are introduced. There are some research reports about high aspect ratio and high resolution Ni molds. However, most of the reports only possess one advantage, i.e., either high aspect ratio or high resolution. There are few achievements which have both of the advantages. Our technique makes up this gap in Ni mold fabrication. The technique combined with our Ni molds was described. Remarkable achievements were achieved. In our research, 500 nm wide and 4 μm high structures were replicated in polymer PMMA. Structures down to 120 nm wide and 280 nm high line was also well achieved in nanoimprinted PMMA. This gives an easier way to fabricated high aspect ratio and high resolution structures which can be used in many areas.

At the end of this chapter, a microfluidic cell separating device was fabricated by our technique. The device was fabricated with optical lithography, PBW, electroplating and nanoimprinting. It was found the Ni mold used gave same good result after 100 times' nanoimprinting. This technique gives a very promising future for mass producing microfluidic devices.

References

[1] Chou, S.Y., P.R. Krauss, and P.J. Renstrom, *Imprint of sub-25 nm vias and trenches in polymers*. Appl. Phys. Lett., 67(21): pp.3114-3116, 1995

[2] Chou, S.Y., *Nanoimprint lithography*, U.S. Patent No. 5772905, 1998

[3] Chou, S.Y., P. Krauss, W. Zhang, L. Guo, and L. Zhuang, *Sub-10 nm imprint lithography and applications*, J. Vac. Sci. Technol. B, 15, 1997

[4] J. Wang, X. Sun, L. Chen, and S. Y. Chou, *Direct nanoimprint of submicro organic light-emitting structures*, Appl. Phys. Lett., 75 18:2767-2769, 1999

[5] A. Lebib, Y. Chen, J.Bourneix, F. Carcenac, E. Cambril, L. Couraud, and H. Launois, *Nanoimprint lithography for a large area pattern replication*, Microelectronic Engineering, 46:319-322, 1999

[6] International Technology Roadmap for Semiconductor. [cited; Available from http://www.itrs.net/]

[7] Z.H. Yu, S.J. Schablitsky, S. Y. Chou, *Nanoscale gas metal-semiconductor-metal photodetectors fabricated using nanoimprint lithography*, Appl. Phys, Lett., 74(16): 2381-2383, 1999.

[8] Chung Yen Chao, Jay Guo, *Polymer microring resonators fabricated by nanoimprint technique*, J. Vac. Sci. Technol. B, 20(6): 2862-2866, 2002

[9] C. Kim, M. Stein, S,R, Forrest, *Nanolithography based on pattered metal transfer and its application to organic electronic devices*, Appl. Phys. Lett., 80:4051-4053, 2002

[10] Zhan Liu, David G Bucknall, Mark G Allen, *Inclined nanoimprinting lithography-based 3D nanofabrication*, J. Micromech. Microeng. 21, 065036, 2011

[11] H. Kobayashi, S. Kishimoto, K. Suzuki, H. Iyama, S. Nakatsuka,K. Taniguchi, T. Sato, T. Watanabe, *25 nm pitch master and replica mold fabrication for nanoimprinting lithography for 1 Tbit/inch^2 bit patterned media*, Proc. Of SPIE Vol. 8323 83231V-1, 2012

[12] H. Tan, L. Kong, M. Li, C. Steere, L. Koecher, *Current status of nanonex nanoimprint solutions*, Proc. SPIE, 2004

[13] B. Heidari, I. Maximov, E. L. Sarwe, L. Montelius, *Large scale nanolithography using nanoimprint lithography*, J. Vac. Sci. Technol. B, 17(6):2961-2964, 1999

[14] Sunggook Park, Zhichao Song, Lance Brumfield, *Demolding temperature in thermal nanoimprint lithography*, Appl Phys A, 97: 395-402, 2009

[15] Fukuda M, Chiba T, Ishikawa M, Itoh K, Kurihara M, Hoga M, *Si-mold fabrication for patterned media using high-resolution chemically amplified resist*, The international Society for Optical Engineering, V 7379, 2009

[16] Tada K, Yasuda M, Kimoto Y, Kawata H, Hirai Y, *Molecular dynamics study of yield stress of Si mold for nanoimprint lithography*, Japanese Journal of Applied Physics, part 1, V 47, 2008

[17] Ji Hye Lee, Kyoung Seob Kim, Byound Kyu Lee, Nam-Hoon Kim, Yonghan Roh, *Performance and characteristics of SiO_2 imprint mould fabricated by liquid-phase deposition*, 44(4-5):520, 2008

[18] Liu Zewen, Zhang Tianruo, Liu Litian, Li Zhijian, *Realization of silicon nitride template for nanoimprint: A first result, Diffusion and Defect Data Pt.B*: Solid State Phenomena, V 121-123, 2007

[19] Tomi Haatainen, Paivi Majander, Tommi Riekkinen, Jouni Ahopelto, *Nickel mold fabrication using step & mold imprint lithography*, Microelectronic Engineering 83 948-950, 2006

[20] Haffner. M, et al, *Simple high resolution nanimprint-lithography*, Microelectron. Eng., 84:937-939, 2007

[21] Y. Hirai, *Polymer science in nanoimprint lithography*, J. Photopolym. Sci. Technol. 18, 551, 2005

[22] Bird.R. B., R. C. Amstrong, O.Hassager, *Fluid mechanics, in dynamics of polymeric liquids*, John Wiley & Sons, 1997

[23] Schift H, Heyderman L. Nanorheology, *Squeeze flow in hot embossing of thin films* // Torres C M S. Alternative Lithography, Kluwer Academic, 2003

[24] Halary J L, et al, *Viscoelastic properties of styrene-co-methyl methacrylate random copolymers*, J. Polym. Sci. B: Polym. Phys., 29(8): 933, 1991

[25] H.C. Scheer, N. Bogdanski, M. Wissen, T. Konishi, Y. Hirai, *Polymer time constants during low temperature nanoimprint lithography*, J. Vac. Sci. Technol. B, 23, 2963, 2005

[26] Hoffmann T, *Viscoelastic properties of polymers: relevance for hot embossing lithography*, Torres C M S. Alternative Lithography. Kluwer Academic, 2003

[27] Scheer H C, et al, *Problems of the nanoimprinting technique for nanometer scale pattern definition*, J. Vac. Sci. Technol., B16 (6): 3917, 1998

[28] Landis S et al, *Mold design effect on 100 nm feature size for 8 inch nanoimprint lithography*, Nanotechnology, 17: 2701-2709, 2006

[29] Cui B., T. Veres, *Pattern replication of 100 nm to millimeter-scale features by thermal nanoimprint lithography*, Microelectron. Eng., 83: 902-905, 2006

[30] Nanonex Corp. [http://www.nanonex.com]

[31] Microresist GmbH. [http://www.microresist.de/]

[32] Chou S.Y., P.R. Krauss, P.J. Renstrom, *Nanoimprint lithography*, J. Vac. Sci. Technol., B14(6):4129, 1996

[33] Haisma J, et al, *Mold-assisted nanolithography: a process for reliable pattern replication*, J. Vac. Sci. Technol., B 14:4124, 1996

[34] N. Koo et al., *Improved mold fabrication for the definition of high quality nanopatterns by soft UV-nanoimprint lithography using diluted PDMS material*, Microelectron. Eng. V 84, p904–908, 2007

[35] D.Y. Khang, H.H. Lee, *Sub-100 nm patterning with an amorphous fluoropolymer mold*, Langmuir 20, p2445–2448, 2004

[36] H. Schmitt, M. Rommel, A.J. Bauer, L. Frey, A. Bich, M. Eisner, R. Voelkel, M. Hornung, *Full wafer microlens replication by UV imprint lithography*, Microelectronic Engineering 87, 2010

[37] Se Hyun Ahn, L. Jay Guo, *High-speed Roll-to-roll Nnaoimprint Lithography on Flexible Substrate and Mold-separation Analysis*, Proc. Of SPIE Vol. 7205, 2009

[38] P. Maury, D. Turkenburg, N. Stroeks, P. Giesen, I. Barbu, E. Meinders, A. van Bremen, N. Iosad, R. van der Werf, H. Onvlee, *Roll-to-roll UV imprint lithography for flexible electronics*, Microelectronic Engineering, V 88, 2011

[39] P. Maury, N. Stroeks, M. Wijnen, R. Tacken, R. van der Werf, *Roll-to-roll UV imprint for Bottom-up Transistor Fabrication*, Journal of Photopolymer Science and Technology, V 24, 2011

[40] A. Marcia, Jeans Albert, Braymen Steve, Elder Richard E, Garcia Robert A, De La Fuente Vornbrock Alejandro, H. Jason, H. Edward, J. Warren, J. Mehrban, J. Frank, J. Kelly, Kim Han-Jun, K. Ohseung, L. Dan, M. John, M. Ping, P. Craig, S. Mark, S. Dan, T. Carl P, T. Steven, Zhao Lihua, *Planarization coating for polimide substrates used in roll-to-roll fabrication of active matrix backplanes for flexible displays*, HP Laboratories Technical Report, n 23, 2012

[41] Shen Su, Zhou Fang, Pu Donglin, Wei Guojun, Zhou Yun, *Microlens array film fabricated by UV roll-to-roll nanoimprinting for enhancing out-coupling efficiency of organic light-emitting devices*, International Conference on Manipulation, Manufacturing and Measurement on the nanoscale, 3M-NANO, 2012

[42] K. Ansari, J. A. van Kan, A. A. Bettiol, F. Watt, *Fabrication of high aspect ratio 100 nm metallic molds for nanoimprinting lithography using proton beam writing*, Appl. Phys. Lett. V 85, 2004

[43] C.H. Yao, C.H. Chang, C.W. Hsieh, C.K. Sung, *Effects of mold shape and sidewall roughness on nanoimprint by molecular dynamics simulation*, Microelectronic Engineering, 87: 864-868, 2010

[44] Navick, X.-F., Carty, M., Chapellier, M., Chardin, G., Goldbach, C., Granelli, R., Hervé, S., Karolak, M. et al., *Fabrication of ultra-low radioactivity detector holders for Edelweiss-II*, NIM A 520: 189–192, 2004

Chapter 5 Application of proton beam fabricated Ni molds in Injection Molding

In this chapter, I will first give an introduction to injection molding, followed by initial injection molding results on Ni molds fabricated via PBW and electroplating.

5.1 Introduction to Injection Molding

Injection molding is a traditional manufacturing process for producing parts by injecting thermoplastic and thermosetting plastic or other materials like metals and glasses into a mold. Fig. 5.1 shows a sketch of an injection molding machine [1].

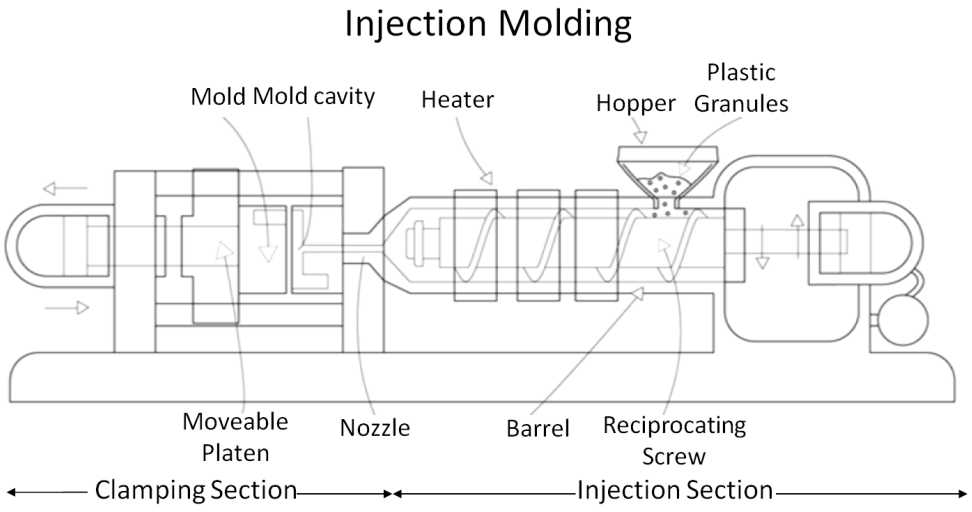

Fig. 5.1 Sketch of injection molding machine

Basically, there are two sections in the machine: injection and clamping section. In the injection section, there is a hopper to hold the plastic granules,

reciprocating screw to move the plastic granules towards the mold, via a barrel surrounded by a heater to melt the plastic granules. Finally the plastic leaves the injector via a nozzle connected to a mold cavity. In the clamping section, there is a mold cavity where the molten plastic is injected into a mold. A moveable platen can lock or release the mold [2]. Fig. 5.2 shows the injection molding process [3].

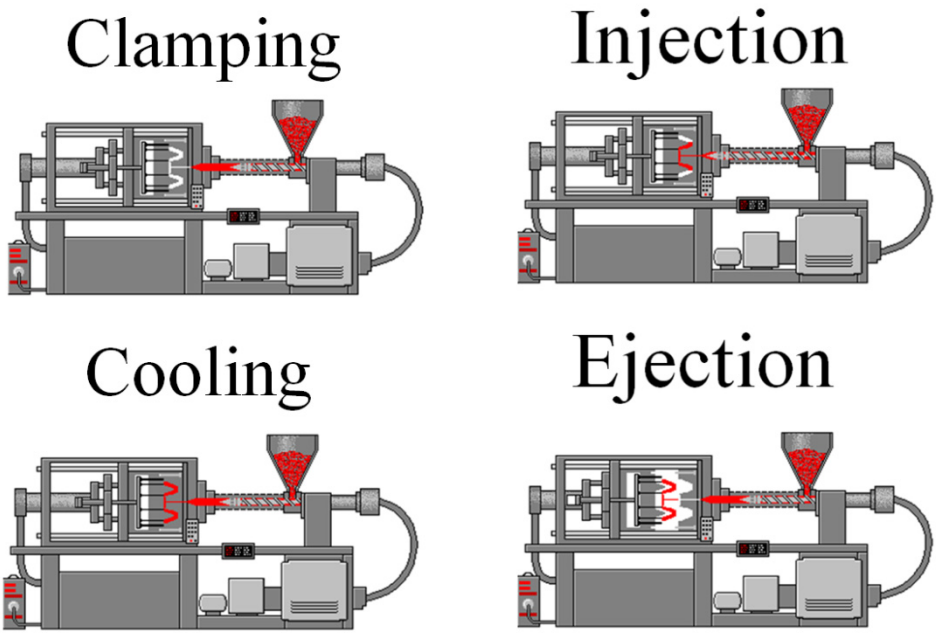

Fig. 5.2 The process of injection molding

The process of injection molding is very short, typically only takes about 2 s to 2 min. There are four stages in the process:

1. Clamping: the mold must first be bolted into the clamping section. The clamping section is closed and the mold is firmly pressed in place.
2. Injection: the plastic granules are fed into the barrel of the injection molding machine by the hopper. In the barrel, the reciprocating screw drives the plastic granules forward, mixes and reduces the required heating time by mechanically shearing the plastic, adding a significant amount of frictional heat to the plastic. The plastic is collected at the

nozzle, in front of the screw. Then the molten plastic is forced into the mold cavity at a high pressure and velocity, and fills the cavity taking the shape of mold.

3. Cooling: the plastic begins to cool as soon as it is released into the cavity. As the plastic cools, it solidifies. During this stage, the reciprocating screw will rotate and bring more plastic granules for the next part.
4. Ejection--- The mold can be opened when it has cooled down enough. Next the injected plastic is ejected. Once the part is ejected, the mold can be clamped shut for the next shot to be injected.

In injection molding, the maximum clamp force a machine can exert is expressed in tonnage. This force keeps the mold closed during the injection process. Injection molding machines can provide a force from less than 5 tons to over 9,000 tons. The total clamp force needed is determined by the projected area of the part being molded. Usually 4 or 5 tons/Inch^2 can be used for most products. If the plastic material is very viscous, it will require more injection pressure to fill the mold, thus more clamp force to hold the mold closed [4]. Larger parts require higher clamping force [5].

There are many types of materials that can be used in injection molding including all thermoplastic, some thermosets, and some elastomers. The most common used materials are listed below [6].

- **ABS** – widely used.

  Acrylonitrile Butadiene Styrene — known widely as ABS — is among the most popular and versatile of the resins in the styrene family (which includes polystyrene). Its availability, strength, and limited shrinkage all help make it widely used as the default choice for most plastic products.

- **Polypropylene (PP)** – strong and bendable.

  Polypropylene is a thermoplastic that, while not as clear or cheap as polycarbonate, is safe for reuseable containers and laboratory tools. It

has particular resistance to fatigue which makes it ideal for living hinge applications.

- **Polyethylene** – even more bendable.

  Also known as PE with variants LDPE, and HDPE, polyethylene is one of the most common thermoplastics and is used in film-bags, poly-bags, tubing, bearings, toys and buckets among other things.

- **High impact polystyrene (HIPS)** – very versatile.

  A very cheap and versatile thermoplastic, polystyrene's rigidity and limited elasticity has caused it to be supplanted with ABS in most applications, but it remains a very good choice for some applications.

- **Vinyl | Flexible PVC** – inexpensive material for soft, flexible parts

  A durable and flexible material, vinyl is widely used for everything from fencing to containers to upholstery. It is tough and resistant to tearing, but can be soft and have trouble holding a rigid shape.

- **Nylon** – very strong but more expensive than HIPS or ABS.

  Being resistant to wear, nylon is used for mechanical parts such as bearings and other low- to medium-stress components.

- **Polycarbonate (PC) | Lexan** – stronger and more rigid than Nylon.

  Polycarbonate is particularly useful in clear applications such as, lenses, and light covers. Some forms are used for single use food containers and water bottles, but the material is not considered food-safe for reused or washed containers.

- **TPE | Synthetic Rubber** – a.k.a. Sarlink & Santoprene

  Thermoplastic elastomers (TPEs) are a viable injection molded substituted for natural rubbers. They offer a range of stiffness and resistance to abrasion which makes them practical for bushings and seals among other uses.

- **Acrylic (PMMA)** – very clear, but expensive.

  Useful as a replacement for glass, acrylic is very versatile and, although somewhat brittle, can be modified for greater strength.

Different materials have different applications because of their different properties, such as density, melting temperature, glass transition temperature, young's modulus, tensile strength, compressive strength, and hardness.

Researchers have worked with injection molding to achieve small structures for many years. It was found that features with high aspect ratio were difficult to form routinely and the ultimate resolution of injection molding is limited largely by the quality of the mold. In 1998, D. Macintyre et al. produced feature sizes of less than 100 nm and 4 cm long gratings with periods down to 1 μm [7]. In 2002, 200 nm wide nano-features with an aspect ratio of 1:1 were replicated in injection molding [8]. However, injection molding results of polymer micro- and sub-micron structures whose aspect ratios exceed two are hard to obtain with the injection molding equipment and techniques for polymers [8, 9] for various reasons [10]. In 2005, A. Liou et al. fabricated features down to 200 nm with aspect ratio more than 5 in PMMA using injection molding with very high pressure and mold temperature [11]. In 2012, structures down to 40 nm wide and 107 nm high were replicated in injection molding using Ni mold [12]. It was found that increase of mold temperature lead to more fill in the mold cavity. However, it is a pity that no SEM figures were reported.

In our research, Ni molds fabricated with PBW and electroplating are used in injection molding. In the next section, I will give the details of our experiments.

5.2 Ni molds application in Injection Molding

As I introduced in Chapter 3, we have the ability to fabricate high quality Ni molds using different kinds of resists in PBW followed by electroplating. These molds have been used in thermal nanoimprinting and have shown good results. Some of the molds were also tested in injection molding.

5.2.1 Battenfeld Microsystem 50

The injection molding machine we used is a Battenfeld Microsystem 50 with a maximum clamp force of 50 kN.

Fig. 5.3 shows an image of the Battenfeld injection molding machine. Fig. 5.4 shows a schematic drawing of the micro molding system.

Fig. 5.3 50 kN micro injection molding machine from Battenfeld

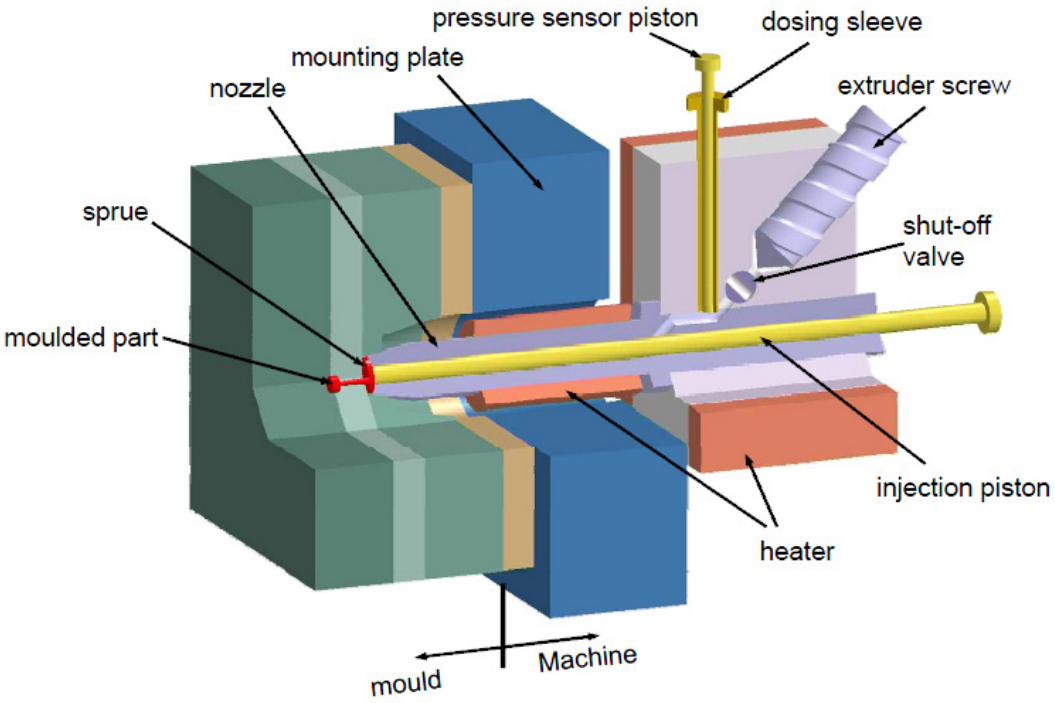

Fig. 5.4 Schematic drawing of the injection molding machine

The mold and cavity area consists two parts---the stationary and the moving half as shown in Fig. 5.5. Every half has two heating slots and a thermo couple slot to control the mold temperature. Details of the design are shown in Fig. 5.6. The stationary half was designed to carry a retainer for a Ni mold. The insert retainer consists of a nozzle hole and an insert holder designed to hold the Ni mold with the dimensions of 21×23×2 mm^3. The mold is clamped with two metal bars and an interchangeable fill plate allowing the fabrication of different structures using different molds. The nozzle of the injection molding machine is in line with the nozzle hole, and this results in a short injection distance, keeping injection pressure and injection speed high and temperature drop low. The two channels at the bottom of the Moving Half are for air release to avoid any air bubbles in the product. After mold opening the replicated part sticks to the Moving Half and is finally ejected by the moving ejector pin and ejector block forward.

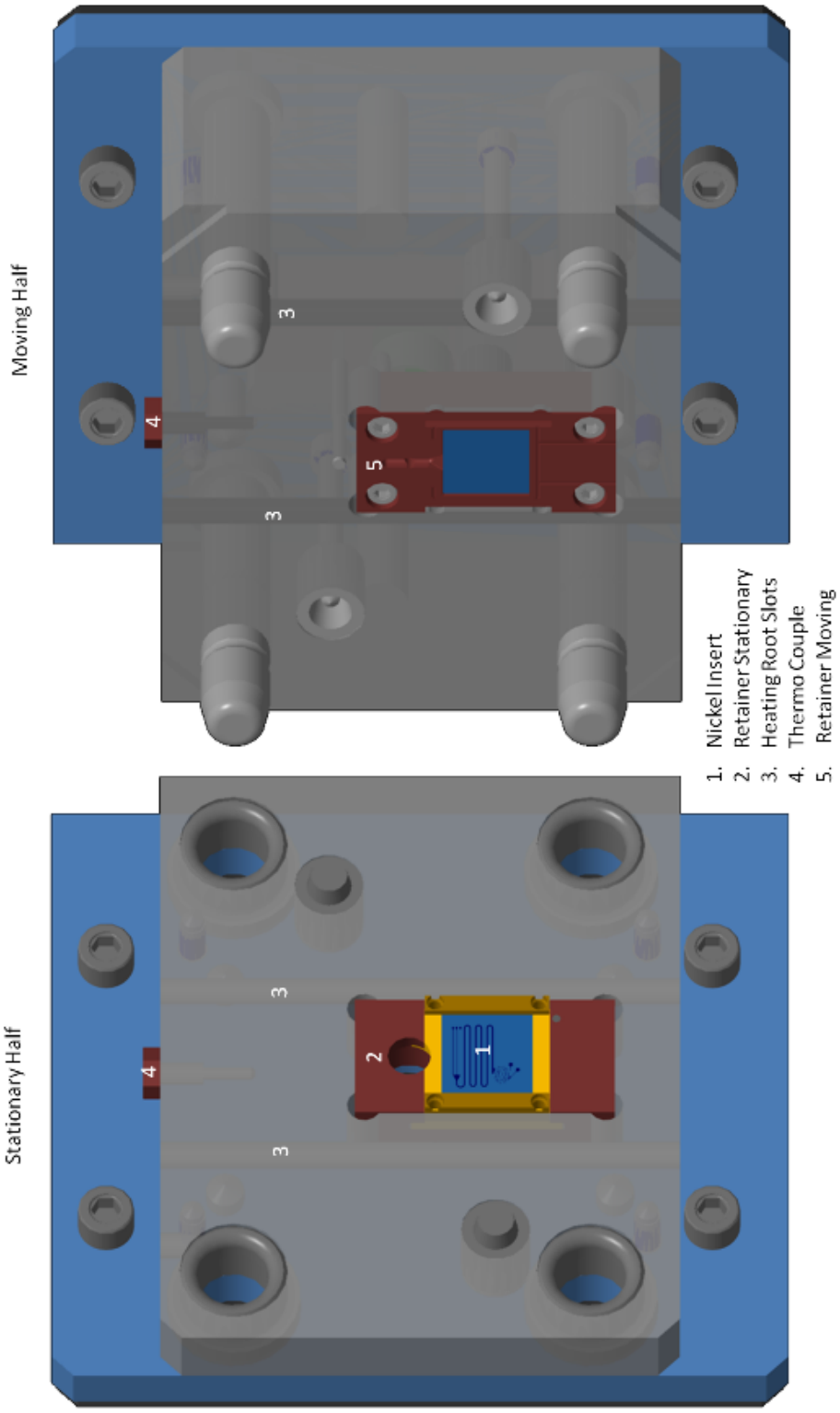

Fig. 5.5 Mold set up

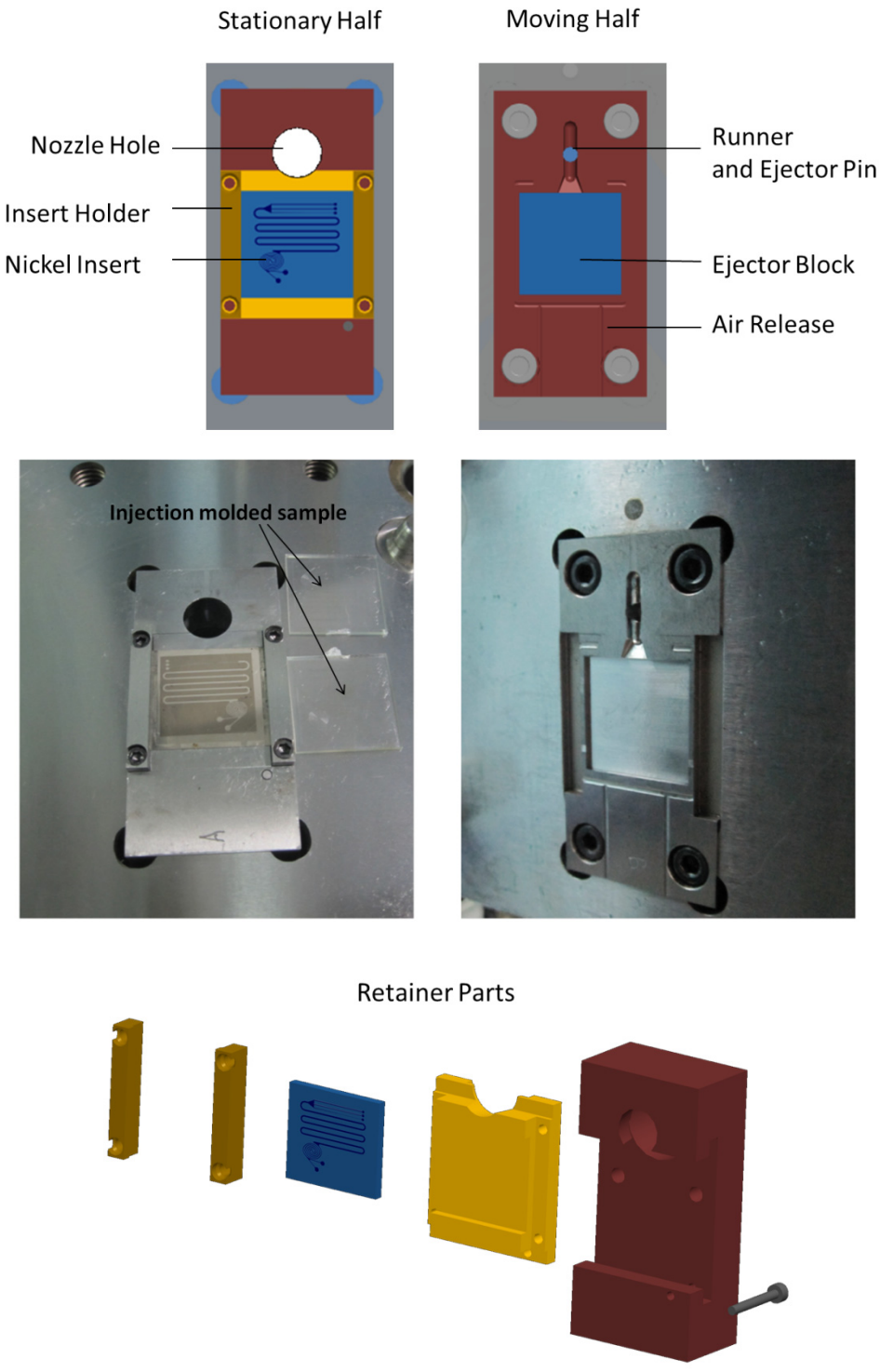

Fig. 5.6 Ni insert retainer showing the clamping mechanism and the different parts

5.2.2 Application of Ni mold fabricated with AR-P 3250 in Injection Molding

The Ni insert was fabricated by PBW and UV exposure combined with electroplating. The design of the structure is shown in Fig. 4.8 which has been discussed in Chapter 4.

As discussed in chapter 4 the pillars were fabricated by PBW while the rest of the chip was fabricated by UV exposure. In my experiment, AR-P 3250 was used to get a thicker resist layer. The experimental details can also be found in Chapter 4. The mold was cut to 21 mm × 23 mm × 2 mm to fit into the injection molding machine.

To replicate the particle separation chip in PC via injection molding, the injection molding circle consists of melt temperature 320 ℃, mold temperature 90 ℃ and injection speed of 140 mm/s. The injection molded sample was measured with profilometer. The measured result is shown in Fig. 5.7. As can be seen from the figure, the height of pillar is almost 10 μm.

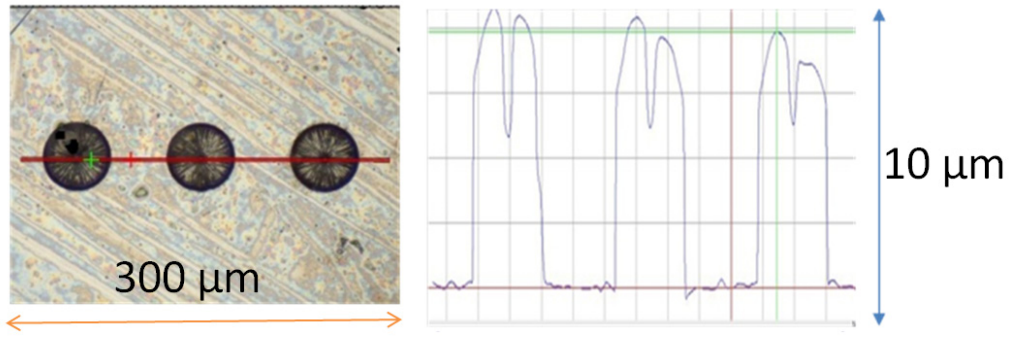

Fig. 5.7 Measured result of injection molded pillars based on profilometer

5.2.3 Application of Ni mold fabricated with ma-N 2410 in Injection Molding

Ni molds fabricated with ma-N2410 were used in the same injection molding machine. Here we used the mold with details down to 500 nm and a depth of 1 μm. Details of the fabrication process have already been introduced in chapter 2 and 3. The Ni mold was also cut to 21×23×2 mm^3 to fit in the injection molding machine. In our experiment, PC and PMMA were tested.

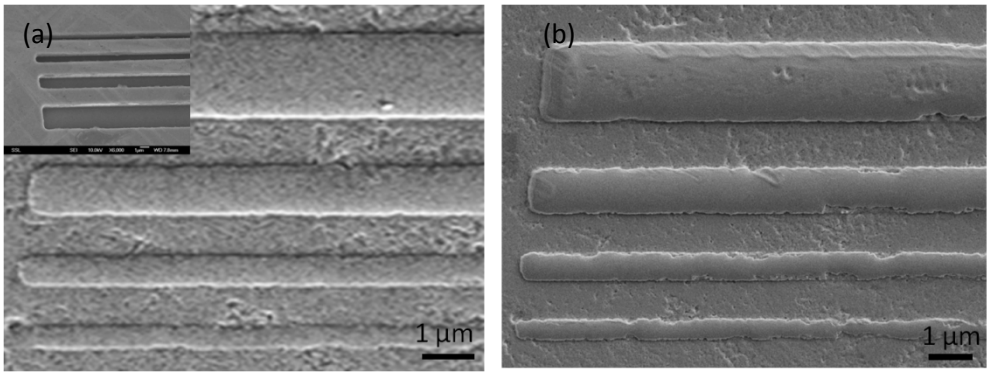

Fig. 5.8 Injection molded structures with PC (a) injection speed: 600 mm/s, mold temp.: 80 ℃; (b) injection speed: 600 mm/s, mold temp.: 100 ℃ (inserted figure is Ni mold).

Fig. 5.8 shows an initial test with a Ni mold using PC. PC was heated to 330 ℃ in the barrel, and injected into the mold cavity to fill the structures. In Fig. 5.8a, the injection speed is 600 mm/s, and the mold temperature is 80 ℃. As can be seen from the figure, the width of the structures was faithfully replicated in PC. However, the height of the structures is only 150 nm measured in SEM. With an injection speed of 700 mm/s, there was no obvious difference compared with the one at 600 mm/s. In addition, 700 mm/s almost reaches the limit of machine (Maximum speed: 750 mm/s). Therefore, we just stick to 600 mm/s. In order to fill the cavity better, the mold temperature was increased to 100 ℃ while keeping the injection speed at 600 mm/s, see Fig. 5.8b. The height of the structures is about 300 nm which is double compared to the previous result. If the temperature of the mold increases, the viscosity of

PC will decrease. This helps PC to fill in the channels in the mold. If the mold temperature is increased further it is expected that the result would improve. However, the limit of the mold temperature of the machine is 100 ℃. As a result, the machine has reached its limit with PC.

The glass transition temperature of PC is 147 ℃. If we use materials with a lower glass transition temperature, better filling of the mold cavity is expected. Therefore we used PMMA since the glass transition temperature of PMMA is only 105 ℃. Injection molding results of PMMA are shown in Fig. 5.9.

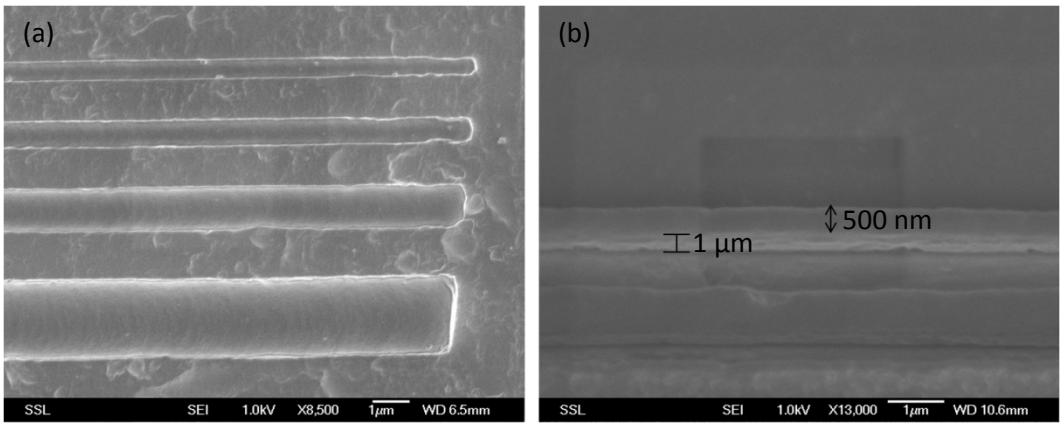

Fig. 5.9 Injection molded structures with PMMA (a) injection speed: 700 mm/s, mold temp.: 90 ℃; (b) injection speed: 700 mm/s, mold temp.: 100 ℃. (tilted by 30^{o})

PMMA heated in the barrel to 260 ℃. With an injection molding speed of 700 mm/s and mold temperature of 90 ℃, the structures can be replicated in PMMA. However the height of the structures is only about 500 nm. When the mold temperature is set at 100 ℃, the injected PMMA can completely fill the grooves in the Ni mold. As can be seen from Fig. 5.9b, the smallest line is 500 nm wide and 1 μm high.

5.2.4 Application of Ni mold fabricated PMMA 950 A11 in injection molding

The Ni mold fabricated with PMMA 950 A11 has been introduced in chapter 3. In this section, I will give the results based on this Ni mold for injection molding. Fig. 5.10 shows a Ni mold with ridges of 300 nm and 1.5 μm wide and a height of 1 μm. The Ni mold was cut to 21 × 23 ×2 mm^3 to fit in the injection molding machine. In addition, PMMA was chosen because of its low glass transition temperature.

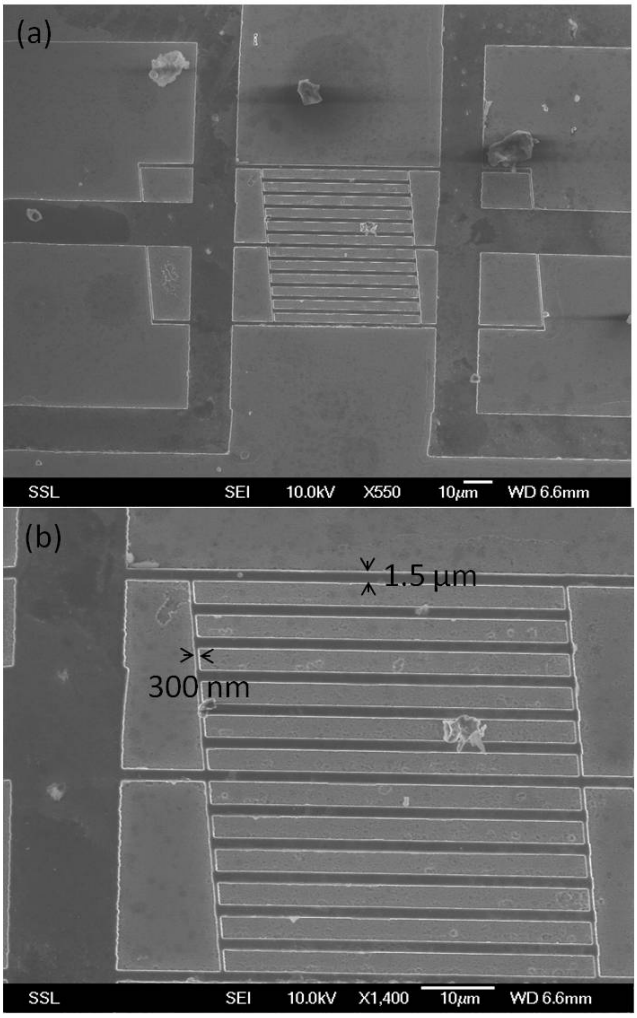

Fig. 5.10 (a) Ni molds fabricated with ridges of 300 nm and 1.5 μm wide (b) a high magnification of the structures in the central part

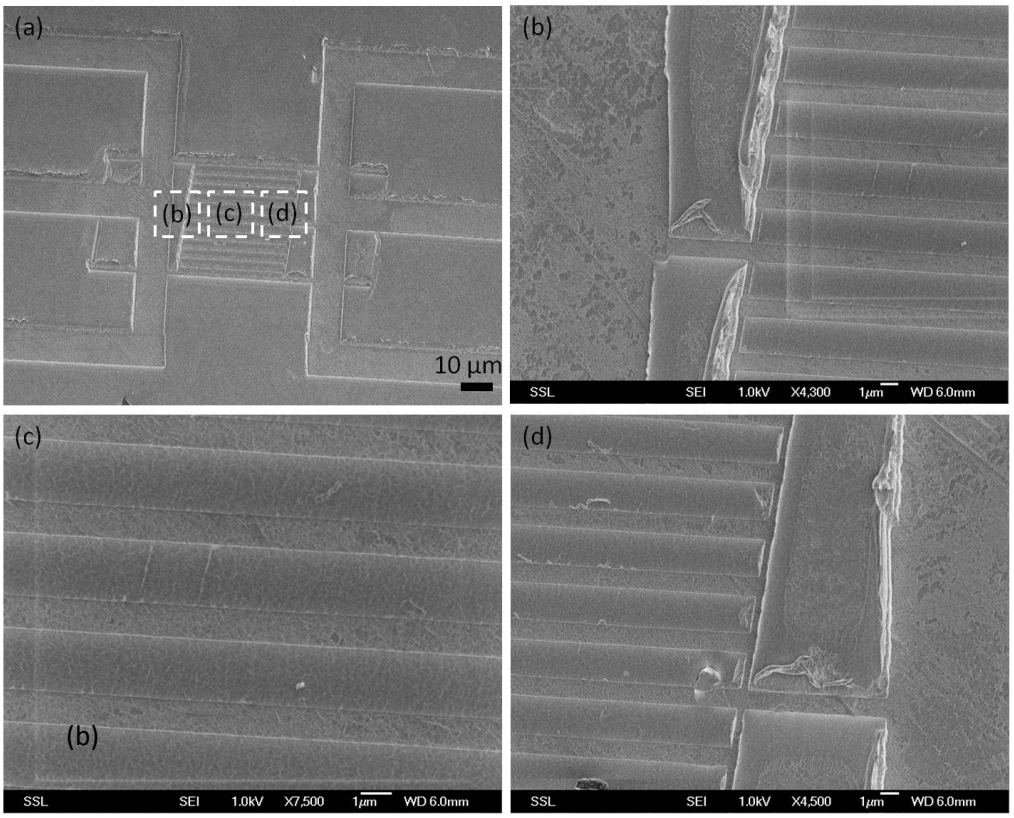

Fig. 5.11 Injection molded PMMA (b) (c) (d) are high magnification figures labeled in fig. (a)

PMMA was heated to 260 ℃, and injected into the mold cavity at a speed of 700mm/s with the mold temperature of 100 ℃. The injection molded PMMA structures are shown in Fig. 5.11.

As can be seen from the figure, the depth of the channel is very small, only 300 nm measured in SEM. However, the parameters we used in the injection molding have reached its limit. Following the general consent that high values of processing parameters have a positive effect on the quality [14, 15]. It can be said that the setup as it is right now cannot achieve complete cavity filling.

5.3 Summary

In this chapter, injection molding machine was first introduced followed by the development in Micro- and nano-fabrication area. Injection molding is an industry technique which has not too much research on micro- and nano-fabrication.

In our project, Ni molds with micro- and nanostructures were used in a Battenfeld Microsystem 50 injection molding machine---. The Ni mold designed for the microfluidic chip was first tested using polycarbonate (PC). PC can almost fully fill the 10 μm deep holes with diameter of 60 μm in Ni mold due to smoothness of the sidewalls. However, the fill is not 100%. Further optimization should be done to address the problem.

The Ni mold featuring 500 nm wide and 1 μm deep grooves were tested in the Battenfeld Microsystem 50 with both PC and PMMA. PC was not a good choice for such small structures since the fluidity is not as good as PMMA. Better results with PMMA were achieved. PMMA can fully fill the 500 nm wide and 1 μm deep groove in the Ni mold. The aspect ratio of the structure is 2 which is impressive in injection molding at these dimensions.

The Ni mold with grooves down to 300 nm was also tested in the Battenfeld Microsystem 50. The 300 nm wide groove can be replicated. However, the height of the structures is much smaller than the structures in the mold. Further optimization should be done to achieve smaller structures with complete groove filling.

References

[1] http://en.wikipedia.org/wiki/Injectionmolding

[2] Todd, Robert H., Allen, Dell K., Alting, Leo, *Manufacturing Processes Reference Guide*, Industrial Press, Inc, 1994

[3] http://www.aclaryn.com/injection.html

[4] Bryce, Douglas M, *Plastic Injection Molding: Manufacturing Process Fundamentals*, SME, 1996

[5] "Injection Molding". custompart.net. CustomPartNet

[6] epsilon industry, http://epsilonindustries.com/resources/plastic-injection-material-selection/

[7] D. Macintyre, S. Thoms, *The fabrication of high resolution features by mould injection*, Microelectronic Engineering, V 41-42, 1998

[8] K. Monkkonen, J. Hietala, P. Paakkonen, E. Paakkonen, T. Kaikuranta, T. Pakkanen, T. Jaaskelainen, *Replication of sub-micron features using amorphous thermoplastics*, Polym. Eng. Sci. 42 1600-1688, 2002

[9] Menges G, Michaeli W, Mohren P, *Special processes – special molds. In: How to make injection molds*, Hanser, Munich, pp 577–587, 2001

[10] Yamagiwa Y, *Micro-injection molding*, J Japan Soc Polym Proc, 15:257–259, 2003

[11] A. Liou, R. Chen, *Injection molding of polymer microand sub-micron structures with high-aspect ratios,* Int. J. Adv. Manuf. Technol., 28 1097–103, 2006

[12] Maria Matschuk, Niels B. Larsen, *Injection molding of high aspect ratio sub-100 nm nanostructures*, J. Micromech. Microeng. 23 025003, 2013

[13] Liu Nan Nan, Shao Peige; Kulkarni, S.R.; Zhao Jianhong; van Kan, J.A. *Nickel Injection Mould Fabrication via Proton Beam Writing and UV Lithography*, Source: Key Engineering Materials, v 447-448, p 188-92, 2010

[14] C. Griffiths and S. Dimov, *The effects of tool surface quality in micro-injection moulding*, Journal of Materials Processing Technology, vol. 189, pp. 418-427, July 2007

[15] B. Sha, S. Dimov, C. Griffiths, *Investigation of micro-injection moulding: Factors affecting the replication quality*, Journal of Materials Processing Technology, v 183, pp. 284-296, 2007

Chapter 6 Conclusion

In this project, I have produced reliable Ni molds via PBW and electroplating. The Ni molds are used for nanoimprinting and injection molding. High quality structures are replicated in plastic using the Ni molds. Combined with thermal bonding, lab-on-chip devices are also fabricated. With PBW, Ni plating and nanoimprinting , it is possible to achieve structures down to 100 nm with aspect ratio of 2 which have great potential in nanofluidics.

In this PhD thesis, we study several new photoresists in PBW consisting of ma-N 2401, ma-N 2410, AR-P 3250 and mixture resist for PBW. The resist structures are transferred to Ni through electroplating. Table 6.1 shows the results on the resist and Ni structures.

Resist	Dose (nC/mm^2)	Energy of proton (MeV)	Resist structures		Ni structures	
			Minimum size (nm)	Aspect ratio	Minimum size (nm)	Aspect ratio
ma-N 2401	40	1	60*	1.67	+	N.A.
ma-N 2410	250	1	250**	2.4	500+	2
AR-P 3250	50	1	330**	10.6	330#	10.6
Mixture (AR-P 3250:AR 300-12=1:3)	50	1	120**	2.3	120#	2.3

* Limited by beam focus

** Limited by resist characteristic

+ Limited by resist removal issues

Resist removal possible in narrow proton dose window.

As can be seen from the table, new negative photoresist ma-N 2401 is capable of fabricating high resolution structures down to 60 nm using 1 MeV protons. However, such small structures cannot be used in Ni mold fabrication. The resist cannot be removed in the Ni. ma-N 2410 can be machined to 250 nm at a height of 600 nm using 1 MeV protons. However, 250 nm wide resist structures cannot be removed after Ni electroplating. Structures as large as 500 nm in 1 μm thick ma-N 2410 can be transferred to Ni. As a result, 500 nm

wide grooves with aspect ratio of 2 can be achieved in Ni mold. AR-P 3250 is an interesting photoresist since it shows positive to UV (360 nm) and negative to PBW. 330 nm wide structures were fabricated in a 3.5 μm thick AR-P 3250 using 1 MeV protons. The structures show very vertical and smooth sidewall. In fact, even smaller structures (200 nm wide in 4 μm thick AR-P 3250) can be fabricated, however, because of the very high aspect ratio, the structures cannot stand on the substrate. Using this photoresist, Ni grooves down to 330 nm wide with depth of 3.5 μm can be fabricated. The resist can be completely removed. AR-P 3250 is a very nice negative photoresist to fabricate Ni molds. The typical thickness of AR-P 3250 is larger than 3 μm. In order to achieve thinner thickness, AR-P 3250 was mixed with AR 300-12. At a ratio of 1:3, a 280 nm thick layer was obtained. The mixture has same property as AR-P 3250. Using 1 MeV protons, structures down to 120 nm can be achieved in this 280 nm thick film. The structures can be well transferred to Ni mold.

The Ni molds were used in nanoimprinting as well as injection molding. Structures down to 120 nm wide and 280 nm high can be well replicated on PMMA plastic sheet in nanoimprinting. A 500 nm structure with aspect ratio of 8 was also replicated in nanoimprinting. Using this technique and PMMA thermal bonding, a full PMMA microfluidic device was easily fabricated in our research. The microfluidic device was tested with injected DI water showing no leak along the path.

However, there was one problem in nanoimprinting. The demolding process was not very easy to control. Sometimes the plastic could be easily peeled off from Ni mold, and sometimes it was very difficult to remove. Demolding is a very important step in nanoimprinting technique and has a major effect on the quality of micro-nanostructures. If the demolding process can be carried out very appropriately, the results of micro-nanostructures would be much better. Further optimization through anti sticking layers should be investigated in this specific process of nanoimprinting.

Using injection molding, 500 nm wide and 1 μm high PMMA lines were fabricated with Ni mold fabricated by resist ma-N 2410. The means PMMA can fully fill the grooves in the Ni mold. This is very remarkable to achieve high aspect ratio structures in sub-μm size. 300 nm wide and 500 nm deep PMMA channels were also realized with another Ni mold fabricated by resist PMMA 950 A11. However, in this Ni mold the depth of the structures is about 1.2 μm. This shows the incomplete filling of the cavity in this Ni mold. Nevertheless, lots of parameters have been tested with the injection molding machine with no obvious improvement. The setup of the machine has reached its limit. Further research on injection molding should be done to replicate plastic structures with Ni molds in some other machine with higher injection pressure and mold temperature. In addition, more materials that can be used in electroplating, nanoimprinting or injection molding can be tried in the future.

In our research, we have shown that we can fabricate a well bonded chip that can be used in microfluidic applications. The processes include PBW; Ni electroplating; nanoimprinting or injection molding. Finally through PMMA to PMMA bonding lab on chip devices can be produced. This will enable researchers to expand applications and create a much cheaper and faster method to fabricate microfluidic devices. Now we are working towards nanofluidic device fabrication. By choosing new proper photoresist for PBW and optimization of the techniques used in this project, sub 100 nm nanofluidic devices can be achieved.

It is also hoped that, in the future, proton beam writing can play a major role as next generation lithography technique and also be expected to make a remarkable contribution to the advancing micro- and nano-fabrication technologies.

Köpenicker Straße 325 • 12555 Berlin – Germany • Tel.: +49 30 65762192 • Fax: +49 30 65762193 • mrt@microresist.com

DIN EN ISO 9001:2000
ZN: 09 100 75084

— Processing guidelines —

Negative Tone Photoresist Series ma-N 2400

Characteristics

ma-N 2400 is a negative tone photoresist series designed for the use in micro- and nanoelectronics. The resists are available in a variety of viscosities.
- electron-beam and DUV-sensitive
- well suitable as an etch mask exhibiting high dry and wet etch resistance
- good thermal stability of the resist patterns
- high resolution capability
- aqueous alkaline development

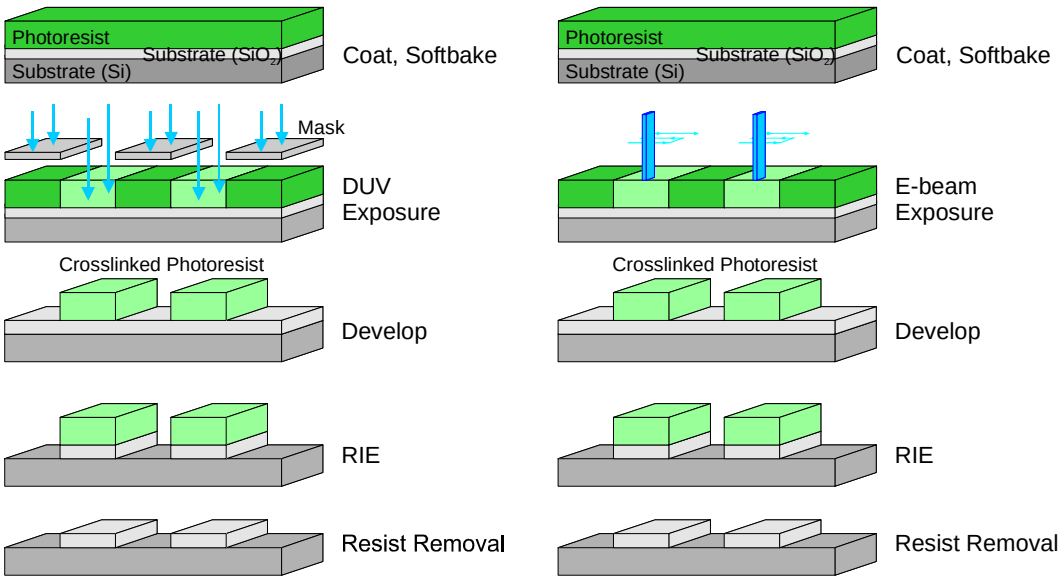

Process flow for DUV and reactive ion etching (RIE)

Process flow for e-beam and RIE

Physical properties of the resist solution

Resist		**ma-N 2401**	**ma-N 2403**	**ma-N 2405**	**ma-N 2410**
Film Thickness[1]	[µm]	0.1± 0.02	0.3 ± 0.02	0.5 ± 0.05	1.0 ± 0.1
Dynamic Viscosity[2]	[mPa s]	1.4 ± 0.3	2.2 ± 0.3	3.2 ± 0.5	7.2 ± 0.5
Density	[g cm^3]	0.986 ± 0.002	1.008 ± 0.002	1.020 ± 0.003	1.043 ± 0.003

[1] Spin coated at 3000 rpm for 30 s
[2] 25°C, 1000 s^{-1}

Processing

Best patterning results are obtained at temperatures of 20 – 25 °C and a relative humidity of 40 – 46 %. The guidelines relate to standard processing of resist films spin coated on silicon or silicon dioxide. The specific process parameters to be applied depend on substrate, application and equipment.

Processing conditions

Resist		ma-N 2401	ma-N 2403	ma-N 2405	ma-N 2410
Film thickness	[µm]	0.1	0.3	0.5	1.0
Substrate preparation		Oven: 200 °C, 30 min			
Spin coating	[rpm] [s]	3000 30			
Prebake					
Hotplate	[°C] [s]	90 60	90 60	90 90	90 150
Exposure dose					
e-beam					
20 keV [1]	[µC cm^{-2}]	120 - 200 (D_0 = 80)[3]	170 – 235 (D_0 = 80)[3]	170 – 250 (D_0 = 80)[3]	(D_0 = 80)[3]
50 keV [1]	[µC cm^{-2}]	120 – 260	120 – 300	150 – 350	
DeepUV [2]	[mJ cm^{-2}]	210 ± 20	260 ± 20	330 ± 30	420 ± 50
Development [3] **ma-D 525**	[s]	10 ± 3	30 ± 5	60 ± 10	130 ± 10
ma-D 331	[s]	10 ± 3			
ma-D 332	[s]	5 ± 3	10 ± 3	15 ± 5	35 ± 10

[1] exposure dose depends on the pattern size/ resolution - [2] broadband exposure, intensity measured at λ=260 nm
[3] D_0= clearing dose, [4] immersion development

Substrate preparation:

The substrates have to be free of impurities and moisture. They should be baked at 200 °C and cooled to room temperature immediately before coating. Alternatively, oxygen or ozone plasma cleaning is recommended.

Coating:

Uniform coatings are obtained by spin coating of ma-N 2400 solutions in the thickness range indicated in the spin curves. Please select the appropriate resist type and spin speed required for the desired film thickness and application. The information refers to an open spin-coating system. The film thickness is measured after the prebake process. It is recommended to use a filter when applying the resist to the wafer for spin-coating.

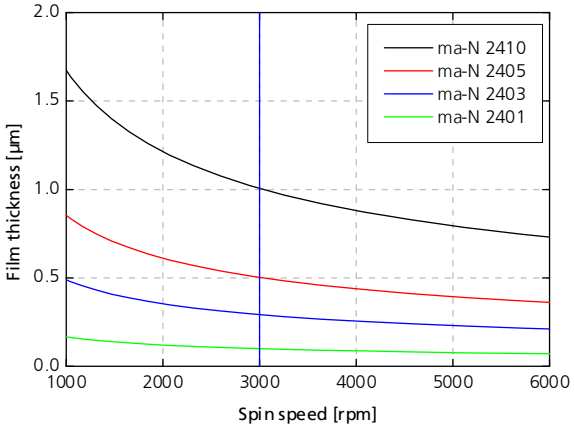

Fig. 1: Spin curves of ma-N 2400 series, 30 s spin time

The refractive index of the resist film depending on the wavelength and the Cauchy equation are given in Fig. 2. This information is needed for ellipsometric or other optical thickness measurement.

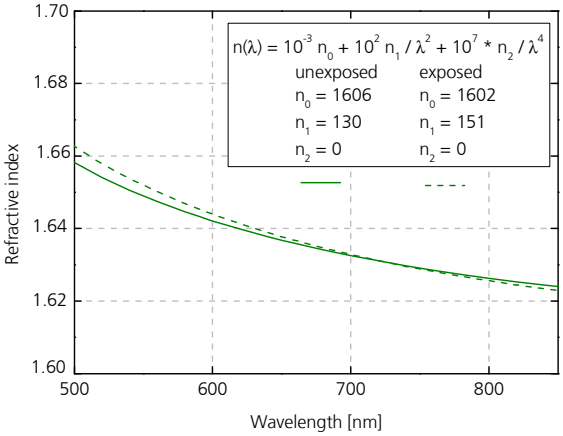

Fig. 2: Refractive index vs. wavelength, Cauchy coefficients of unexposed and exposed ma-N 2400

Prebake:

Resist films are baked on a hotplate at 90 °C. If required, the etch resistance and thermal stability of the resist can be increased by applying a higher prebake temperature (max. 110 °C) or a longer prebake time. The developing time will increase in this case.

Exposure:

The resists are effective for e-beam exposure and Deep UV-exposure.

Resolution and aspect ratio for different types of exposure

	e-beam exposure	Deep UV exposure
Aspect ratio	6	2
Resolution	50 nm	200 nm

E-beam exposure

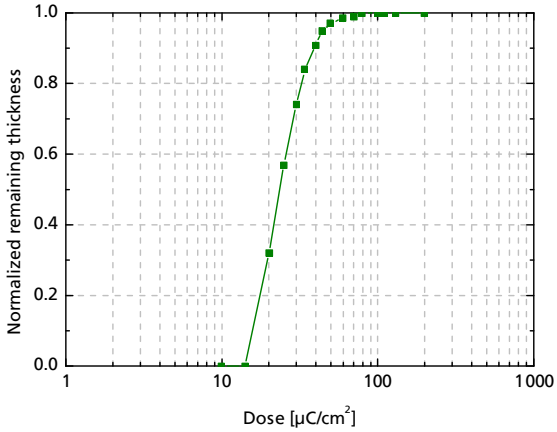

Fig. 3: Sensitivity curve at 20 keV electron energy

With higher electron energies the exposure dose shifts to higher doses. For a specific film thickness the generation of smaller features requires higher exposure doses (~1,5 x D_0) than larger features.

Deep UV exposure

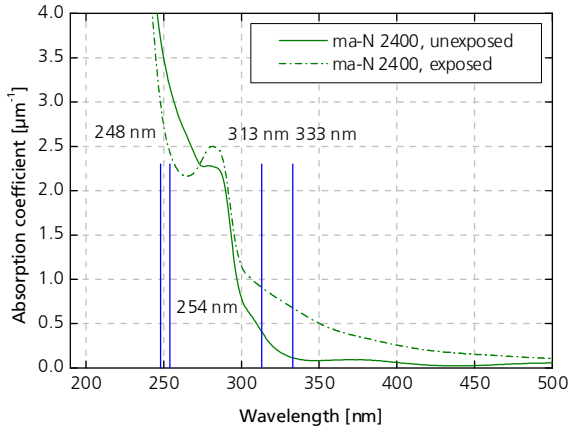

Fig. 4: UV/vis absorption of unexposed and exposed ma-N 2400

Develop:

Ready-to-use developers **ma-D 525** (metal ion free) and **ma-D 332** are recommended. The temperature of the developer should be 20 – 25 °C. The developed resist films are thoroughly rinsed with deionized water for about 5 – 10 min and then dried.

Hardbake (optional):

If required, the etch resistance and the thermal stability of the resist can be further increased. Hardbaking of the developed resist patterns is suggested in an oven at 100 °C for approximately 5 – 15 min.

Removal:

Ready-to-use removers **mr-Rem 660** (solvent based) and **ma-R 404/S** (strongly alkaline) are recommended. Acetone, N-methylpyrrolidone (NMP) or oxygen plasma is also suitable for the residue free removal of the resist.

Storage

Storage at temperatures of 18 – 25 °C is recommended. Do not store ma-N 2400 resists in a refrigerator. Keep the bottle closed when not in use. Under these conditions a shelf life of 6 month from the date of manufacture is ensured.

Disposal

Unexposed resist: dispose of as halogen free solvent
Exposed resist: dispose of as resist/ old resist

Environmental and health protection

ma-N 2400 resist series contains "safe solvents". Ensure that there is adequate ventilation while processing the resists. Avoid contact of the resists with skin and eyes and breathing solvent vapours. Wear suitable protective clothing, safety goggles and gloves.

Equipment

ma-N 2400 resists are compatible with most commercially available photoresist processing equipment. The data given in these guidelines were obtained using:
- Convac spin coater or Suss RC 5 spin coater without cover
- contact hotplate/ convection oven
- ZBA 23H and LION LV1 with 20 keV, Leica EBPG 5000plus with 20 and 50 keV
- High pressure mercury lamp without UV filter
- immersion development

Patterning examples (by courtesy of IPHT/ Jena and HHI/ Berlin)

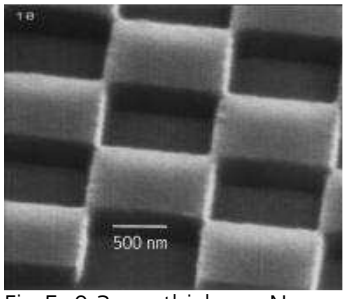

Fig.5: 0.3 µm thick ma-N 2400 chess pattern, e-beam exposed

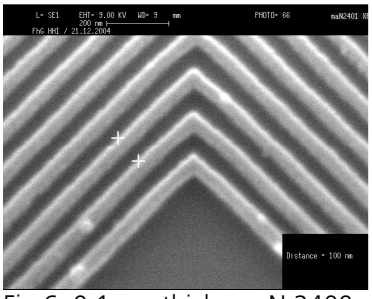

Fig.6: 0.1 µm thick ma-N 2400 pattern, 50 nm lines/ spaces, e-beam exposed

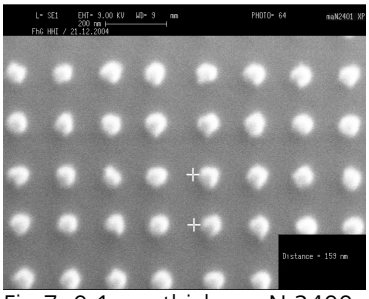

Fig.7: 0.1 µm thick ma-N 2400, 80 nm dots, e-beam exposed

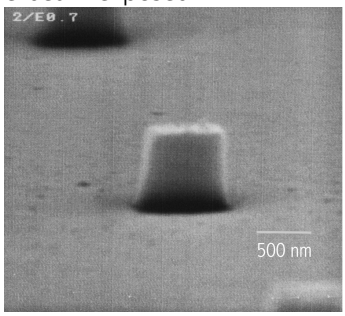

Fig.8a: 0.75 µm thick ma-N 2400, e-beam exposed, 0.8 µm wide dots

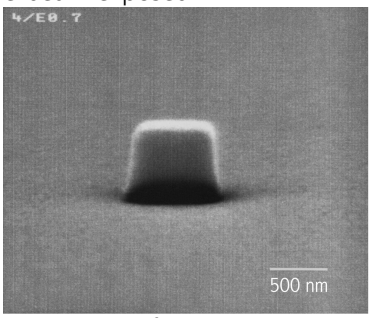

Fig.8b: Dot after a reactive ion etching with CF_4 (power: 60 W)

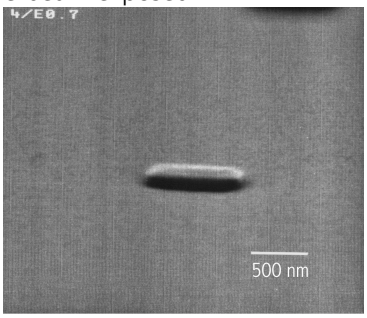

Fig.8c: 0.8 µm wide niobium dot after resist remove

Photoresist serie for thick resist films
AR-P 3200

1. General description

The Photoresists of the series AR-P 3200 are positive liquid resists with high viscosity for high film thicknesses. These resists are well suitable for galvanic process, microsystemtechnics and covering edges of topographies on complicated wafer surfaces (good levelling). It is possible to generate resist pattern with a vertical profile. The resolution of the thick resist layers is very high. The profile of lines shows very steep edges so that a high degree of pattern resolution is given in these films.

Resists **AR-P 3210** a**nd AR-P 3250** are particularly well suited for film thickness values of 40 µm and 20 µm, respectively. Using these resists, vertical profiles with high edge steepness can be generated, allowing a very good structural resolution.

Resist **AR-P 3220** is more sensitive, has a higher transparency in the entire UV range and is this thus especially suitable for thicker films of up to 100 µm by multiple coating. It is possible to exposure and develops a 100-µm-layer in one step. By use of "Closed Chuck-Systems" (gyrset) higher resist thickness can be generated.

The resists contain a combination of novolac resin with diazonaphthoquinone, dissolved in a mixture of solvents main component safer solvent propylene glycol methyl ether acetate.

2. Parameters

Properties / Resist	**AR-P**	**3210**	**3220**	**3250**
Solids content	%	47	47	39
Viscosity (25 °C)	mPa·s	1990	1820	250
Film thickness at 4000 rpm Semitec CPS 20, uncovered chuck, 2" Si-wafer	**µm**	**10**	**10**	**5,0**
Film thickness at 6000 - 2000 rpm Film thickness at 1000 - 250 rpm	µm	8 – 15 20 – 40	8 – 15 20 – 40	4 – 8 10 – 20
Flash point	°C	42		
Filtration	µm	0.8		
Storage at temperatures	°C	10 - 18		
Guarantee from date of sale	months	6		

3. Process chemicals

Developer	AR	300-26
Thinner	AR	300-12
Remover	AR	300-70

4. Processing of AR-P 3200

Before handled the resist has to be adapted to the temperature of the working area (recommended is a range of 20 – 25 °C at a relative humidity from 30 to 50%). The unexposed resist should be handled under yellow safe light.

Equal quantities of resist (e.g. 10 g for 4inch wafers) ensure equal film thickness. Usual coat and bake procedure of standard resist (AR-P 3500) is needed for layers < 10µm. Thicker layers (10-40 µm) should be spin coated for 60-120 seconds. Layers > 40µm should be coated in two steps. Low starting spin speed (30 s) should be followed by a main spin speed of 250-500 rpm, for at least 2-5 minutes. Marginal beads are reduced by a final spin rotation at 800 rpm for 5 seconds.

10-40 µm layers should be prebaked on hot plate (95 - 100 °C, 8-15 min) or in convection oven (85 - 90 °C, 30-60 min). For higher thickness (> 40 µm) a two step bake is recommended:

1.) 70 °C for 30 min in convection oven or 5 minutes using a hot plate.

2.) 85 - 90 °C for 60-90 min in convection oven or 95 - 100 °C for 15-30 min on hot plate. A longer bake reduces the sensitivity as well as the possibility of undercut patterns.

These resists are suitable for application in the wavelength range of 308 - 450 nm.

Instructions for Development

Developer suitable for Photoresists	**AR 300-26** immersion-, puddle- and spray-development, 21-23 °C	**AR 300-35** immersion- and puddle-development, 21-23 °C
AR-P 3210	**1 : 3** (2 … 10 min)	**undiluted to 10 µm** (2 … 10 min)
AR-P 3220	**2 : 1** (2 … 5 min)	**-**
AR-P 3250	**2 : 1** bis **3 : 2** (1 ... 3 min)	**-**

These concentrations of developer are recommended values. The exact concentration of developer should be adjusted to the special parameters (film thickness, time of development, bake). See also ☞ information about developers. ☞ Dilution of developer leads to an increase of contrast by decreasing the speed.

Developed images have to be rinsed in deionized water immediately after developing process.

A post development bake at about 110 °C improves adhesion and resistance of the structure which leads to good etching stability.

5. Cleaning and Removal

Substrates and equipments can be cleaned with the **Thinner AR 300-12** or the **Remover AR 600-70**.

Hard-baked layers can be stripped with the **Remover AR 300-70 or 300-72.** Very hard-baked layers (plasma processing or UV-stabilization) need a treatment with oxidizing acids.

6. Waste Water Disposal

Up to 90% of the organic material of used developer and aqueous alkaline remover can be separated by precipitation through pH-adjustment in a range of 9-10. Filtered solutions have to be adjusted to 6.5–8.0 for final waste disposal. Liquid or solid wastes have to be disposed at proper deposit places or by controlled combustion in officially authorized plants.

7. Safety References

Resists and thinner contain organic solvents. Adequate ventilation in the working area is demanded. Avoid direct contact with products and their vapours.

Wear safety goggles and rubber gloves!

Please ask for safety data sheets!